Adaptive Optics
for Phase and Polarization Control

Yuanyuan Dai

Pembroke College
University of Oxford



A thesis submitted for the degree of
Doctor of Philosophy

Trinity Term 2019

To the most beautiful Mom in the world, Ying Li

and the coolest Dad ever, Yanwu Dai

Acknowledgements

I would like to firstly express my heartfelt thanks to my supervisor Professor Martin J. Booth. He has a wide knowledge of the state-of-the-art on adaptive optics and gives me huge help on my research. His assistance provides me more opportunities to the academic and resources to all the collaborators. Thanks for all his kind support in the lab.

Thanks Jacopo Antonello, Chao He and Jingyu Wang. Their advice from the software to hardware allows me to complete this research smoothly. This research is completed based on their professional guidance.

I also would like to thank the other members in Dynamic Optics group; their help throughout this work is very important.

Lastly, I want to delivery my appreciation to my beloved parents for their unconditional love. They motivate me and give me big financial support throughout all the stages of my study from primary to PhD. I am so grateful to have them besides me and for providing me a haven from the storms of life.

This work is mainly funded by European Research Council (ERC) under the Horizon 2020 research and innovation program (AdOMiS, grant agreement No. 695140) and China Scholarship Council.

Abstract

Adaptive optics (AO) is a powerful tool for microscopy. It helps to improve the image quality and resolution by correcting the aberrations that arise in the optical system or through external disturbance. Most AO technologies concern phase distortion, which is the main issue in the mainstream microscopies.

However, the correction is limited by the capabilities of the adaptive optical devices, e.g. in correction range and correction accuracy. Apart from that, phase distortion is not the only aberration that can affect microscopes. Polarization error is also a major concern for some polarization-sensitive microscopes such as Stimulated Emission Depletion Microscopy (STED) and Structured Illumination Microscopy (SIM).

Therefore, in this thesis, I firstly investigated the capabilities and limitations of a phase correction device, a deformable mirror (DM), specifically its correction range and accuracy based on Zernike mode aberrations. Then an adaptive polarization control (APC) system was developed through both hardware and software aspects. The APC consists of polarization state generator (PSG) and polarization state analyzer (PSA). The two modules were investigated separately first and then integrated together.

The system functionality was then demonstrated using different kinds of samples. Results show that this system is able to correct the external birefringence disturbance dynamically and the measurements could be tailored to the ability of prior knowledge about on the samples. This system could be combined with conventional phase AO methods to provide further improvements in system correction in applications ranging from quantum optics to microscopy imaging.

Table of Contents

Chapter 1 Introduction 1

1.1 Background and motivation 1

1.2 Objective 3

1.3 Organization of this thesis 3

Chapter 2 Background 7

2.1 Optical wavefront 7

2.1.1 Optical field 8

2.1.2 Wavefront 9

2.1.3 Optical aberration 10

2.2 Polarized light 13

2.2.1 Light propagation in crystal 15

2.2.2 Polarizing components 17

2.2.3 Jones calculus 19

2.2.4 Stokes parameters and Müller matrices 22

2.2.5 Poincaré Sphere 26

2.3 Adaptive optics 28

2.3.1 Adaptive optics systems 28

2.3.2 Correction device: deformable mirror and spatial light modulator 29

2.4 Summary 31

Chapter 3 Deformable Mirror Characterization 32

3.1 Introduction 32

3.1.1 Introduction to interferometry and analysis 32

3.1.2 Basic principle of interferometer 33

3.1.3 Image analysis and phase extraction 34

3.2 Aim and experiment set-up 37

3.3 Results and analysis 39

3.3.1 System introduction 39

3.3.2 Data Record and Analysis 40

3.4 Error analysis 46

3.4.1 Small amplitude and step size 47

3.4.2 Large amplitude and step size 59

3.5 Summary 61

Chapter 4 Calibration of SLM for Phase and Retardance Modulation 63

4.1 Combining phase and retardance calibration 65

4.2 Methodology 67
4.2.1 Phase calibration 67
4.2.2 Retardance calibration 73
4.3 Results and data processing 74
4.3.1 Phase calibration results with *x* polarized incident light 74
4.3.2 Phase calibration results with *y* polarized incident light 78
4.3.3 Retardance calibration 80
4.4 Effects of the reflections from front surface of the SLM 81
4.5 Summary 83

Chapter 5 Polarization State Generation and Imaging Polarimeter 85
5.1 Polarization state generator 87
5.1.1 Methodology 87
5.1.2 Experimental set-up 89
5.1.3 Calibration and alignment 92
5.2 Imaging polarimeter 100
5.2.1 The modified Sagnac interferometer 100
5.2.2 Stokes polarimeter 107
5.3 Comparison and conclusion 109

Chapter 6 Adaptive Polarization Control 112
6.1 Methodology 113
6.2 Experiment set-up 115
6.3 Results and Discussion 116
6.3.1 Vortex half wave retarder 117
6.3.2 Stressed plastic plate 121
6.3.3 Liquid crystal device 123
6.3.4 Mouse brain tissue 125
6.4 Summary 127

Chapter 7 Conclusion and Outlook 129
7.1 Conclusion 129
7.2 Outlook 130

Appendix: Conversion between Stokes parameters and Jones vectors 134

Publications during DPhil study 136

References 137

List of Figures

Figure 2. 1: Schematics of Young's double slit interference experiments [18]. 8
Figure 2. 2: A single positive lens transfers a plane wave to a converging spherical wave. 10
Figure 2. 3 Noll's index for Zernike polynomials [35]. 12
Figure 2. 4: Light propagation schematic showing the electric (E) and magnetic (B) fields. 13
Figure 2. 5: Different polarization states with different δ, $\delta = \delta x - \delta y$ 15
Figure 2. 6: Light transmitted through to a polarizer becomes linearly polarized. 15
Figure 2. 7: Comparison of the RI ellipsoids of different materials. Isotropic: $nx = ny = nz = no$; uniaxial positive: $no < ne$; uniaxial negative: $no > ne$; biaxial: nx, ny, and nz are all different. 17
Figure 2. 8: Polarization ellipse. 24
Figure 2. 9: Polarized point P in the subspace of S_1 S_2 S_3 represents its polarization state. 25
Figure 2. 10: Polarized light represented by the Poincaré sphere: S_0 = 1, S_1 = $\cos 2\chi \cos 2\psi$, S_2 = $\cos 2\chi \sin 2\psi$, S_3 = $\sin 2\chi$. 27
Figure 2. 11: General schematic of an adaptive optics system. 29

Figure 3. 1: Schematic of (a) Twyman-Green interferometer (b) Sagnac interferometer 33
Figure 3. 2: (a) Components separated in the frequency domain (b) Select the first order frequency and shift it to the center, which is equivalent to demodulation. 36
Figure 3. 3: (a) Experimental interferometer schematic (b) Real set-up. 37
Figure 3. 4: (a) Each mirror segment was controlled by three actuators. (b) The whole mirror segments arrangement (hexagon). 38
Figure 3. 5: Measured mirror shape for open-loop positioning of the Iris DM after applying different Zernike modes [62]. 39
Figure 3. 6: Flow chart of the measurement process. 40
Figure 3. 7: (a) Initial interferogram with the applied mask (b) Zoomed in fringes. 41
Figure 3. 8: Effective analysis area and interferogram after applying the aperture mask. 42
Figure 3. 9: Fourier transform and mask of initial interferogram, three bright dots represent three frequency orders existing in the fringes. 43
Figure 3. 10: Analysis process from fringes to phase. Interferogram (f), Fourier transform (F = F[f]), apply uniform mask (M), mask multiplication (F*M), shift to origin (shifted), phase (ϕ) 43
Figure 3. 11: (a) Wrapped phase of the interferogram with tilt and (b) Calculated unwrapped phase 44

Figure 3. 12: PTT value of initial interferogram. Blue line: estimated amplitude from the interferogram; red line: set amplitude sent to the DM.....45
Figure 3. 13: (a) Comparison of the amplitude of different Zernike modes of set and estimated when the DM is set to 0.5 μm *rms* tilt (b) Calculated unwrapped phase. 45
Figure 3. 14: Comparison of the measured amplitude and set amplitude for 2−21 Zernike mode (Noll's index) and corresponding errors, which are calculated as the sum of *rms* amplitude of other Zernike modes and difference between the set amplitude and measured amplitude. 49
Figure 3. 15: Unwrapped phase and comparison of estimated and set Zernike coefficient (a) Mode 5 phase (b) Mode 5 coefficient comparison (c) Mode 6 phase (d) Mode 6 coefficient comparison (e) Mode 9 phase (d) Mode 9 coefficient comparison (g) Mode 10 phase (h) Mode 10 coefficient comparison. 51
Figure 3. 16: Simulation (a) Ideal phase profile for mode 20 (b) measured unwrapped phase and coefficient comparison of mode 20 with an amplitude of 0.5 (c) Ideal phase graph for mode 21 (d) measured unwrapped phase and coefficient comparison of mode 20 with an amplitude of 0.5.....52
Figure 3. 17: Measured phase profile of mode 7 and 8 with different amplitudes. 53
Figure 3. 18: (a) Mode 7 phase profile with an amplitude of 0.5 with smaller mask (b) Mode 7 phase profile with an amplitude of 0.4 with smaller mask (c) Mode 7 phase profile with an amplitude of 0.5 with normal mask (d) Mode 7 phase profile with an amplitude of 0.4 with the normal mask. 54
Figure 3. 19: Maximal ideal phase graph of (a) Mode 16 (b) Mode 17.....54
Figure 3. 20: (a) Cross-section phase analysis (b) Measured phase of mode 17 with an amplitude of 0.4 with normal mask (c) Measured phase of mode 17 with an amplitude of 0.4 with smaller mask (c) Ideal phase; the *x* axis is the pixel number along the diagonal and *y* axis is the relative amplitude. 55
Figure 3. 21: Comparison between the set (red line) and measured (blue line) Zernike coefficients for different modes and amplitudes (a) Mode 11 at amplitude of 0.5 (b) Mode 19 with amplitude of 0.5 (c) Mode 19 with amplitude of 0.4.....57
Figure 3. 22: Average error sum ε from amplitude of -0.5 to 0.5 at different modes. 59
Figure 3. 23: The measured amplitude for Zernike modes 2–15 (Noll's index) and corresponding errors, with amplitude from -2 to 2 and step size of 1. 60

Figure 4. 1: (a) Schematic of the SLM calibration: Twyman−Green interferometer. The analyzer was inserted when doing the retardance calibration. HWP: half wave plate. BS: 50:50 beam splitter; SLM: spatial light modulator. (b) Interferogram obtained when the SLM was replaced with a flat mirror. 68

Figure 4. 2: Blue circles: mean value of the phase measured with the interferometer when the SLM was replaced with a flat mirror; Red crosses: remaining phase after removing ε_i. After removing ε_i the phase becomes stationary as expected for a flat mirror. 69

Figure 4. 3: Schematic of the measurement process. The sets of reference (R) and normal (N) measurements were interleaved in time as shown to subsequently apply interpolation and detrending. 71

Figure 4. 4: Decomposition of the phase in the terms outlined in Eq. (11). (a) Γ'_i varying as a function of PGV at the center point of the SLM; (b) ε_i varying with the measurement i (c) calculated Φ_i varying as a function of PGV. For the SLM calibration, the values Φ_i shown in (c) are of interest. 71

Figure 4. 5: Flow chart of the data processing and analysis method. 72

Figure 4. 6: Phase extraction results from the SLM center point (a) Γ_i (b) Γ'_i after removal of the piston offset $2k_i\pi$ introduced by the phase unwrapping algorithm. 75

Figure 4. 7: Comparison of phase varying as PGV before and after Step 2 and 3. Red circle: Γ'_i in Eq. (4.11); yellow cross: Φ_i in Eq. (4.11); blue line: Φ_S, 3rd order polynomial fit in Eq. (4.12). 76

Figure 4. 8: (a) The phase map at PGV = 0, SLM was divided into 30×40 sub-regions for phase response analysis. (b) Φ_S variation along the SLM x direction at y = 15, PGV = 0; the x axis represents the x coordinate of the SLM sub-region (c) Φ_S variation with PGV at region (3,15). (d) Φ_S variation with PGV at center region. 77

Figure 4. 9: Results after Step 4: subtraction of the phase at PGV = 0 for visualizing the polynomial coefficient differences at SLM different regions (a) The relative phase map, $\Phi_S - d$, at PGV = 155 (b) $\Phi_S - d$ variation along y direction at x = 20, PGV = 155; the y axis represents the y coordinates of the SLM sub-region (c) $\Phi_S - d$ variation along x direction, at y = 20, PGV = 155 (d) $\Phi_S - d$ variation as PGV at the center region. 78

Figure 4. 10: Calibration for y polarized incident light. (a) Phase varying as a function of PGV before and after removing phase disturbance ε. Blue circle: before step 2: removing the phase disturbance; Red Cross: after step 2: removing the disturbance. (b) Phase variation along x direction at y = 15, PGV = 0. 79

Figure 4. 11: Retardance calibration: intensity profile recorded by the camera with 45° linearly polarized input light and viewed after the analyzer at (a) PGV = 3 (b) PGV = 56 (c) PGV = 187. 80

Figure 4. 12: Retardance calibration. (a) Red Dot: intensity change with PGV at region (19,18) recorded by camera. Blue Line: Fit obtained. (b) Retardance variation with PGV at (19,18) according to fitting result. (c) Red Dot: intensity change with PGV at region (4,17). Blue Line: fit obtained. (d) Retardance variation with PGV at (4,17). 81

Figure 5. 1: The principle of adaptive polarization control is similar to phase control principle. The polarization state generator (PSG) serves as the correction device while the polarimeter serves as the wavefront sensor in AO. 86
Figure 5. 2: A linear retarder effect on the polarization state on the Poincaré sphere. The input state is at point A. It rotates across the axis that has an angle of 2θ to S_1 axis, and change the retardance of δ. 88
Figure 5. 3: (a) The first pass on the SLM is equivalent to rotate the polarization state from the input 45° linear polarization to any point on the green circle. The second pass on the SLM is equivalent to rotate the polarization state from the ending point on the first pass around S_2 axis (orange). (b) When the input polarization state is not 45° linearly polarized, the sphere surface to the right of the orange circle is not accessible. 88
Figure 5. 4: Schematics of the dual pass SLM polarization modulation scheme. The SLM was divided into two windows to realize dual-pass modulation. 90
Figure 5. 5: Polarization state after each component with the SLM retardance set to 0. 91
Figure 5. 6: Schematic of the PSG alignment set up 93
Figure 5. 7: Generated pattern with retardance labelled on different parts (left image); and its image recorded by camera after applying the pattern on the SLM through a linear polarizer with transmission axis aligned with white arrows at vertical (middle image) and horizontal (right image) 94
Figure 5. 8: Simulation of the Stokes parameters when the retardance of the first pass is fixed at an arbitrary value of $\delta 1 = 7\pi 24$ rad (this angle is chosen since the deviation is obvious to see) and the second pass of the retardance is changed from 0-2π. The blue line is the Stokes parameter when $\theta = \pi 100$ rad and the red line is ideal case: when θ = 0 rad. 97
Figure 5. 9: Simulation of the Stokes parameters when the retardance of the second pass is fixed at an arbitrary value of $\delta 2 = 11\pi 8$ rad and the second pass of the retardance, δ_1, is changed from 0−2π. Blue line is the Stokes parameter when $\theta = \pi 100$ rad and the red line is ideal case: when θ = 0 rad. 97
Figure 5. 10: Simulation of the Stokes parameters after removing the QWP, fixing the retardance of the first pass of $\delta 1 = 7\pi 24$ rad, and changing the second pass of the retardance, δ_2, from 0−2π. The blue line is the Stokes parameter when $\theta = \pi 100$ rad and the red line is ideal case: when θ = 0 rad. 98
Figure 5. 11: Stokes parameters measurement of the center region of the output light when the first pass PGV was fixed at 100 and the second pass PGV was varied from 0−255. 99
Figure 5. 12: Stokes parameters measurement of the center region of the output light when the second pass PGV was fixed at 140 and the first pass PGV was varied from 0−255. 99

Figure 5. 13: Stokes parameters measurement of the center region of the output light when the second pass PGV was fixed at 100 and the first pass PGV was varied from 0−255. 100
Figure 5. 14: Schematics of the interferometer imaging polarimeter. 101
Figure 5. 15: Example fringe image from the modified Sagnac interferometer. 101
Figure 5. 16: Data recording process and notation. 103
Figure 5. 17: (a) Simulated model image (b) calculated amplitude (c) calculated phase. Note that the phase values in the low amplitude regions have arbitrary values..... 104
Figure 5. 18: Basic configuration of a Stokes polarimeter..... 108
Figure 5. 19: Intensity image recorded by camera at different QWP fast axis orientation. (a) 15.1° (b) 51.7° (c) 128.3° (d) 164.9° 109
Figure 5. 20: Stokes parameters calculated (a) S_1 (b) S_2 (c) S_3, theoretical Stokes parameters of 45° polarized light is $[S_1, S_2, S_3]^T = [0, 1, 0]^T$ 109
Figure 5. 21: (a) Interferogram recorded if the beam is nearly -45° polarized. The low intensity decreases the accuracy to calculate the polarization state. (b) Two beams after the PBS was hard to be superposed perfectly. 110

Figure 6. 1: Principle of the APC system operation. Blue solid line: beam propagation direction; grey dashed line: calculation path. 114
Figure 6. 2: Schematic of the experimental setup of the APC system. PSG and PSA are labeled in the dashed line. M1 to M7: mirrors. HWP: half wave plate with fast axis at 22.5°. L1 to L7: lens. SLM: spatial light modulator. QWP: quarter wave plate with fast axis at 22.5°. Fast axis of the polarizer was fixed to be horizontal and of the rotating QWP were at 15.1°, 51.7°, 128.3°, and 164.9° respectively when measuring the polarization state [128]. .. 115
Figure 6. 3: (a) Fast axis angle distribution of the HWR. (b) The intensity profile when viewed between crossed polarizers. Image provided by Thorlabs. [131] 118
Figure 6. 4: Stokes parameters calculated from the polarimeter measurements of the output light after using −45° linear polarized light incident onto the vortex HWR. (a) S_1 (b) S_2 (c) S_3. S_1, S_2 and S_3 are all normalized between -1 to 1. The measurements show the expected distribution corresponding to a radially polarized light field. 119
Figure 6. 5: (a) The intensity distribution detected by the camera before polarization correction using a fast axis angle of 15.1° for the QWP (b) with 164.9° fast axis angle (c) corresponding orientation of the polarization state of the output light before correction, showing a near-radially polarized beam. (d) The intensity distribution after the QWP with 15.1° fast axis angle, when using the customized polarized beam to incident on the vortex HWR to restore the output to horizontal polarization. (e) with 164.9° fast axis angle (f) orientation of the polarization state of the output light after correction, showing near-zero angles across the beam. 120

Figure 6. 6: Stokes parameters measured by the PSA under different reconstructing situations. (a) − (c): S_1, S_2 and S_3 for horizontally polarized output. (d) – (f): Stokes parameters for 45° linearly polarized output. (g) – (i): Stokes parameters for right circular polarized output 121

Figure 6. 7: (a) Birefringent effects of a stressed plastic plate illuminated by a lamp when viewed through cross polarizers with white light illumination. (b) Plotted polarization ellipse of the output before correction when using vertical polarized illumination. (c) Polarization ellipse under horizontal polarization state reconstruction (d) Polarization ellipse under 45° linear polarization state reconstruction. (e) Plotted polarization ellipse of the output light under right circular polarization state reconstruction. 123

Figure 6. 8: (a) Schematic of the liquid crystal device, the birefringence of the dynamic region can be changed according to drive voltage while the static region does not. (b) Output light polarization state of each sub-region representing on Poincaré Sphere before correction, at U = 1.8 volts. (c) Polarization state distribution after correction at U = 1.8 volts. (d) Polarization state distribution before correction at U = 2.5 volts. (e) Polarization state distribution after correction at U = 2.5 volts. 125

Figure 6. 9: (a) Microscope image of the mouse brain tissue sample. (b) Intensity image recorded by the camera of the brain tissue sample before correction at the rotating QWP of 128.3°. (c) Intensity image of the sample after correction. (d) − (f) S_1, S_2 and S_3 of the polarization state after the brain tissue when using horizontal polarized illumination before correction. (g) − (i) S_1, S_2 and S_3 of the polarization state following correction. 127

List of Tables

Table 2. 1 Jones vectors of different polarized light 20
Table 2. 2 Jones matrix of some polarizers 21
Table 2. 3 Jones matrix of phase retarders 21
Table 2. 4 Stokes parameters of different polarized light. 23
Table 2. 5 Müller Matrix of phase retarder with the fast axis orientated at the angle of θ. 26

Table 3. 1 Noll's index numbering 46
Table 3. 2 First and second derivative of the each Zernike mode 58

Table 4. 1 Diffraction efficiency comparison with different SLM calibration and different blazed grating periods 80

List of Abbreviations

2D	2-dimentional
3D	3-dimentional
AO	Adaptive optics
APC	Adaptive polarization control
BS	Beam splitter
CCD	Charge coupled device
CMOS	Complementary metal oxide semiconductor
DM	Deformable mirror
FFT	Fast Fourier Transform
HWP	Half wave plate
LC	Liquid crystal
OPL	Optical path length
PBS	Polarization beam splitter
PGV	Pixel grayscale value
PSA	Polarization state analyzer
PSG	Polarization state generator
PTT	Piston, tip and tilt
QWP	Quarter wave plate
RI	Refractive index
SLM	Spatial light modulator

Chapter 1 Introduction

1.1 Background and motivation

Adaptive optics (AO) is an important technology for a wide range of applications including bio-medical imaging [1-3], retinal imaging [4, 5], astronomy[6] and various kinds of microscopies [7-12]. This concept was first introduced by Horace W. Babcock to improve astronomical imaging through closed-loop correction of wavefront errors. In microscopy, AO helps to improve image quality that is compromised by imperfect optics and distorted wavefronts, which are defined as aberrations [13]. AO corrects the aberration by generating a conjugated wavefront that compensates the errors.

In its conventional implementation, the AO system includes a wavefront sensor to detect the distorted wavefront and a correction element to generate the conjugated wavefront. There are also other AO methods, e.g. “sensor-less” AO has been developed that does not use a wavefront sensor, but instead permits the inference of the correction aberration from a sequence of aberrated images. Changing wavefront shape is the key technology achieved through correction devices such as deformable mirrors (DM) and spatial light modulators (SLM) [14, 15]. DM is a flexible mirror whose shape can change according to electrical voltage etc. whereas SLM is a liquid crystal array device, in which each pixel can be regarded as a phase retarder.

There are several advantages to use a DM comparing to SLM as correction element, such as wavelength and polarization independent, but sometimes there is variability between devices and performance may not be as specified. In this case, when one buys a DM, it usually needs

calibration in the specific experiment. Therefore, to provide a simple and realizable way to characterize the performance of the DM is essential. This is explored in the first part of this thesis.

While the traditional concept of AO has concerned phase aberrations, phase is not the only property of light that can be controlled using adaptive elements. Certain microscopes have been found to be more sensitive to small levels of phase aberration than others. These include super-resolution microscopes, such as Stimulated Emission Depletion (STED) microscopy, Structured Illumination Microscopy (SIM), and single molecule localization fluorescence microscopy [8, 13, 16, 17]. These microscopes are not only sensitive to phase aberrations, but also to small errors in the polarization state at the focus. Polarization aberrations are the deviation of the polarization state from its desired form. Such polarization errors can be introduced by optical elements, Fresnel effects at interfaces, scattering and birefringence in specimens. Therefore, to develop an adaptive polarization control system is the second work in this thesis that is expected to be beneficial for these polarization sensitive imaging systems.

While polarization modulators and various polarimeters have already been developed, we do not yet have closed loop polarization correction systems for complex beams. Hence, there is a need to design a system for adaptive polarization control. Apart from that, most of the polarization modulators change the whole beam polarization state instead of changing the different parts with different states. SLMs are commonly used for phase modulation in AO. It also can be used to change the polarization state if the input light has a different polarization. Since calibration for phase and polarization modulation is different, full calibration is needed. Therefore, in the second part of this thesis, I introduce a method to fully calibrate SLM and followed this with an adaptive polarization control (APC) system that consists of polarization modulation and measurement, which is able to change and measure the different regions of

polarization across a single beam. This system is demonstrated to have the ability to extract the birefringent feature of the disturbance in the system and reconstruct the polarization state of the output light.

1.2 Objective

This thesis aims to better understand the capability and limitation of adaptive optics for phase correction and further extend the possibility of AO to polarization control.

The work in this thesis contains the following objectives:

1) To be able to control adaptive elements (particularly DMs) to enable aberration correction using an appropriate mathematical model (like Zernike modes) and to understand the capabilities and limitations of the DM correction abilities.

2) To understand and develop the strategy to do full polarization modulation and measurement.

3) To fully calibrate the key device, the SLM, for polarization generation.

3) To build a system which can realise adaptive polarization control, *i.e.* dynamically reconstruct the polarization state with the presence of the birefringent disturbance.

1.3 Organization of this thesis

This thesis is organized in 7 chapters, with the opening chapter, Chapter 1, the state-of-art technology, and the challenge, limitation on the AO in microscopy are introduced. The understanding of the AO on phase control and the need for the AO on polarization control are the motivation of this thesis work.

1.3 Organization of this thesis

A brief introduction on the physics of light is first given in Chapter 2, about phase and polarization. In Section 2.1, the mathematical representation of the light, the wavefront and the optical aberration are given. It is followed by introducing of how the light propagates in free-space and in crystals to describe polarization in Section 2.2. Then polarization of the light is discussed in detail from the definition, to the different polarized light, to the representation ways including Jones calculus, Stokes calculus and the Poincaré Sphere.

Then the concept of adaptive optics is briefly reviewed. The methods and elements to correct optical aberration by using AO is described in Section 2.3. Based on the mathematical decomposition of the aberration, the correction device, generally the deformable mirror and spatial light modulator, to make compensation for the wavefront aberration are introduced. To know the capability and limitation of a correction device on the AO phase correction, in the first part of this thesis, DM characterization is demonstrated in Chapter 3.

In Chapter 3, a segmented deformable mirror is characterized. The wavefront generated by the DM was extracted from the interferogram. The interferometric technique to extract the phase is firstly reviewed in Section 3.1. System setup is introduced in Section 3.2 and the detailed correction results are discussed in Section 3.3. The results describe the correction range, which is measured by how accurately the DM could generate a Zernike mode aberration with different amplitudes. The comparison result of each mode is listed with the amplitude of 0.5 μm *rms* and 2 μm *rms* respectively. The ideal wavefront and measured wavefront are compared and the errors are calculated.

Prior to the build up of the APC system, since the SLM is used as the key device to in the PSG, full calibration is needed since it is found that the calibration for polarization modulation should be different from the phase modulation. In Chapter 4, a comprehensive calibration is presented

of the SLM. The difference of the phase and retardance calibration from a mathematical perspective is addressed first. In Section 4.2, the calibration set-up and methodology are shown. The spatial variation and how the phase modulated by the SLM changes with the voltage are then analysed. Detailed data processing and analysing algorithm are given in Section 4.3. The discussion on the interesting phenomenon that different regions have different reaction for the same voltage are also given. At the end of the section, the diffraction efficiency comparison between using the calibration data provided by the company and by our measurement technique is shown. Next for the retardance calibration, the same set-up was used but with a different configuration.

In Chapter 5, the PSG and PSA are introduced. The methodology of full polarization control from the double pass of the SLM for the PSG are first presented. In Section 5.1, the experimental setup are shown and the system alignment method for the double pass system are introduced. Then misalignment effect of the liquid crystal in the double pass SLM on the polarization modulation in the PSG was simulated. It proves that the small angle deviation of the liquid crystal could bring large distortion on the modulated polarization. In Section 5.2, some polarimeter techniques for PSA including the Sagnac interferometer and Stokes polarimeter are then reviewed. Two polarimeters have been built and tested based on these techniques in this thesis. A modified Sagnac interferometer is first presented including the setup and operation principle. Thereafter, an optimized Stokes polarimeter was tested. Finally, after a thorough comparison between the two polarimeters and the considering the suitability for the APC system, the optimized Stokes polarimeter was chosen as the PSA.

In Chapter 6, the functionality of the APC system is demonstrated. In Section 6.1, the methodology to reconstruct the polarization state is presented when there is a birefringent disturbance in the system. Based on that, the APC system was built by combing the PSG and

PSA. Followed by the system design and setup, four different kinds of disturbance were tested including a vortex half wave retarder, a stressed plastic plate, a customized liquid crystal device and a mouse brain tissue. A sequence of measurements were taken before polarization reconstruction, the number of which depends on the degree of prior information that was known about the disturbance. The testing results shown in Section 6.3 proves that the APC system is able to reconstruct the polarization state even when there is a dynamic and spatial birefringent variant disturbance in the system.

The summary of this thesis is given in Chapter 7, as well as the limitations and potential future work.

Chapter 2 Background

In this Chapter, the background knowledge related to the work in this thesis is given. The mathematic representation of an optical wavefront and aberrations are first introduced. Since the aberration is not only concerned on phase distortion here but also polarization error as well, the polarization of light is introduced in the second section. In the end, AO technology to correct the aberration is briefly reviewed.

2.1 Optical wavefront

Light is an electromagnetic wave. Its wave-like properties were illustrated by Young's famous interference experiment [18], which is shown in Figure 2.1. When studying the light property or describing the light propagation in optical system design, one could use geometric optics or wave oscillation optics. The geometrical representation is used for paraxial optics or in the phase of the optical design process.

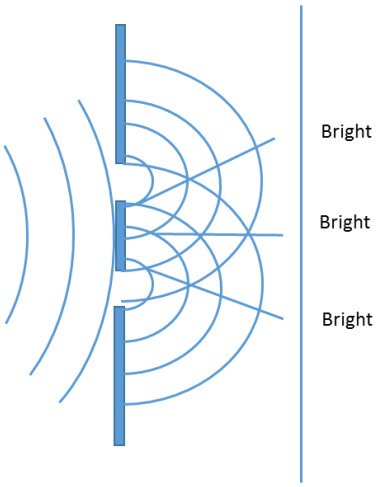


Figure 2. 1: Schematics of Young's double slit interference experiments [18].

2.1.1 Optical field

In order to understand the behaviour of light waves, one can model mathematically how waves are generated from oscillating charges. The steady state of a mono-chromatic wave field could be regarded as the harmonic motion at a constant oscillation frequency ω. The equation to describe the wave field can be written as [19]:

$$\vec{W}(p,t) = A(p)\cos(\omega t - \vec{\varphi}(p)) \tag{2.1}$$

where p is the position of a point in the field; t is the time; $A(p)$ is the amplitude profile and $\vec{\varphi}(p)$ is the phase profile in the spatial domain. $A(p)$ and $\vec{\varphi}(p)$ are both independent with time t. When writing Eq. (2.1) in the complex form, it becomes:

$$W(p,t) = A(p)e^{i(\omega t - \varphi(p))} = A(p)e^{i\omega t}e^{i\varphi(p)} \tag{2.2}$$

The spatial term and temporal term in Eq. (2.2) are independent. When discussing the wave spatial distribution, as the time factors are always the same, it can be ignored and then Eq. (2.2) becomes:

$$W(p) = A(p)e^{i\varphi(p)} \tag{2.3}$$

Eq. (2.3) shows that to describe the optical field in the spatial domain, it is important to know the two parameters, the amplitude and the phase.

2.1.2 Wavefront

A wavefront of wave is the surface which connects all the points that have the same phase in the spatial domain. If the wavefront is flat, it is called a plane wave. If the wavefront forms part of a spherical surface, it is called a spherical wave [20].

The amplitude of a homogeneous plane wave is a constant whereas the phase is a linear function of the coordinate of the position. The phase can be written as:

$$\varphi(p) = \vec{k} \cdot \vec{r} + \varphi_0 \tag{2.4}$$

where $\vec{k}$ is the wave vector, and $\vec{r}$ is the position vector, φ_0 is the initial phase at the origin point. The magnitude of *k*, $k_0 = 2\pi/\lambda$, where λ is the wavelength of the wave as $\lambda = 2\pi v/\omega$ and *v* is the magnitude of the phase velocity. Eq. (2.4) also can be written in complex form as $W(p) = Ae^{i(\vec{k}\cdot\vec{r}+\varphi_0)}$. For the spherical wave, the amplitude is no longer a constant. It is inversely proportional to the distance between the point and the light source whereas the phase is proportional to that distance, namely, $A(p) = A_0/r$, $\varphi(p) = k_0 r + \varphi_0$, where A_0 is the amplitude when the light source is one unit distance away from the point and *r* is the distance between the light source and that point. Therefore, the complex form of the wavefront of the spherical wave is: $W(p) = \frac{A_0}{r} e^{i(k_0 r+\varphi_0)}$.

A plane wave is generally called collimated light, where the wavefronts are flat and parallel. When it propagates through a lens, the lens can transfer it to a converging or divergent spherical wave. The phase transfer function of a single thin lens is [21]:

$$T(x,y) = \exp\left(-ik_0 \frac{x^2+y^2}{2F}\right) \tag{2.5}$$

where $= \frac{1}{(n-1)\left(\frac{1}{r_1}-\frac{1}{r_2}\right)}$, r_1 and r_2 are the radius of the curvature of the front and back of the lens surface respectively, n is the refractive index of the lens. F is the focal length of the lens. When applying the transfer function to a plane wave with the amplitude constant A_1 and phase factor 1, namely, $W_1(x,y) = A_1$, the wave after the lens is:

$$W_2(x,y) = T(x,y)W_1(x,y) = A_1 \exp\left[-ik_0 \frac{x^2+y^2}{2F}\right] \tag{2.6}$$

It is seen that the phase factor of $W_2(x,y)$ is a spherical wave [18]. Figure 2.2 shows the schematics of this process.

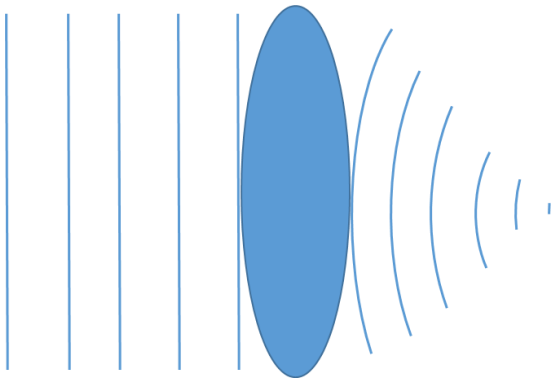


Figure 2. 2: A single positive lens transfers a plane wave to a converging spherical wave.

2.1.3 Optical aberration

Aberrations as wavefront distortions arise from imperfect optical elements or refractive index (RI) variations. Aberrations are the reason why light does not converge to (or diverge from) a certain point after passing through an imaging system, or equivalently when the wavefront deviates from its ideal state. Optical elements can cause aberrations like spherical aberration, coma, etc. [22]. Spherical aberration forms because of the non-spherical curved surfaces of the

spherical lens and it does not focus all rays on the same point. Different transmission media would cause different reasons to distort the wavefront, like uneven RI, atmospheric turbulence, surface deviation of a mirror, temperature stress and strain on the optical elements, as well as some mounting deflection [23, 24]. When considering microscopy, a mismatch of the index between the coverslip and the specimen will cause spherical aberration [25].

Another source of aberration in microscopy is introduced by the biological specimens when one wants to focus deep in the structure. Since the 3-dimensional structure and thick tissue have spatially varying RI, the impact on imaging can be significant [26, 27]. Light travels at different speeds through different RI so parts of the wavefront are delayed relative to others when passing through the specimen. These aberrations get more complex and larger when focussing deeper as aberration can be accumulated. Therefore, they have the effect of reducing the contrast and resolution of microscope images.

It is helpful to have a mathematical description of optical aberrations. Zernike polynomials are a convenient set of circular or annular basis functions used to represent an arbitrary phase distribution in a mathematical form. A sum of a number of polynomials, each with its own weighting, can be used to represent the total wavefront aberration [28, 29]. The Zernike polynomials are an infinite set of functions consisting of two variables, the radial coordinate ρ and the angle coordinate θ, representing the polar coordinates in the normalised pupil of the system. The functions are orthogonal is the unit circle [28, 30-34]. Therefore, the aberration can be represented as:

$$W(\rho,\theta) = \sum_{n=0}^{\infty} \sum_{m=0}^{n} A_n^m Z_n^m \tag{2.7}$$

where n and m to represent the highest order of the radial variable and angle variable respectively. A_n^m is the coefficient of each Zernike term. Then Z_n^m can be written as:

$$Z_n^m(\rho,\theta) = \begin{cases} N_n^m R_n^{|m|}(\rho)\cos m\theta\,; & m \geq 0 \\ -N_n^m R_n^{|m|}(\rho)\sin m\theta\,; & m < 0 \end{cases} \tag{2.8}$$

where the radial function $R_n^{|m|}(\rho)$ is:

$$R_n^{|m|}(\rho) = \sum_{s=0}^{(n-|m|)/2} \frac{(-1)^s (n-s)!}{s!\,[0.5(n+|m|)-s]!\,[0.5(n-|m|)-s]!}\rho^{n-2s} \tag{2.9}$$

The normalization term N_n^m :

$$N_n^m = \sqrt{\frac{2(n+1)}{1+\delta_{m0}}} \tag{2.10}$$

where δ_{m0} is the Kronecker delta, namely, when $m = 0$, $\delta_{m0} = 1$ and when $m \neq 0$, $\delta_{mn} = 0$. Generally, the wavefront is asymmetric and that is why the Eq. (2.8) has both sine and cosine terms. Figure 2.3 shows the Noll's index in ordering the representation of optical aberrations in the Zernike terms [35]. Note that the normalisation of the functions used here ensures that the function has a root-mean-square (rms) value of 1.

Radial degree (n)	Azimuthal frequency (m) 0	1	2	3	4	5
0	$Z_1 = 1$ Constant					
1		$Z_2 = 2r\cos\theta$ $Z_3 = 2r\sin\theta$ Tilts (Lateral position)				
2	$Z_4 = \sqrt{3}(2r^2-1)$ Defocus (Longitudinal position)		$Z_5 = \sqrt{6}r^2\sin 2\theta$ $Z_6 = \sqrt{6}r^2\cos 2\theta$ Astigmatism (3rd Order)			
3		$Z_7 = \sqrt{8}(3r^3-2r)\sin\theta$ $Z_8 = \sqrt{8}(3r^3-2r)\cos\theta$ Coma (3rd order)		$Z_9 = \sqrt{8}r^3\sin 3\theta$ $Z_{10} = \sqrt{8}r^3\cos 3\theta$		
4	$Z_{11} = \sqrt{5}(6r^4-6r^2+1)$ 3rd order spherical		$Z_{12} = \sqrt{10}(4r^4-3r^2)\cos 2\theta$ $Z_{13} = \sqrt{10}(4r^4-3r^2)\sin 2\theta$		$Z_{14} = \sqrt{10}r^4\cos 4\theta$ $Z_{15} = \sqrt{10}r^4\sin 4\theta$	
5		$Z_{16} = \sqrt{12}(10r^5-12r^3+3r)\cos\theta$ $Z_{17} = \sqrt{12}(10r^5-12r^3+3r)\sin\theta$		$Z_{18} = \sqrt{12}(5r^5-4r^3)\cos 3\theta$ $Z_{19} = \sqrt{12}(5r^5-4r^3)\sin 3\theta$		$Z_{20} = \sqrt{12}r^5\cos 5\theta$ $Z_{21} = \sqrt{12}r^5\sin 5\theta$
6	$Z_{22} = \sqrt{7}(20r^6-30r^4+12r^2-1)$ 5th order spherical		Z_{23} Z_{24}		Z_{25} Z_{26}	

Figure 2. 3 Noll's index for Zernike polynomials [35].

2.2 Polarized light

As described above, light is electromagnetic radiation in which the electric and magnetic fields oscillate in a transverse manner, perpendicular to the direction of propagation, as shown in Figure 2.4. The orientation of the electric field vector is called the polarization of the light.

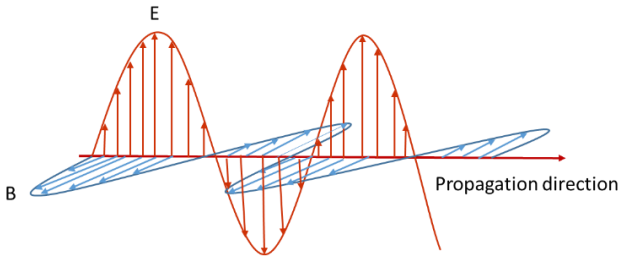


Figure 2. 4: Light propagation schematic showing the electric (E) and magnetic (B) fields.

In Cartesian coordinates, assuming a plane polarized wave is propagating along the *z* axis, its three electrical field components are:

$$E_x = E_{x0}\cos(\omega t - kz + \delta_x)$$

$$E_y = E_{y0}\cos(\omega t - kz + \delta_y)$$

$$E_z = 0 \tag{2.11}$$

in which E_{x0}, E_{y0} are the amplitude, δ_x and δ_y are the initial phase of E_x and E_y, k is the wave index or spatial frequency and ω is the angular frequency. The end of the resultant electrical vectors forms an ellipse during the propagation. It can be represented as:

$$\frac{E_x^2}{E_{x0}^2} + \frac{E_y^2}{E_{y0}^2} - 2\frac{E_x}{E_{x0}}\frac{E_y}{E_{y0}}\cos\delta = \sin^2\delta \tag{2.12}$$

where $\delta = \delta_x - \delta_y$. It can be seen that, the amplitude ratio between E_{x0} and E_{y0} and the phase difference δ can decide the ellipse direction and shape which in effect defines the polarization state.

Polarization can be classified as linear polarization, circular polarization or elliptical polarization. When the electrical field direction is always in the same plane that is perpendicular to the propagation direction, and the normal does not change with time, this state is called linear polarization. In this case, the projected electrical field in this plane is a line. If E_x is 0, only the lateral wave oscillates. This is vertical polarized light. The same idea can be also applied to the horizontal polarized light. They are two special cases of linearly polarized light. If $\delta = \pm k\pi$, the oscillation orientation is still a line but the orientation of this line depends on the amplitude ratio of E_{x0} and E_{y0}. If $E_{x0} = E_{y0}$, the plane is oriented at 45° to the *x*-axis.

Circular polarized light has the same amplitude when projected in the plane perpendicular to the propagation but the direction is rotated with time, alternatively, $\delta = \pm\pi/2$ and $E_{x0} = E_{y0}$. If $\delta = -\pi/2$, it is called left-hand circular polarized light and if $\delta = \pi/2$, it is called right-hand circular polarized light. For elliptical polarization, not only the direction of the electrical field projected on the plane perpendicular to the propagation changes with time, amplitude also changes [36]. Obviously, linear polarization and circular polarization are special cases of elliptical polarization.

Figure 2.5 shows the different polarization state with different δ but with $E_{x0} = E_{y0}$.

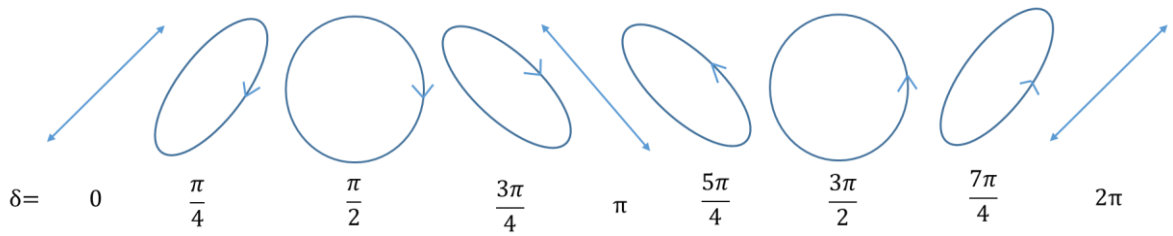


Figure 2. 5: Different polarization states with different δ, $\delta = \delta_x - \delta_y$.

Natural light is usually a random mixture of polarizations and is referred to as "unpolarised" [37]. In turn, laser sources are typically linear polarized. In reality, most sources are to some degree partially polarized, not perfectly polarized or unpolarised. A polarizer can be used to filter out one component of unpolarised light to give linearly polarized output. Figure 2.6 shows the schematics of how a transmission polarizer works.

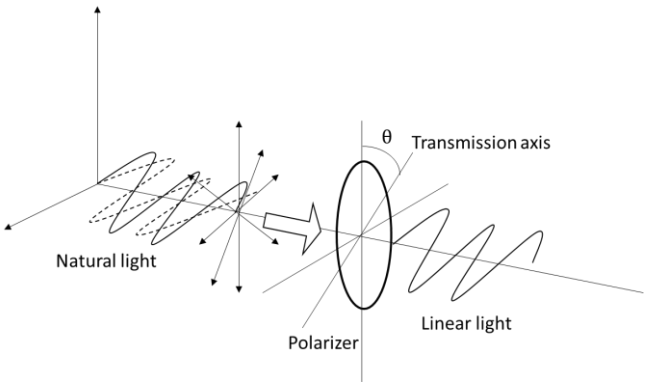


Figure 2. 6: Light transmitted through to a polarizer becomes linearly polarized.

2.2.1 Light propagation in crystals

Phase differences occur due to variations in the optical path length (OPL), which is defined as $OPL = \int n\, ds$, where n is the refractive index of the media and s is the distance that the light travels. If light comes from a point source, passing through an isotropic media, it has the same speed at each direction which is $v_0 = c/n$. It forms a spherical wavefront with a radius of vt. When the material is anisotropic, like many crystals, the light property will be changed. These

materials have a refractive index that depends on the propagation direction of the light and the orientation of the electric field vector [38], so they are called birefringent. Many crystals are birefringent including quartz, Iceland spar etc.

When collimated light propagates in a birefringent crystal, it is likely that the light is split into two [39]. One of them propagates in the original direction, whereas the other one deviates to another direction. The one which subjects to the ordinary propagation is called ordinary ray, *o*-ray; the one with deviation is called the extraordinary ray, *e*-ray. The *o*-ray propagates in the same way as in an isotropic material, so the velocity at each direction is the same. The *e*-ray has a different speed in different directions. It would have the same speed with the *o*-ray along the optical axis, but have a different speed along the axis which is perpendicular to the optic axis [40]. The refractive index is defined as $n = c/v$, so for the *o*-ray, the refractive index n_o is $n_o = c/v_o$. For the *e*-ray, it is not suitable to show its optical property by using a single refractive index but generally the refractive index is defined as $n_e = c/v_e$, where v_e is the velocity of the light traveling along the axis perpendicular to the optical axis [41].

Generally, a uniaxial material is defined to have only one optical axis whereas a biaxial material could have two or even more. A uniaxial negative material has a larger n_o than n_e while the uniaxial positive is the opposite. Figure 2.7 shows the comparison of the refractive index ellipsoids of different materials. One of the important applications of the birefringence is to make polarizing components with crystals that have different birefringent features.

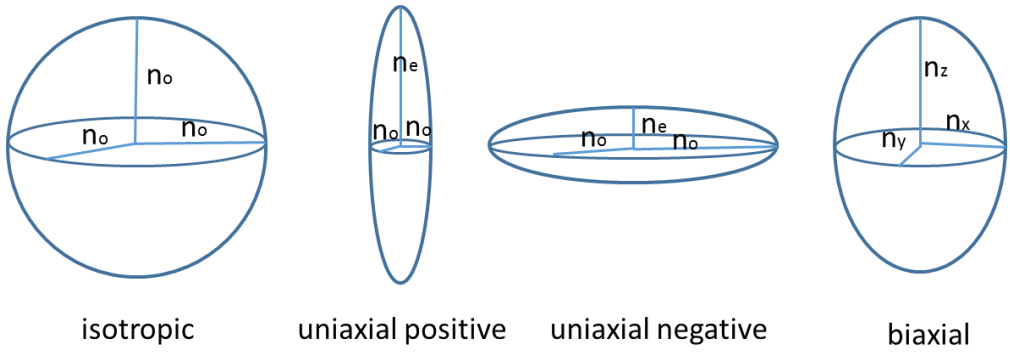


Figure 2. 7: Comparison of the RI ellipsoids of different materials. Isotropic: $n_x = n_y = n_z = n_o$; uniaxial positive: $n_o < n_e$; uniaxial negative: $n_o > n_e$; biaxial: n_x, n_y, and n_z are all different.

2.2.2 Polarizing components

As described above, birefringent materials can separate the light into an *o*-ray and an *e*-ray. Therefore, it can be used to obtain two linear polarized light beams with perpendicular orientation. A polarization beam splitter is usually made of crystals with this birefringence feature.

Another application of the birefringent crystal is phase retarders. The surface of a phase retarder is parallel to its optical axis. When collimated light is incident normally onto it, the *o*-ray and *e*-ray have different propagation speed v_o and v_e due to the different effective refractive indices, where $v_o = c/n_o$ and $v_e = c/n_e$. If the thickness of this retarder is d, the OPL of *o*-ray is $n_o d$ and that for *e*-ray is $n_e d$. Therefore, the phase difference between the input and output light of *o*-ray and *e*-ray are:

$$\delta_o = \frac{2\pi}{\lambda} n_o d$$

$$\delta_e = \frac{2\pi}{\lambda} n_e d \tag{2.13}$$

where λ is the wavelength of the incident light. Hence, the retardance difference between the *o*-ray and the *e*-ray is:

$$\delta = \delta_o - \delta_e = \frac{2\pi}{\lambda}(n_o - n_e)d \tag{2.14}$$

The retardance difference is not only proportional to the index difference but also to the thickness of the retarder. Therefore, any retardance can be obtained by selecting different *d*. If the retardance is changed by the phase retarder, the polarization state of the light is also changed. Hence, a phase retarder is always used to change the light polarization. The axis which has the lowest refractive index is called fast axis. The most widely used retarders are half-wave plate (HWP) and quarter-wave plate (QWP). The thickness of a HWP is subject to $(n_0 - n_e)d = \pm\lambda/2$, hence $\delta = \pm\pi$; where the thickness for a QWP is subject to $(n_0 - n_e)d = \pm\lambda/4$ and $\delta = \pm\pi/2$.

In addition to the crystal with birefringent features, some materials can absorb the electromagnetic radiation with specific oscillation orientation. When light is incident on such a material, it can absorb most of the energy which oscillates parallel to the absorbing molecules. However, it absorbs only weakly light that oscillates perpendicular to the molecules whereby most of the light can pass. This is called diattenuation. One can use this property to make a polarizer, which is able to generate linear polarized light with different orientation by rotating the crystal transmission axis.

The polarization state is mathematically described by three common ways, which are Jones vectors, Stokes parameters and the Poincaré sphere. Each of them has its own characteristics, are to the most part interchangeable, and one can choose one according to different requirements.

2.2.3 Jones calculus

In 1941, Jones first proposed a simple vector, known as the Jones vector, which is a 2×1 matrix to represent polarized light. It describes the polarization state with complex exponential number of the light on the propagation direction [42]. Its definition is:

$$\begin{bmatrix} E_x \\ E_y \end{bmatrix} = e^{i(\omega t - kz)} \begin{bmatrix} E_{x0} e^{i\delta_x} \\ E_{y0} e^{i\delta_y} \end{bmatrix} = e^{i(\omega t - kz)} e^{i\delta_y} \begin{bmatrix} E_{x0} e^{i\delta} \\ E_{y0} \end{bmatrix} \tag{2.15}$$

where, $\delta_x - \delta_y = \delta$, as the phase has period of 2π, the phase range is defined between –π and π. When $-\pi < \delta < 0$, the *x* component is behind the *y* component; on the contrary, when $0<\delta<\pi$, *y* component is behind the *x* component; when $\delta = 0$, *x* and *y* have the same phase; when $\delta = \pm\pi$, *x* and *y* field components have opposite phase.

The coefficient $e^{i(\omega t - kz)} e^{i\delta_y}$ is the mutual phase component. In addition to considering the product of two Jones matrices, in terms of the polarization transformation of an optical system, only the phase difference between the two components is of interest. Therefore, a common phase shift is ignored (although it is interesting to note that this phase is related to the phase aberration that is considered in other sections of this thesis). If the coefficient $e^{i(\omega t - kz)} e^{i\delta_y}$ is ignored, the polarized light can be represented as:

$$\vec{J} = \sqrt{E_{x0}^2 + E_{y0}^2} \begin{bmatrix} \cos\gamma \, e^{i\delta} \\ \sin\gamma \end{bmatrix} \tag{2.16}$$

in which, the $\cos\gamma = E_{x0} / \sqrt{E_{x0}^2 + E_{y0}^2}$, $\sin\gamma = E_{y0} / \sqrt{E_{x0}^2 + E_{y0}^2}$ and $\tan\gamma = E_{y0}/E_{x0}$ is the amplitude ratio. The normalized Jones vector is:

$$\overrightarrow{J_n} = \begin{bmatrix} \cos\gamma \, e^{i\delta} \\ \sin\gamma \end{bmatrix} \tag{2.17}$$

It has unit magnitude. For the linear polarized light, $\delta = \pm n\pi$; for circular polarized light, $\delta = \pm(2n+1)\pi/2$. However, Jones vectors can only describe fully polarized light and not partial polarization. Table 2.1 shows the Jones vectors of light with different polarization states.

Table 2. 1 Jones vectors of different polarized light

Polarization State	Horizontal polarized	Vertical polarized	+45° linear polarized	−45° linear polarized	Left-hand circular polarized	Right-hand circular polarized
Jones Vector	$\begin{bmatrix}1\\0\end{bmatrix}$	$\begin{bmatrix}0\\1\end{bmatrix}$	$\frac{1}{\sqrt{2}}\begin{bmatrix}1\\1\end{bmatrix}$	$\frac{1}{\sqrt{2}}\begin{bmatrix}1\\-1\end{bmatrix}$	$\frac{1}{\sqrt{2}}\begin{bmatrix}1\\-i\end{bmatrix}$	$\frac{1}{\sqrt{2}}\begin{bmatrix}1\\i\end{bmatrix}$

Since Jones vector can be utilized to represent the polarization, if light is incident on a retarder or a polarizer, the output Jones vector will typically be different from the input one. Therefore, the intermediate component can be represented as a Jones matrix to change the light polarization into a different state depending on the incident polarization:

$$\vec{J'} = J_{matrix}\vec{J} = \begin{bmatrix}J_{xx} & J_{xy}\\ J_{yx} & J_{yy}\end{bmatrix}\vec{J} \tag{2.18}$$

where $\vec{J}$ and $\vec{J'}$ are the input and output Jones vectors respectively. The Jones matrix of some polarizers are list in Table 2.2.

Table 2. 2 Jones matrix of some polarizers

Linear polarizer with different transmission axes orientation	Jones matrix
Horizontal axes	$\begin{bmatrix} 1 & 0 \\ 0 & 0 \end{bmatrix}$
Vertical axes	$\begin{bmatrix} 0 & 0 \\ 0 & 1 \end{bmatrix}$
+45° with the horizontal	$\frac{1}{2}\begin{bmatrix} 1 & 1 \\ 1 & 1 \end{bmatrix}$
−45° with the horizontal	$\frac{1}{2}\begin{bmatrix} 1 & -1 \\ -1 & 1 \end{bmatrix}$

When the fast axis of a phase retarder is horizontal or vertical, the off-diagonal elements of the Jones matrix is zero and it can be represented as $\begin{pmatrix} e^{i\delta_x} & 0 \\ 0 & e^{i\delta_y} \end{pmatrix}$, so the retardance $\delta = \delta_x - \delta_y$ will be introduced if the input light is not horizontal or vertical polarized. The Jones matrix is more complex if the fast axis is orientated with an angle to the *x* axis, Table 2.3 shows the Jones matrix of HWP and QWP with fast axis orientation of θ.

Table 2. 3 Jones matrix of phase retarders

Phase retarder with fast axis orientated at θ to the *x* axis	Jones Matrix
HWP	$e^{-\frac{i\pi}{2}}\begin{bmatrix} \cos^2\theta - \sin^2\theta & 2\sin\theta\cos\theta \\ 2\sin\theta\cos\theta & \sin^2\theta - \cos^2\theta \end{bmatrix}$
QWP	$e^{-\frac{i\pi}{4}}\begin{bmatrix} \cos^2\theta + i\sin^2\theta & (1-i)\sin\theta\cos\theta \\ (1-i)\sin\theta\cos\theta & \sin^2\theta + i\cos^2\theta \end{bmatrix}$
Any phase retarder with retardance of δ	$e^{-\frac{i\delta}{2}}\begin{bmatrix} \cos^2\theta + e^{i\delta}\sin^2\theta & \left(1-e^{i\delta}\right)e^{-i\varphi}\sin\theta\cos\theta \\ \left(1-e^{i\delta}\right)e^{i\varphi}\sin\theta\cos\theta & \sin^2\theta + e^{i\delta}\cos^2\theta \end{bmatrix}$

where δ is the phase difference introduced from δ_x and δ_y, and φ is the circularity. For HWP and QWP, $\varphi = 0$, since they are linear retarders.

2.2.4 Stokes parameters and Müller matrices

It is known that the polarized light is generally represented as elliptical polarization as described in Eq. (2.12), so it requires 3 independent parameters to describe it, such as the amplitudes E_{x0} and E_{y0} and the phase δ. Alternatively, one can use four measurable parameters known as the Stokes parameters to describe partially polarized light. They were proposed by Stokes in 1852 and are convenient as each one is a measurable intensity. The definition of the parameters S_0, S_1, S_2 and S_3 are as follows [43]:

$$S_0 = \langle E_x^2(t)\rangle + \langle E_y^2(t)\rangle$$

$$S_1 = \langle E_x^2(t)\rangle - \langle E_y^2(t)\rangle$$

$$S_2 = 2\langle E_x(t)E_y(t)\cos\left[\delta_y(t) - \delta_x(t)\right]\rangle$$

$$S_3 = 2\langle E_x(t)E_y(t)\sin\left[\delta_y(t) - \delta_x(t)\right]\rangle \tag{2.19}$$

where the $\langle E_x^2(t)\rangle$ is the time average of the amplitude square of the $E_x^2(t)$:

$$\langle E_x^2(t)\rangle = \frac{1}{T}\int_0^T E_x^2(t)\ dt \tag{2.20}$$

δ is phase, T is the time interval that is long enough that the time average integral is independent of T itself. When writing the above four parameters into a vector, the Stokes vector is:

$$\vec{S} = \begin{bmatrix} S_0 \\ S_1 \\ S_2 \\ S_3 \end{bmatrix} \tag{2.21}$$

The following table lists some typical polarized light Stokes parameters.

Table 2. 4 Stokes parameters of different polarized light.

Natural light	Horizontal linear polarized	vertical linear polarized	45° linear polarized	-45° linear polarized	Right-circular polarized	Left-circular polarized
$\begin{bmatrix}1\\0\\0\\0\end{bmatrix}$	$\begin{bmatrix}1\\1\\0\\0\end{bmatrix}$	$\begin{bmatrix}1\\-1\\0\\0\end{bmatrix}$	$\begin{bmatrix}1\\0\\1\\0\end{bmatrix}$	$\begin{bmatrix}1\\0\\-1\\0\end{bmatrix}$	$\begin{bmatrix}1\\0\\0\\1\end{bmatrix}$	$\begin{bmatrix}1\\0\\0\\-1\end{bmatrix}$

From the Eq. (2.19), it can be seen that the S_0 represent the intensity of the light; S_1 is the horizontal linear polarized light component; S_2 is the 45° linear polarized component and S_3 is the right circular polarized component. The orthogonal components which are the vertical linear, -45° linear and left circular are represented using negative S_1, S_2 and S_3, respectively.

For fully polarized light:

$$S_0{}^2 = S_1{}^2 + S_2{}^2 + S_3{}^2 \tag{2.22}$$

For partially polarized light:

$$S_0{}^2 > S_1{}^2 + S_2{}^2 + S_3{}^2 \tag{2.23}$$

For natural light: $S_1{}^2 = S_2{}^2 = S_3{}^2 = 0$. The degree of the polarization is defined as Eq. (2.24). Its value changes from 0 (non-polarized light) to 1 (fully polarized).

$$P = \frac{\sqrt{S_1^2 + S_2^2 + S_3^2}}{S_0} \tag{2.24}$$

Since the total intensity $S_0 = E_{x0}^2 + E_{y0}^2 = E_0^2$, here $E_{x0} = E_0 \cos\alpha$ and $E_{y0} = E_0 \sin\alpha$, where α is the angle of E_{x0} to the x axis. When substituting them into Eq. (2.19):

$$\vec{S} = S_0 \begin{bmatrix} 1 \\ \cos 2\alpha \\ \sin 2\alpha \cos\delta \\ \sin 2\alpha \sin\delta \end{bmatrix} \tag{2.25}$$

It can also be rewritten in the form of the polarization ellipticity angle χ and the polarization ellipse orientation angle ψ that are defined in Eq. (2.26) and (2.27) according to Eq. (2.12). Figure 2.8 shows the angle χ and ψ in the polarization ellipse.

$$\tan 2\psi = \frac{2E_{x0}E_{y0}\cos\delta}{E_{x0}^2 - E_{y0}^2} = \frac{S_2}{S_1} \tag{2.26}$$

$$\sin 2\chi = \frac{2E_{x0}E_{y0}\sin\delta}{E_{x0}^2 - E_{y0}^2} = \frac{S_3}{S_0} \tag{2.27}$$

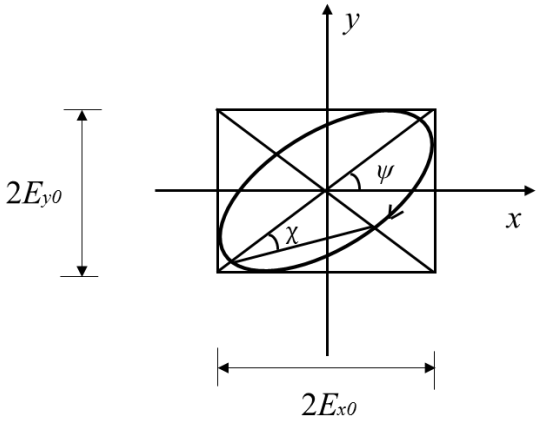


Figure 2. 8: Polarization ellipse.

Then the Stokes vector is described as:

$$\vec{S} = S_0 \begin{bmatrix} 1 \\ \cos 2\chi \cos 2\psi \\ \cos 2\chi \sin 2\psi \\ \sin 2\chi \end{bmatrix} \tag{2.28}$$

For the fixed total intensity *I*, the polarization state is decided by *P*, χ and ψ. In the Stokes subspace (S_1 S_2 S_3), the polarization of monochromatic light can be represented by a point with polar coordinates (P, 2ψ, 2χ), which is shown in Figure 2.9.

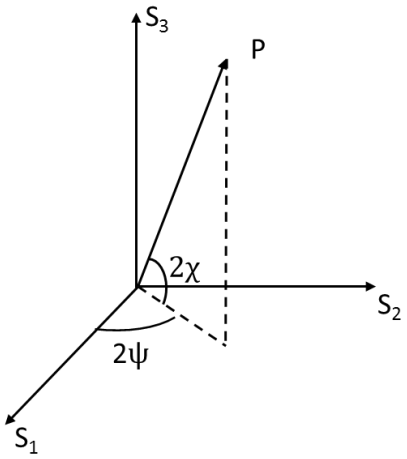


Figure 2. 9: Polarized point P in the subspace of S_1 S_2 S_3 represents its polarization state.

The characteristics of the polarization subspace can be easily obtained: first, the origin represent the non-polarization state which is $P = 0$; each point on the unit sphere surface all has $P = 1$, representing different full polarization state; finally, apart from the origin, each point inside the surface has $0 < P < 1$ representing the partial polarized light and the outside point which has $P > 1$ does not have physical meaning.

Similar to Jones matrix, the Müller matrix can be defined as the matrix that describes the transition from an input polarization state to an output polarization state. Assuming the Stokes parameters of the input light is $\vec{S}$, the Müller matrix is M, so the output polarized light $\overrightarrow{S'} = M\vec{S}$ or written as:

$$\overrightarrow{S'} = \begin{bmatrix} S'_0 \\ S'_1 \\ S'_2 \\ S'_3 \end{bmatrix} = M\vec{S} = \begin{bmatrix} m_{00} & m_{01} & m_{02} & m_{03} \\ m_{10} & m_{11} & m_{12} & m_{13} \\ m_{20} & m_{21} & m_{22} & m_{23} \\ m_{30} & m_{31} & m_{32} & m_{33} \end{bmatrix} \begin{bmatrix} S_0 \\ S_1 \\ S_2 \\ S_3 \end{bmatrix} \tag{2.29}$$

Table 2.5 shows the Müller matrix of some phase retarders whose fast axis is orientated at the angle of θ to the x axis.

Table 2. 5 Müller Matrix of phase retarder with the fast axis orientated at the angle of θ.

Phase retarder with fast axis orientated at θ to the x axis	Müller Matrix
HWP	$\begin{bmatrix} 1 & 0 & 0 & 0 \\ 0 & \cos 4\theta & \sin 4\theta & 0 \\ 0 & \sin 4\theta & -\cos 4\theta & 0 \\ 0 & 0 & 0 & -1 \end{bmatrix}$
QWP	$\begin{bmatrix} 1 & 0 & 0 & 0 \\ 0 & \cos^2 2\theta & \sin 2\theta \cos 2\theta & -\sin 2\theta \\ 0 & \sin 2\theta \cos 2\theta & \sin^2 2\theta & \cos 2\theta \\ 0 & \sin 2\theta & -\cos 2\theta & 0 \end{bmatrix}$
Any phase retarder with retardance of δ	$\begin{bmatrix} 1 & 0 & 0 & 0 \\ 0 & \cos^2 2\theta + \cos\phi \sin^2 2\theta & (1-\cos\phi)\sin 2\theta \cos 2\theta & -\sin\phi \sin 2\theta \\ 0 & (1-\cos\phi)\sin 2\theta \cos 2\theta & \sin^2 2\theta + \cos\phi \cos^2 2\theta & \sin\phi \cos 2\theta \\ 0 & \sin\phi \sin 2\theta & -\sin\phi \cos 2\theta & \cos\phi \end{bmatrix}$

2.2.5 Poincaré Sphere

In 1892, Poincaré realised that for the sphere corresponding to $S_0 = 1$, the points on the surface correspond states of fully polarized light. This is known as the Poincaré sphere. As shown in Figure 2.10, any point on this sphere has the longitude of 2χ and latitude of 2ψ [37]. Therefore, any point on the surface of the fully polarized light has the intensity of unit 1.

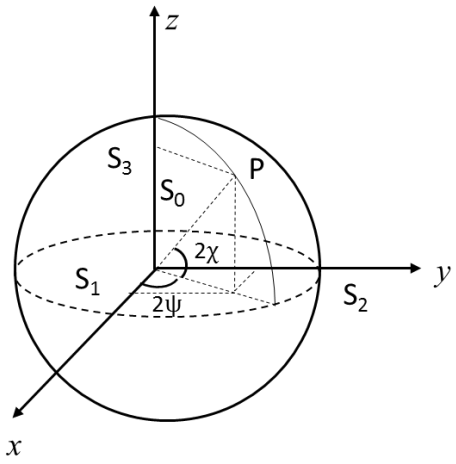


Figure 2. 10: Polarized light represented by the Poincaré sphere: $S_0 = 1$, $S_1 = \cos 2\chi \cos 2\psi$, $S_2 = \cos 2\chi \sin 2\psi$, $S_3 = \sin 2\chi$.

On the Poincaré sphere, the properties of polarized light can be summarised as:

1) If $\chi = 0$, P is on the equator representing the linear polarized light with different degree; if $\psi = 0$, the *e*-vector is horizontal polarized and when $\psi = \pi/2$, it becomes vertical polarized.
2) When $0 < \chi < \pi/4$, point P is on the upper hemisphere corresponding to the right elliptical polarized light; when $-\pi/4 < \chi < 0$, P is on the lower hemisphere corresponding to the left elliptical polarized light.
3) If P is on the N pole or S pole, it represents the right or left circular polarized light respectively.

In this case, wave with unit intensity has a corresponding point of each polarization state and vice versa. The physical meaning of the Stokes parameters becomes clearer by using the Poincaré sphere representation.

2.3 Adaptive optics

Aberrations cause image blur and therefore limit advanced development in many research areas. Adaptive optics is an important technology to address this problem. It helps to reduce the wavefront distortion and hence improve the optical system performance. AO for wavefront correction has broad applications including biology, astronomy and engineering.

2.3.1 Adaptive optics systems

An adaptive optics system correct for light distortions in the medium of transmission. The control system basically involves aberration measurement and aberrations correction.

Figure 2.11 shows a schematic of an open loop AO system that consists of the wavefront sensor, controller and correction element [44]. The solid line represents the light transmission while the dotted line represents the control signal. The wavefront sensor is like the eye of the adaptive system, detecting the wavefront error, φ, receiving the light coming from the input and sensing the static and dynamic errors. The wavefront controller is like the brain of the system, processing the signal from the wavefront sensor, calculating the wavefront errors and generating the signals that control the correction elements. The wavefront correction device is the execution element, adding to the wavefront the conjugate phase $-\varphi$ to make the corrected wave in conjugated planes.

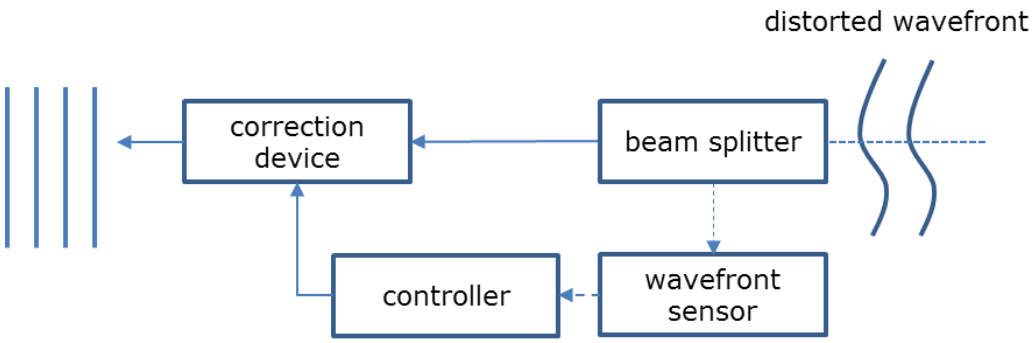


Figure 2. 11: General schematic of an adaptive optics system.

2.3.2 Correction device: deformable mirror and spatial light modulator

The wavefront correction device is the most important part of the AO system and it is usually either a DM or an SLM. The idea is to change the OPL, by changing either the distance travelled (like with a DM) or the refractive index (using an SLM). The DM and the SLM are regarded as phase modulation devices and are main components of AO systems.

Deformable mirror

DM is a flexible mirror device with mechanical actuators that provide adjustment of its surface in accordance with the wavefront measurements. Different types of DM like segmented DM and membrane DM are available commercially for various applications. Segmented DM consists of an array of small individual mirrors which are typically honeycomb structured; whereas a membrane DM is a type of mirror with flexible surface manufacturing mainly from thin polymer foil. The parameters of a DM include the number of the actuators, actuator stroke and the response time.

The segmented DM consists of multiple separate facets, each of which is a small mirror and is controlled by three actuators to control the degree of tilt so that it can change the wavefront shape. The position of each actuator is driven by external voltage. Segmented mirrors have

high reliability and fast response speed [45] and are widely used in astronomical telescopes and laser propagation through the atmosphere. However, for good performance a segmented DM is required with many small segment mirrors, which can be difficult to manufacture. Besides, the stepwise and large edge effect between the small mirrors also limits its application. Phasing between adjacent mirror segments is also important.

A common continuous mirror is the membrane DM that has a single membrane surface. There are different actuation methods that rely on static electrical force, electromagnetic forces or gas pressure etc. to drive the deformation of the membrane surface. The advantages of the membrane mirror include low surface density, easier fabrication and relatively low cost [46-48].

Spatial light modulator

Another important correction element is the SLM and liquid crystal on silicon (LCOS) device [49-51]. Generally, the SLM can change the light characteristics such as phase, amplitude, intensity, or polarization in the spatial distribution under external control that could be optical or electrical [34]. The SLM consists of many independent pixels that are arranged in a one or two dimensional array. Each pixel could be controlled by an independent voltage to change its own characteristic to modulate the light at that point. The SLM could be regarded as a device in which the optical parameter on each spot can be modulated according to our requirements. Liquid crystal SLMs modulate the light by using the electro-optical effect in the liquid crystal layer. By reorientation of the anisotropic liquid crystal molecules, the light experiences a different refractive index as described in Section 2.2.1. This is the origin of the phase modulation.

When the oscillation direction of the incoming light is parallel to the optical axis of the liquid crystal, due to the driving voltage, the molecules would be orientated along with the light

propagation direction. Only the refractive index of the liquid crystal is changed so the polarization of the light would not be changed but the phase would be modulated. However, when the incoming light has a different polarization orientation, the light polarization state will change. If polarizers are added in between of front and back substrate, the amplitude can be modulated. This is the principle of amplitude modulation.

In this thesis, the use of both DM and SLM will be explored in different ways and the detailed introduction to each element used in different applications will be given in the following chapters.

2.4 Summary

In this chapter, the phase and polarization of light are discussed. A wavefront is generally used to represent the phase of a propagating beam. Since the wavefront has distortion during propagation, AO is essential to correct the wavefront aberrations. The polarization of the light is also an important parameter. Followed by the introduction of what is the different polarized light, three general representations of polarization have been described including Jones calculus, Stokes calculus and Poincaré sphere. This chapter provides the fundamental knowledge of the following work in the thesis.

Chapter 3 Deformable Mirror Characterization

3.1 Introduction

The DM is probably the most commonly used wavefront correction device in AO. Its surface changes according to external forces to compensate wavefront aberrations. It is important to know a DM's capabilities (e.g. stroke, type of aberrations they can correct, dynamics, etc.). In this chapter, an interferometry based method to characterize a segmented DM is going to be introduced.

3.1.1 Introduction to interferometry and analysis

Interference is a unique characteristic of a wave. When two light waves that have a phase difference between each other are superposed, their intensity will be enhanced in some regions and impaired in other regions through the process of interference [52].

There is a condition to generate interference that is only if the two waves are mutually coherent, that is they have the same frequency, polarization and phase difference with the same vibration direction. If two lights are from two independent light source, it is not likely to have same frequency nor the fixed phase difference, so there will be no interference [53, 54].

3.1.2 Basic principle of interferometer

There are different kinds of interferometers for different kinds of applications. Usually, they first divide the light from the single light source into different waves. As these waves come from the same light source, when their original phase changes, the original phase of sub-waves also changes correspondingly so that their phase difference does not change within the coherence length of the source.

There are many types of interferometers [52]. The interferometer used in this chapter is the Twyman-Green interferometer. The Twyman-Green interferometer is a variant of Michelson interferometer and generally used to test optical elements. It is also used to calibrate the SLM in Chapter 4. The schematic is shown in Figure 3.1 (a). Another typical interferometer is the Sagnac interferometer, which is more stable than the Twyman-Green interferometer but it is hard to make the superposition of the two beams after the beam splitter. The schematic of the Sagnac interferometer is shown in Figure 3.1 (b). The Sagnac interferometer is going to be discussed in detail in Chapter 5 as a kind of PSA.

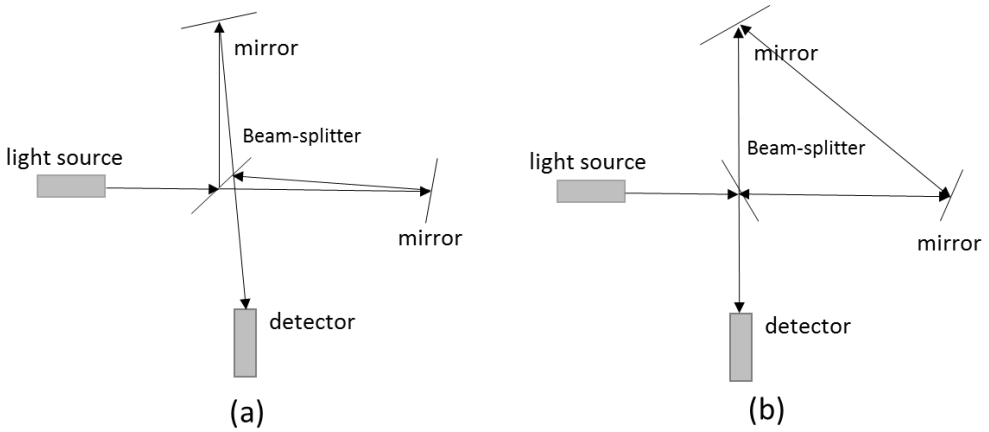


Figure 3. 1: Schematic of (a) Twyman-Green interferometer (b) Sagnac interferometer

3.1.3 Image analysis and phase extraction

Based on Twyman-Green interferometer setup, after obtaining the interference pattern, image analysis is needed to extract the phase information according to the fringes. There are several methods to extract the phase such as phase tracing, 2D Fourier transform and wavelet transform.

Phase tracing method is to sample the interference directly from the CCD and digitize the pattern, then do binarization and refining [55]. The 2D Fourier Fast Transform (FFT) is another widely used method [56]. This method is used in the work described in this thesis. According to the interference principle, when two waves interfere, the intensity is:

$$i(x,y) = a(x,y) + b(x,y)\cos[\varphi_0(x,y)] \tag{3.1}$$

where $a(x,y)$ is the background intensity, $b(x,y)$ is amplitude modulation of the fringes, $\varphi_0(x,y) = \varphi_s(x,y) - \varphi_R(x,y)$; $\varphi_s(x,y)$ is the phase distribution of the target light wave; $\varphi_R(x,y)$ is the reference wave phase distribution.

As the $a(x,y)$ and $b(x,y)$ are both unknown, it is impossible to obtain $\varphi_0(x,y)$ directly. Transformation of Eq. (3.1) is needed. If some tilt is added on the reference wave on both *x* and *y*, the fringes become denser in a specific direction with an angle with *x*, which is equivalent to creating spatial frequencies f_x and f_y. The interference intensity can be represented as:

$$\begin{aligned} i(x,y) &= a(x,y) + b(x,y)\cos[\varphi_0(x,y) + 2\pi f_0(x\cos\theta + y\sin\theta)] \\ &= a(x,y) + b(x,y)\cos[\varphi_0(x,y) + 2\pi f_x x + 2\pi f_y y] \end{aligned} \tag{3.2}$$

where f_0 is the spatial frequency, which is perpendicular to the fringes, $f_0 = \frac{1}{T}$, T is the spatial period of fringes.

3.1 Introduction

The rate of change of $a(x,y)$, $b(x,y)$ and $\varphi_0(x,y)$ is much slower than the change caused by the tilt. If one can calculate the $\varphi_0(x,y)$ and choose $\varphi_R(x,y)$ as a constant, the distribution function can be calculated.

In order to find $\varphi_0(x,y)$, Eq. (3.2) is rewritten as the complex expression:

$$i(x,y) = a(x,y) + c(x,y)e^{(j2\pi f_x x + j2\pi f_y y)} + c^*(x,y)e^{(-j2\pi f_x x - j2\pi f_y y)} \tag{3.3}$$

in which * represents conjugate and $c(x,y) = \frac{1}{2}b(x,y)e^{[j\varphi_0(x,y)]}$

The 2D Fourier Transform of the Eq. (3.3) is:

$$I(f_1,f_2) = A(f_1,f_2) + C\left(f_1 - f_x, f_2 - f_y\right) + C^*\left(f_1 + f_x, f_2 + f_y\right) \tag{3.4}$$

where capital letters represent functions in the frequency domain. $A(f_1,f_2)$is the background noise that is the zero order distribution function. $C(f_1 - f_x, f_2 - f_y)$ is the positive first order frequency distribution function and $C^*(f_1 + f_x, f_2 + f_y)$ is the negative first order frequency distribution. The positive first order centre is at (f_x, f_y) while the negative first order centre is at the $(-f_x, -f_y)$. Since the rate of change of $a(x,y)$, $b(x,y)$ and $\varphi_0(x,y)$ is much slower than the variances caused by f_x, f_y, the function of $I(f_1,f_2)$ has its peak value on (f_x, f_y) and $(-f_x, -f_y)$. If the carrier frequency is so large that the zero order can be separated from the first order, the positive first order frequency contains all the wave information. When a filter with its central frequency of (f_x, f_y) and proper bandwidth is adapted, $C\left(f_1 - f_x, f_2 - f_y\right)$ can be separated as shown in Figure 3.2.

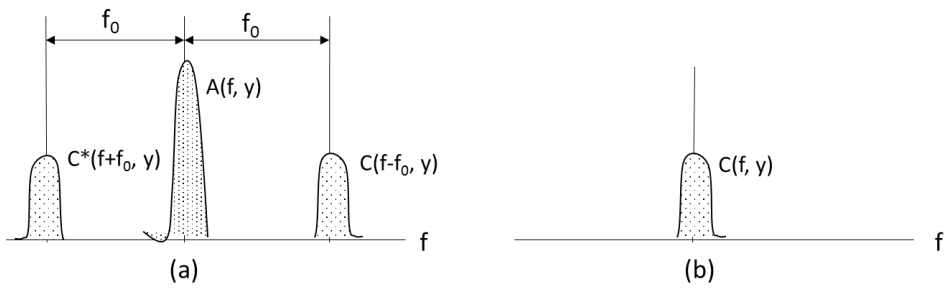


Figure 3. 2: (a) Components separated in the frequency domain (b) Select the first order frequency and shift it to the center, which is equivalent to demodulation.

Then, by shifting the $C(f_1 - f_x, f_2 - f_y)$ to the origin, one will get $C(f_1, f_2)$. After the inverse Fourier transform:

$$F^{-1}[C(f_1, f_2)] = c(x, y) = \frac{1}{2} b(x, y) e^{j\varphi_0(x,y)} \tag{3.5}$$

Knowing the $c(x, y)$, the phase distribution function $\varphi_0(x, y)$ can be found as

$$\varphi_0(x, y) = \arctan \frac{Im[c(x, y)]}{Re[c(x, y)]} \tag{3.6}$$

here, the $Re[c(x, y)]$ and $Im[c(x, y)]$ are the real and imaginary part of $c(x, y)$ respectively.

Since the arctangent gives values from $-\pi$ to π, the restored wave phase will have discontinuities. To remove these steps, phase unwrapping is needed. Generally used phase unwrapping algorithms include least squares, modal phase unwrapping, etc. [57, 58].

In reality, it may be hard to get the strictly parallel equally interval fringes. When the carrier frequency is a function of position rather than a constant, the wavelet transform, which combines both the spatial and frequency position characteristics, is a better way to solve this [59-61]. This may be a good toolkit in our future work to get accurate results.

3.2 Aim and experimental set-up

The DM is controlled to produce the Zernike polynomials described in Section 2.1.3 as these modes are regarded as a useful mathematical representation of aberrations. Characterization of the DM means determining the effective range and quality of reproduction of different aberrations, specifically the Zernike modes.

According to the above three identified features, it aims to find the operate range for the specific DM. A simple Twyman-Green interferometer was built. The setup and the corresponding schematic is shown in Figure 3.3. Basically, light coming from the laser source, was expanded through several telescope systems and split by a beam splitter. One beam came to the DM and the other to the reference mirror. These two reflected beams went through the splitter again. A lens was used after the beam splitter to focus the two lights to the camera, which was used to detect the interference. The lens was positioned to create an image of the DM aperture on the camera.

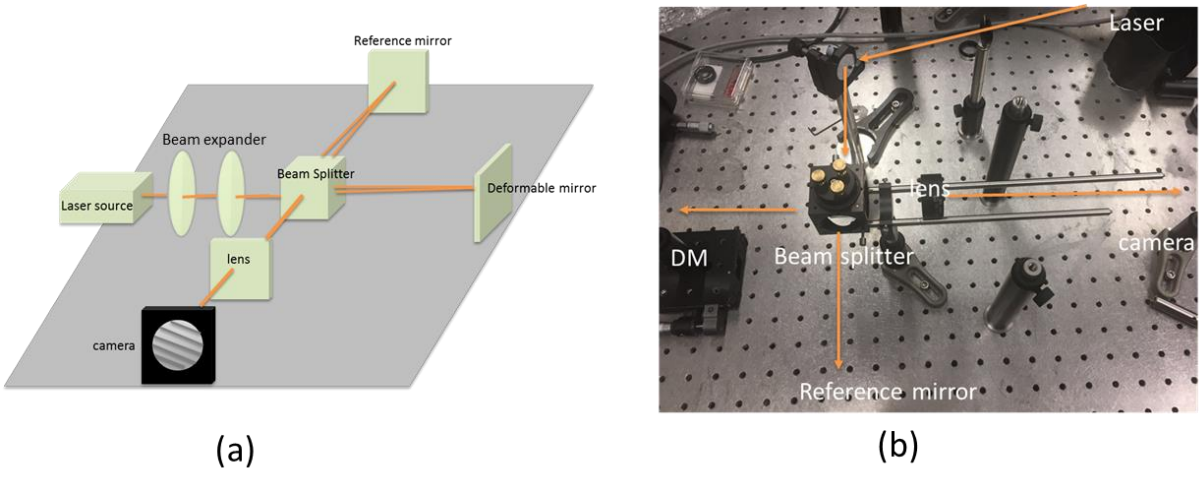


Figure 3. 3: (a) Experimental interferometer schematic (b) Real set-up.

In the simple interferometer built-up, the phase difference of the split waves was created by creating different travel paths between the beam splitter and the reference mirror and the DM,

respectively. The interference pattern detected by the camera depends on the position and shape of the reference mirror and the DM. If the position of the reference mirror was fixed, the interference pattern is only decided by the shape of the DM. In this case, it is able to characterize the DM by analysing the interference pattern on the camera.

The light source used was a Helium-Neon laser with a 15 mW max output at the wavelength of 632.8 nm (Melles Griot, 05-LHP-171). Due to the space limitation on the platform, the light source was diverted to the 50:50 beam splitter by using a flat mirror. The lens had a focus of 120 mm. The distance between the lens and the beam splitter was 50 mm and the distance between the beam splitter and the camera was 120 mm. The distance between the beam splitter and the reference mirror were 150 mm and the distance between the reference mirror and the DM and 250 mm respectively. The camera used to detect the interference pattern was a Thorlabs USB 2.0 CMOS camera (DCC1645C). The DM being characterized was of the segmented type from Iris AO, PTT111 Deformable Mirror, with 111 actuators and 37 piston-tip-tilt segments. Figure 3.4 shows the simple actuator and segment arrangement of this DM, while Figure 3.5 individually shows the ideal mirror shape after applying the Zernike modes 1–21 to the DM.

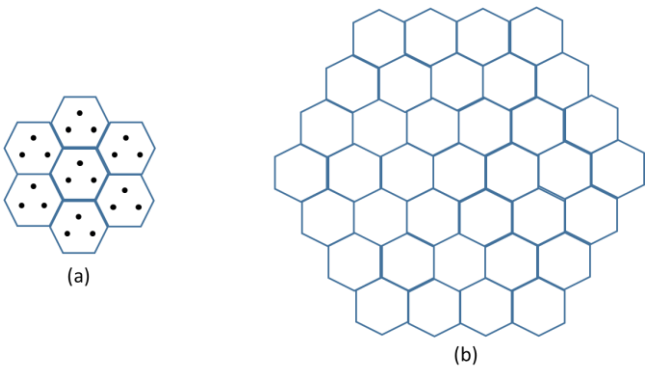


Figure 3. 4: (a) Each mirror segment was controlled by three actuators. (b) The whole mirror segments arrangement (hexagon).

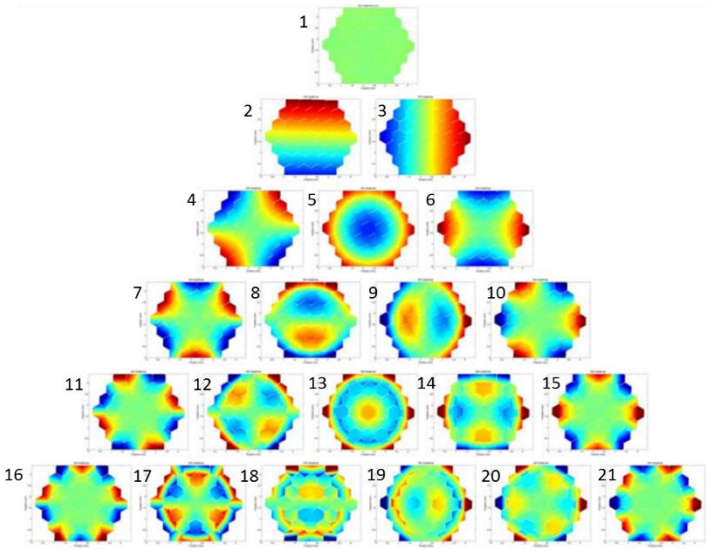


Figure 3. 5: Measured mirror shape for open-loop positioning of the Iris DM after applying different Zernike modes [62].

3.3 Results and analysis

3.3.1 System introduction

In this experiment, Matlab was used as our control interface. Although the DM and camera have their own control software, it is challenging to integrate them as a system for system control. The flowchart of the measurement process is shown in Figure 3.6. The DM was first initialized to its zero-state in which all of the segments are flat. Next, the camera was initialized and set corresponding specifics including the image greyscale, display and colour mode, exposure time etc. At this moment, one picture was first captured as the reference. The fringes on the reference image represent the interference of two reflected plane light wave from two flat mirrors. In order to modify the fringe distance, the reference mirror was manually tilted, which in effect allows control of the fringes in the interference pattern. Thereafter, the program entered into a loop to change the shape of the DM in different conditions. In the experiment, the shape was changed using Zernike modes to represent the aberration. In order to investigate

the DM performance for each Zernike mode, only one Zernike mode was set each time while keeping coefficients of other modes at zero [63].

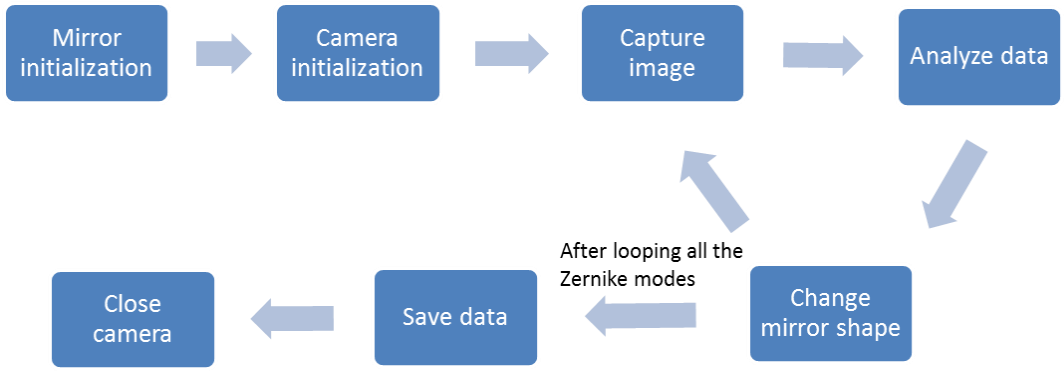


Figure 3. 6: Flow chart of the measurement process.

First, the amplitude of different Zernike modes was changed in steps. The DM controller was programmed with the ANSI Z.80.28-2004 standard Zernike modes, using single-index notation and contained 21 modes totally. The first set of the Zernike modes sent to the DM had the Zernike coefficients from -0.5 μm *rms* to 0.5 μm *rms* (all the amplitudes mentioned below in this chapter are in μm *rms* unit), at a step size of 0.1. In order to characterize the shape efficiently, only one Zernike mode was set while other modes were zero. This set of measurements were intended to characterize the mirror change over a small range. Thereafter, another set of Zernike modes which has a range of -2 to 2 at step size of 1 was used.

3.3.2 Data Record and Analysis

The first processing step is to extract the phase from the interferogram. The 2D Fast Fourier Transform (FFT) was used to recover phase in our experiment [56, 64, 65]. As the mirror was set to have tip/tilt effect, which is also a good way to check the fringes at first, the intensity of the interferogram could be represented as:

3.3 Results and analysis

$$I = \left|Ae^{i\Phi} + Be^{i\varphi}\right|^2 = A^2 + B^2 + ABe^{i(\Phi-\varphi)} + ABe^{-i(\Phi+\varphi)} \quad (3.7)$$

where $Ae^{i\Phi}$ is the complex field of the light reflected by the DM, while $Be^{i\varphi}$ is the complex field of the light reflected by the reference mirror. If the Fourier transform is applied to Eq. (3.7), one will get three terms in the frequency domain, 0 order, +1 order, -1 order. The +1 order can be separated by applying a mask and shift it to the centre to demodulate the spatial frequency. The wrapped phase can be obtained from the inverse Fourier transform. As phase is periodic, the phase value after calculation is always in the range (-π, +π]. The unwrapped phase was recovered from this by using a phase unwrapping algorithm [66].

When doing the mask selection, one need make sure that the area that the mask covered should approximately the same as the aperture. The DM manufacturer defined that the circle inscribed within the actuator pattern was the aperture that used to generate the pre-calibrated Zernike coefficients, so Figure 3.7 shows the mask applied on the first interferogram.

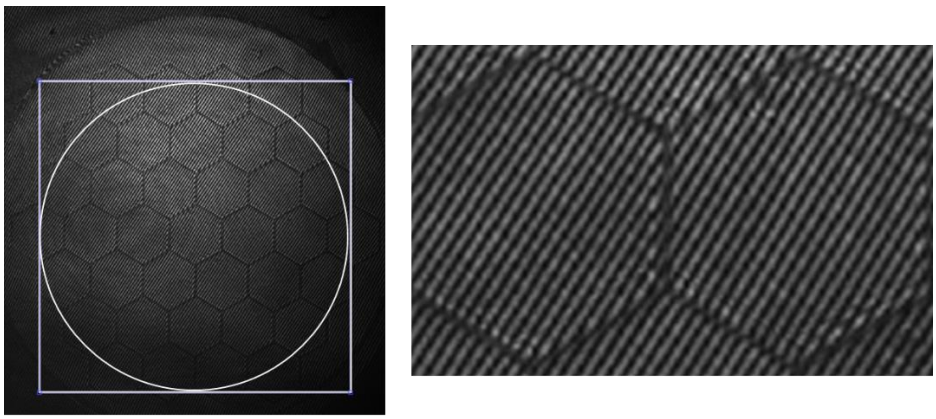


Figure 3. 7: (a) Initial interferogram with the applied mask (b) Zoomed in fringes.

Next, the program took only the pattern in the inscribed circle as the aperture for analysis. The included part is shown in Figure 3.8.

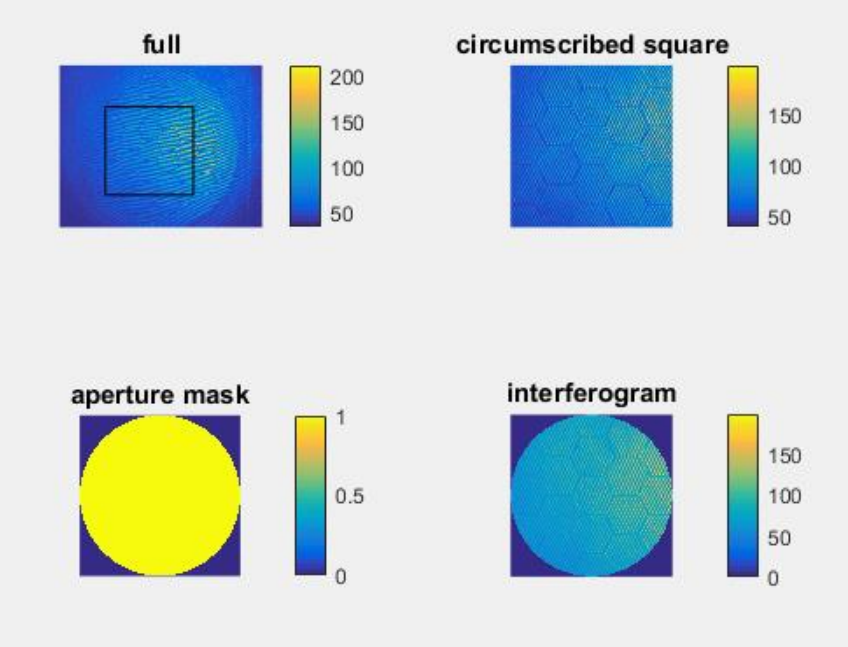


Figure 3. 8: Effective analysis area and interferogram after applying the aperture mask.

Then the Fourier transform of the image was calculated and showed its graph in frequency domain. Three bright dots are clearly shown in the Figure 3.9. Figure 3.10 shows a series of the images that illustrate the process from the interferogram to phase (fringes, Fourier transform, apply mask, shift to origin, inverse Fourier transform, phase).

The image used for mask selection was when the DM at the mirror-release state at which there would be no voltage applied. It is also found that the DM after the mirror release command was not in a flat state. Therefore, in Figure 3.10 can see the individual hexagonal mirror segments, which is the result of the displacement between each segments position. The phase shown here is the wrapped phase, which means that the phase values are all in the same range of - π to π radians. In order to get the unwrapped real phase, an unwrapping algorithm [66] was used that in effect adds an integer multiple of 2π to the corresponding wrapped value at different points in the retrieved function. The wrapped and unwrapped phase of the interferogram with tilt are shown in Figure 3.11.

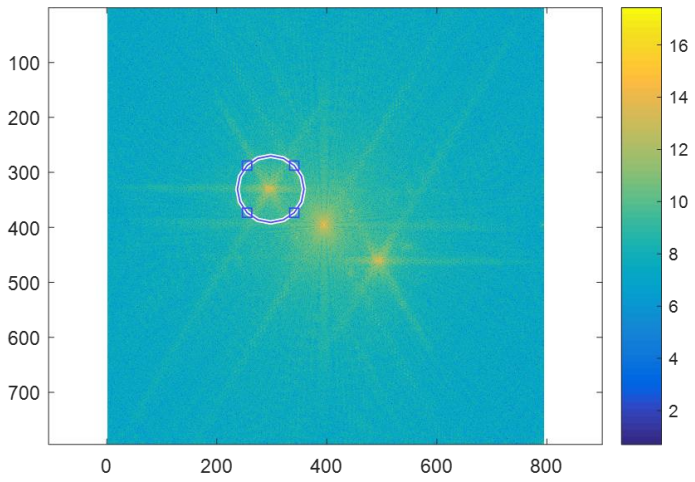


Figure 3. 9: Fourier transform and mask of initial interferogram, three bright dots represent three frequency orders existing in the fringes.

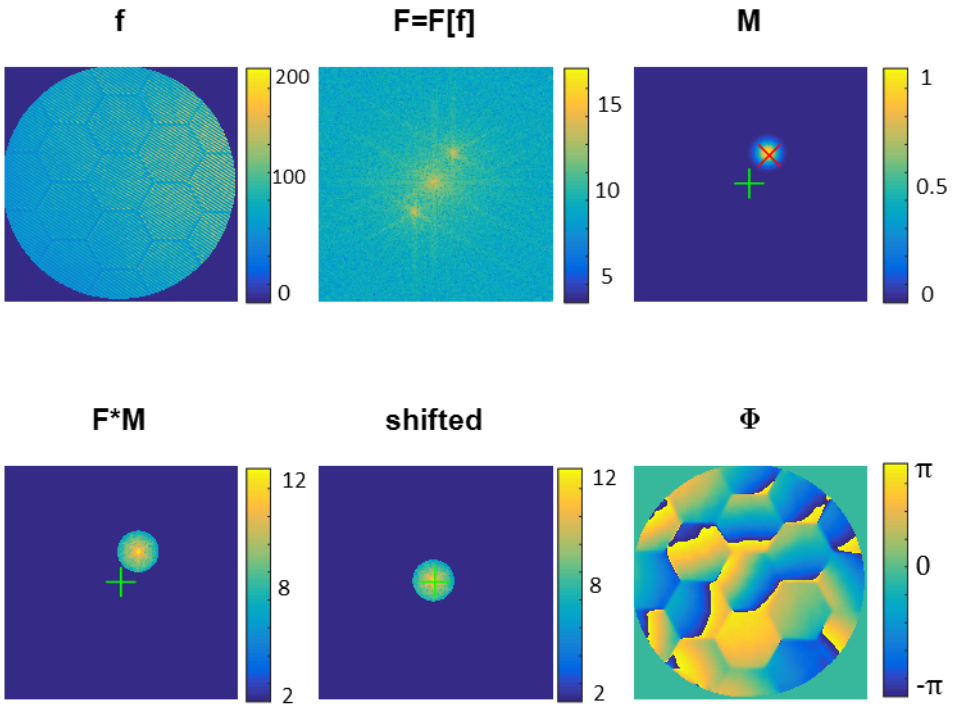


Figure 3. 10: Analysis process from fringes to phase. Interferogram (f), Fourier transform (F = F[f]), apply uniform mask (M), mask multiplication (F*M), shift to origin (shifted), phase (ϕ)

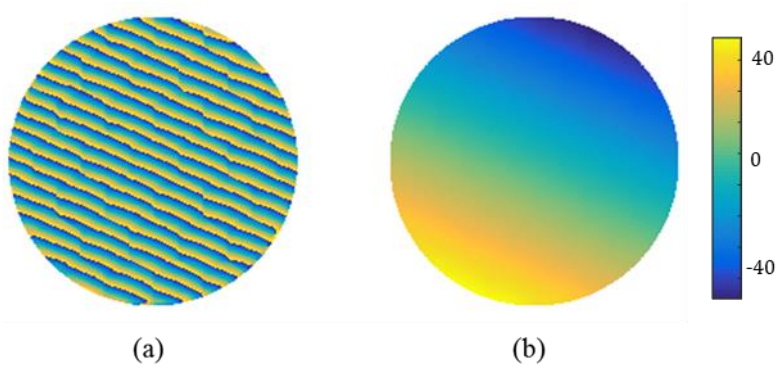


Figure 3. 11: (a) Wrapped phase of the interferogram with tilt and (b) Calculated unwrapped phase

In order to compare the Zernike coefficient and amplitude sent to the DM to those measured from the interferogram, it is plotted, as shown in Figure 3.12, the blue line, the measured coefficients and the red line, the coefficients set. As there is initial piston, tip and tilt (PTT) in the reference mirror, mode 1–3 that are piston, tip and tilt always have non-zero value. Basically, the tip and tilt value will remain the same in all measurements if DM is not in any PTT mode. In the later analysis the initial PPT were removed. Figure 3.12 shows the initial PTT value. Since only one set of the initial value is not sufficient to obtain the accurate initial PTT, the mean value of all sets measured data is obtained to evaluate this effect. Since piston represents the DM movement along the optical axis, this value is changeable from time to time and has no impact on the surface shape. Hence, the piston value during the accuracy analysis will be ignored in the experiment. In order to increase the accuracy and compensate the Zernike fitting error, 45 modes were used in the program to fit the fringes although only 20 modes can be set in the control code for this DM. Although high order Zernike modes are not common in aberration in microscopes, they are dominate in astronomy aberration.

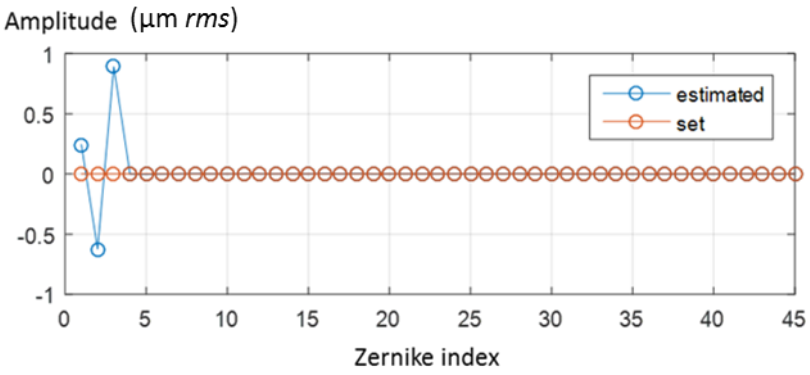


Figure 3. 12: PTT value of initial interferogram. Blue line: estimated amplitude from the interferogram; red line: set amplitude sent to the DM.

Figure 3.13 (a) shows an example of setting the DM to a 0.5 µm *rms* tilt (red line) and the blue line is the amplitude of each Zernike coefficient that estimated based on image analysis. The corresponding phase is shown is Figure 3.13 (b). Although the estimated coefficient contains the initial tilt component, when changing the tilt amplitude, the estimated amplitude will change to the same extent e.g. when set tilt changed 0.1, the measured tilt changes 0.1 correspondingly, which proves that the program works correctly.

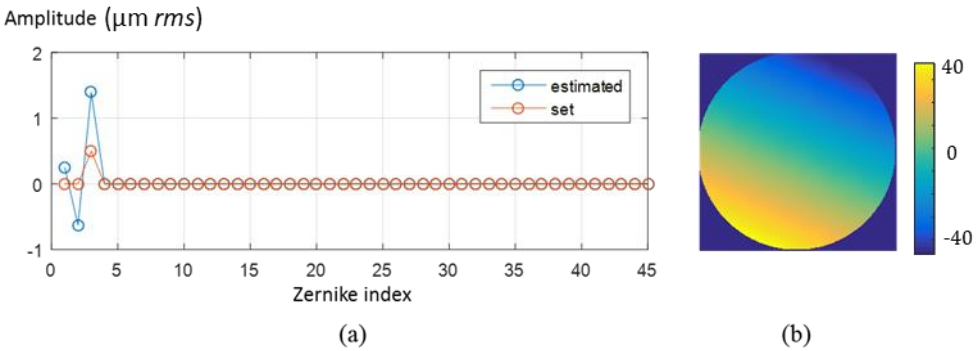


Figure 3. 13: (a) Comparison of the amplitude of different Zernike modes of set and estimated when the DM is set to 0.5 µm *rms* tilt (b) Calculated unwrapped phase.

3.4 Error analysis

Although the DM controller used a different single index normalization, it is transferred to Noll's index for standardization shown in Table 3.1. From now on, all the index discussed below is based on Noll's index.

Table 3. 1 Noll's index numbering

j = index	n = order	m = frequency	$Z_n^m(\rho,\theta)$
1	0	0	1
2	1	1	2 ρ cos θ
3	1	-1	2 ρ sin θ
4	2	0	$\sqrt{3}$ (2ρ^2-1)
5	2	-2	$\sqrt{6}$ ρ^2 sin 2θ
6	2	2	$\sqrt{6}$ ρ^2 cos 2θ
7	3	-1	$\sqrt{8}$ (3ρ^3-2ρ) sin θ
8	3	-1	$\sqrt{8}$ (3ρ^3-2ρ) cos θ
9	3	-3	$\sqrt{8}$ ρ^3 sin 3θ
10	3	3	$\sqrt{8}$ ρ^3 cos 3θ
11	4	0	$\sqrt{5}$ (6ρ^4-6ρ^2+1)
12	4	2	$\sqrt{10}$ (4ρ^4-3ρ^2) cos 2θ
13	4	-2	$\sqrt{10}$ (4ρ^4-3ρ^2) sin 2θ
14	4	4	$\sqrt{10}$ ρ^4 cos 4θ
15	4	-4	$\sqrt{12}$ ρ^5 sin 5θ$\sqrt{10}$ ρ^4 sin
16	5	-1	$\sqrt{12}$ (10ρ^5-12ρ^3+3ρ) sin θ
17	5	1	$\sqrt{12}$ (10ρ^5-12ρ^3+3ρ)
18	5	-3	$\sqrt{12}$ (5ρ^5-4ρ^3) sin 3θ
19	5	3	$\sqrt{12}$ (5ρ^5-4ρ^3) cos 3θ
20	5	-5	$\sqrt{12}$ ρ^5 sin 5θ
21	5	5	$\sqrt{12}$ ρ^5 cos 5θ

Mode 1–20 in single index corresponds to mode 2–21 in Noll's index. All the curves of all the amplitude of the measured Zernike coefficients comparing to the set ones are plotted. Besides the difference between the desired and measured amplitude of the specified Zernike mode, the

sum of the amplitude of the other modes is also counted. The error calculation formula is shown in Eq. (3.8).

$$\varepsilon = \sqrt{(a_s - a_m)^2 + \sum_{k \neq m} a_k^2} \tag{3.8}$$

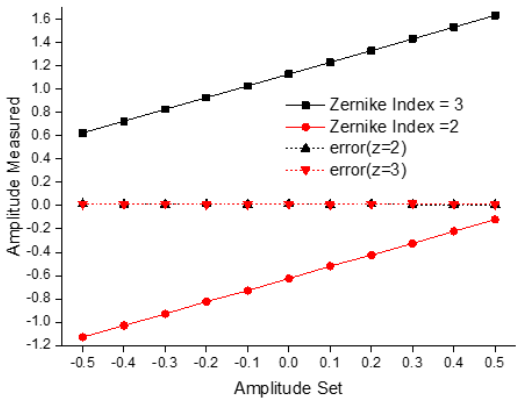
where a_s is the amplitude of the specific Zernike mode set; a_m is the amplitude of that Zernike mode measured; a_k is the amplitude of other Zernike modes measured except for piston, and the initial tilt and tip.

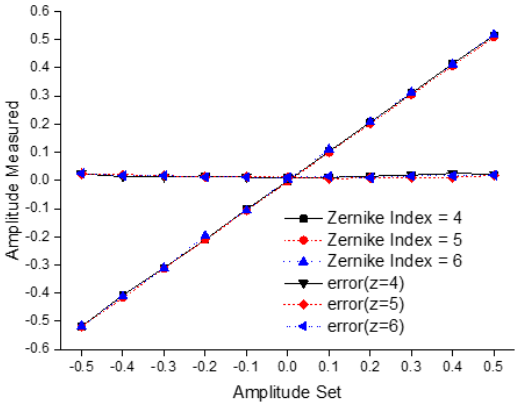
3.4.1 Small amplitude and step size

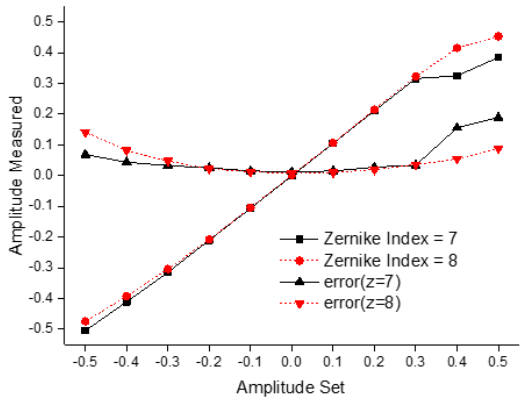
The errors and the amplitude measured are plotted at the same scale in Figure 3.14 with the amplitude sent from -0.5 to 0.5 with step size of 0.1.

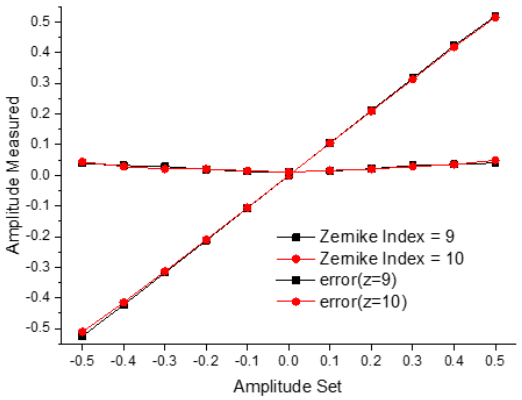
In order to visualize the amplitude of the Zernike coefficient at same scale, the initial tip/tilt effect was removed. Another part of the error is the processing error, which is caused by the phase unwrapping process. When using the unwrapping algorithm, it may have larger unwrapping error for higher Zernike order. Of course, with the segmented mirror one can expect phase jumps at the edges of the hexagonal segments. The sharp edges within the segments other than the border of the segments itself, it may be the evidence that the errors are because of the unwrapping, not a mirror issue.

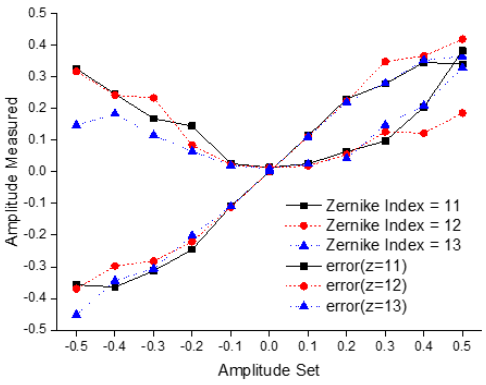
3.4 Error analysis

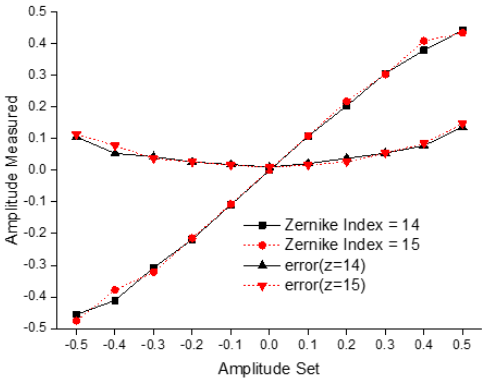


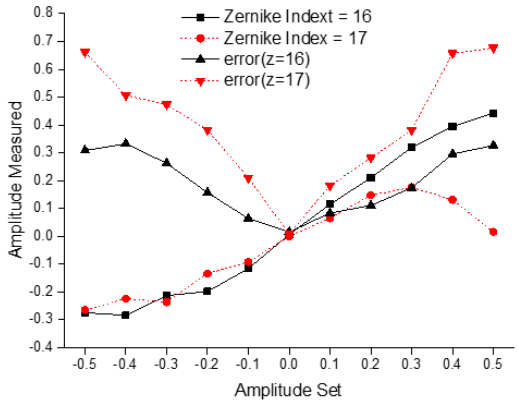


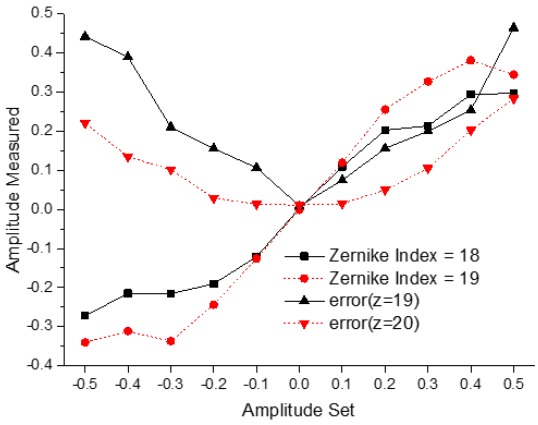












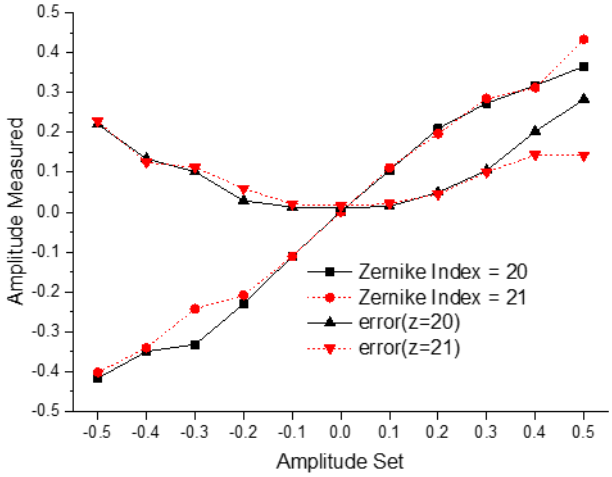


Figure 3. 14: Comparison of the measured amplitude and set amplitude for 2−21 Zernike mode (Noll's index) and corresponding errors, which are calculated as the sum of *rms* amplitude of other Zernike modes and difference between the set amplitude and measured amplitude.

Tip & Tilt

Mode 2 and 3 are tip and tilt so in Figure 3.13 (a) the measured amplitude is not consistent with the amplitude set. However, the change within the range is nearly linear and the gradient is around 0.96 approximately to 1.

Defocus & Primary Astigmatism

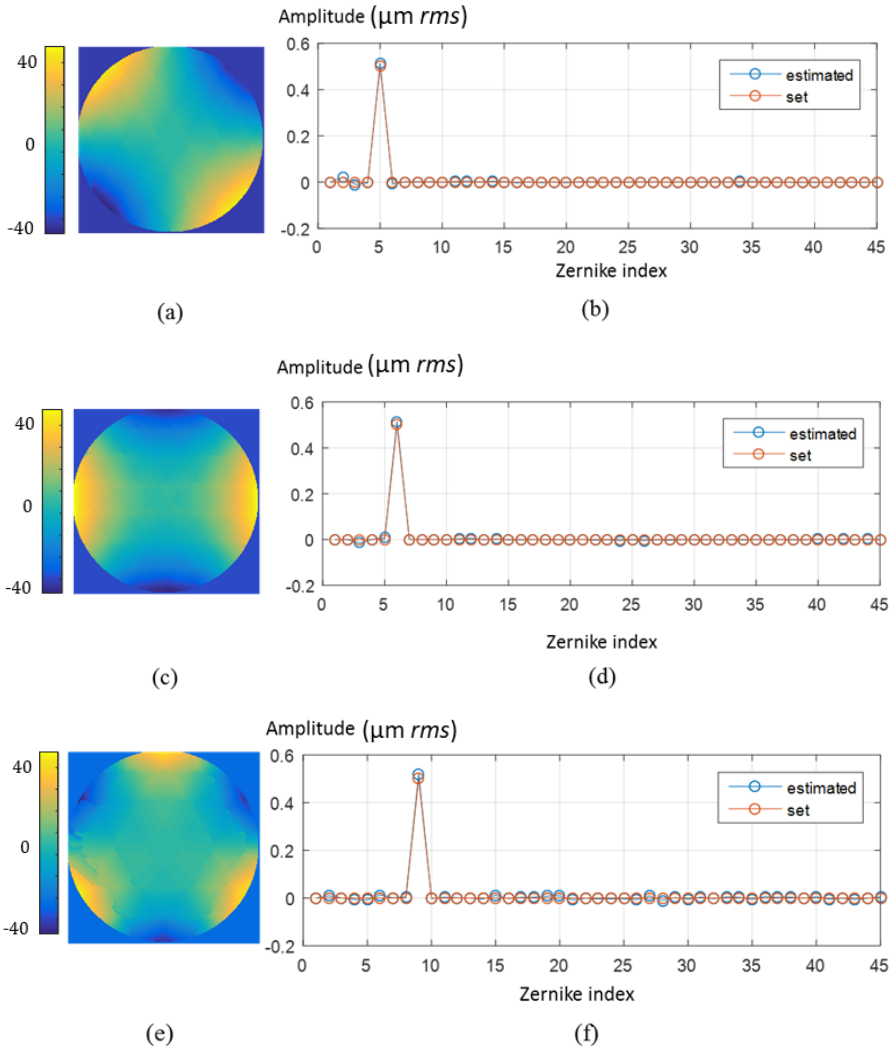
Mode 4, 5, and 6 have similar changing trend and the measured amplitude at each point matches closely the set amplitude. These results show that the mirror can generate the Zernike shape from mode 2 to 6 in the range of -0.5 to 0.5 with error below 5%, which is negligible.

Primary Trefoil

A good match is also found for modes 9 and 10. Errors are higher when the amplitude is 0.5 but still remain small with gradient error within 5% when amplitude is below 0.3. To know where the larger error comes from, the comparison of the set Zernike coefficient and the

measured Zernike coefficient at mode 4, 5 and 6 with amplitude of 0.5 was displayed, which is shown in Figure 3.15.

From the coefficient comparison figure, it is seen that the enlarged error is not only because of the difference between the estimated and set amplitude of the specific coefficient, more coefficients have non-zero value for Mode 9 and 10. From the unwrapped phase figure, it is clearly that mode 5 and 6 have smooth phase graph while in the mode 9 and 10, some edges of the mirror segments could be seen. That may be the reason why the measured amplitude is slightly higher than the expected one. Despite that, modes 9 and 10 are still in 5% gradient deviation because they have good linearity with gradient ~1.



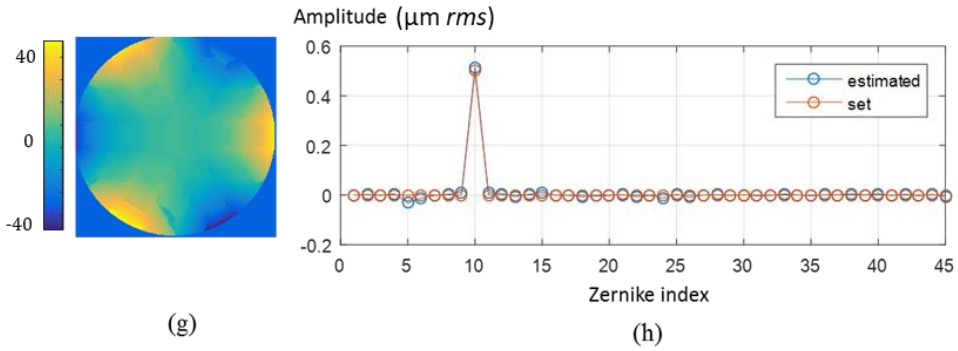


Figure 3. 15: Unwrapped phase and comparison of estimated and set Zernike coefficient (a) Mode 5 phase (b) Mode 5 coefficient comparison (c) Mode 6 phase (d) Mode 6 coefficient comparison (e) Mode 9 phase (d) Mode 9 coefficient comparison (g) Mode 10 phase (h) Mode 10 coefficient comparison.

Quadrafoil

The pair of modes 14 and 15 have consistent trend and errors. Errors increase when the amplitude is above 0.4. From the phase and coefficient graph, it is found that the phase graph has more sharp edges and therefore, many other Zernike modes have non-zero value. As the mirror is segment based, when it is commanded to generate a higher amplitude, there will be significant gap between segment edges.

Pentafoil

As the azimuthal order increases, more rapid spatial changes are required in the mirror shape. Therefore, when amplitude goes higher, it becomes more difficult for the DM to generate modes with high amplitude. Figure 3.16 shows the phase and coefficient comparison of mode 20 and 21 at amplitude of 0.5 and their desired mirror shape.

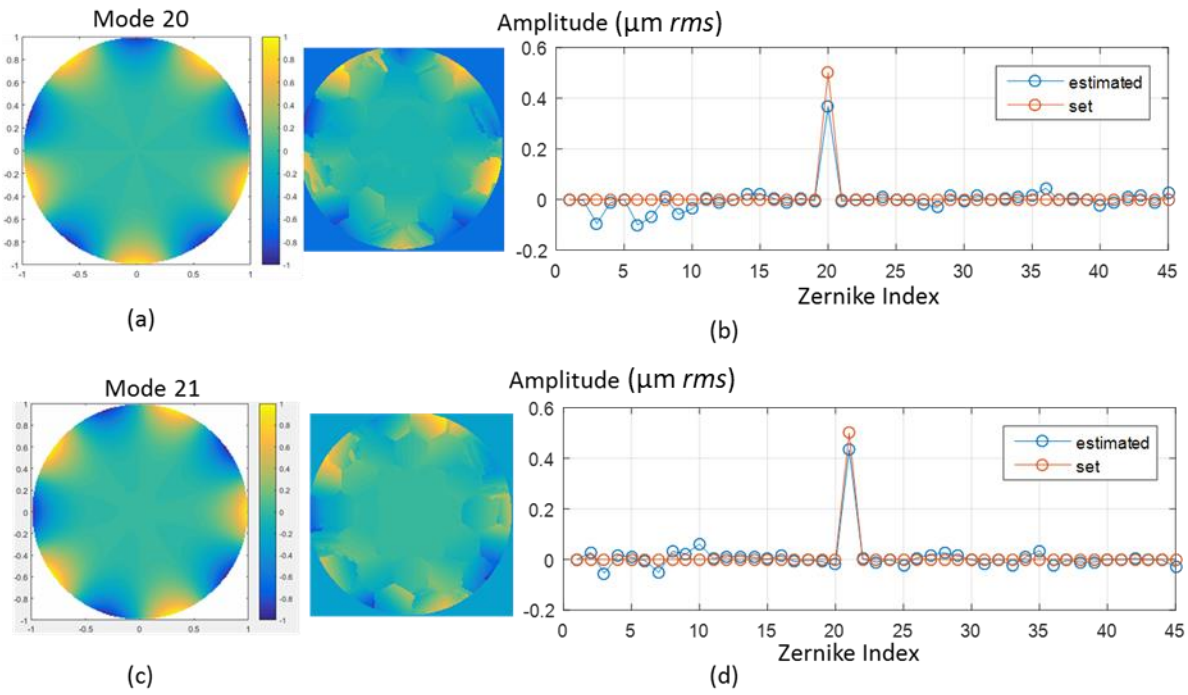


Figure 3. 16: Simulation (a) Ideal phase profile for mode 20 (b) measured unwrapped phase and coefficient comparison of mode 20 with an amplitude of 0.5 (c) Ideal phase graph for mode 21 (d) measured unwrapped phase and coefficient comparison of mode 20 with an amplitude of 0.5.

Thereafter, the modes 7&8, 11, 12&13, 16&17, 18&19, which have larger errors were analysed.

Primary Coma

Although modes 7 and 8 still have good linearity with gradient ~1, the error curve is not symmetrical with respect to the origin nor similar to the previous modes analysed. Figure 3.17 shows the measured phase of mode 7 and 8 at different amplitudes. More edges of the segments can be seen. These two modes both require a rapid spatial change of phase gradient that is not well represented by the segmented mirror, which is reason why the linearity is not as good as for mode 9 and 10. In addition to that, mode 7 clearly has worse phase structure than mode 8 at positive amplitude. The only difference between mode 7 and mode 8 is that mode 7 requires the upper and lower segments to generate the sudden change while the mode 8 requires the left and right segments to do that. However, it is noticed that, the error at the upper and lower

segments are due to a processing error, rather than the mirror itself since the error exits within the segment. However, it seems like the unwrapping errors are always in the upper and lower area, it is possible that because the segments' arrangement cause the upper/lower segments arrangement to differ from the left/right ones. Like the mirror arrangements shown in Figure 3.4, the relative orientation of the hexagonal segments is different between the upper/lower ones and the left/right ones. That means the discontinuity is also different in the two regions. When trying to decrease the mask size, the unwrapping error indeed decreased, which can be seen in Figure 3.18. Sometimes the unwrapping errors can be resolved by using a different mask radius, but sometimes it is a problem irrespective of the mask properties.

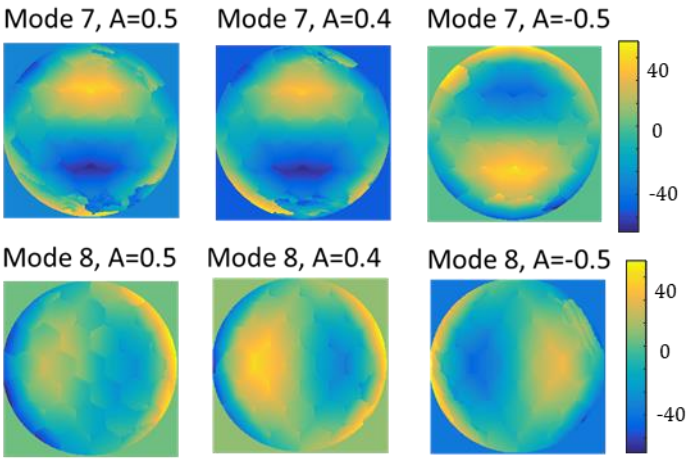


Figure 3. 17: Measured phase profile of mode 7 and 8 with different amplitudes.

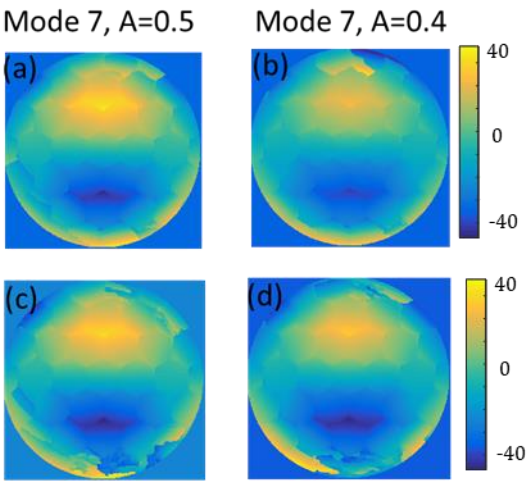


Figure 3. 18: (a) Mode 7 phase profile with an amplitude of 0.5 with smaller mask (b) Mode 7 phase profile with an amplitude of 0.4 with smaller mask (c) Mode 7 phase profile with an amplitude of 0.5 with normal mask (d) Mode 7 phase profile with an amplitude of 0.4 with the normal mask.

Secondary Coma

Apparently, modes 16 and 17 have a very different trend and are not symmetrical about the origin. As the phase of these two modes is not ideal and it is not easy to tell its original shape, a program is used to plot the desired phase graph for these two modes that are shown in Figure 3.19. A rapid change in phase gradients near the edge, that might not be reproduced by the segments can be observed.

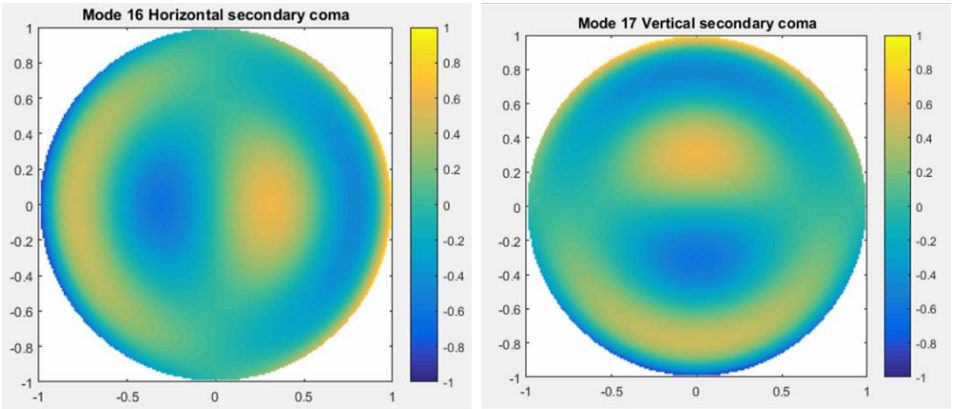


Figure 3. 19: Maximal ideal phase graph of (a) Mode 16 (b) Mode 17.

3.4 Error analysis

It is clear that mode 16 required rapid change in phase gradient on the left and right segments and mode 17 on the upper and lower segments. The measured decreasing amplitude from 0.3 once again show that; the upper and lower segments have lower capability and flexibility to generate the rapid shape change.

The cross-section analysis is done on mode 17 to see the ideal and real wave shape, which are shown in Figure 3.20. From Figure 3.20 (c) it can be seen that the function contains rapidly changing gradients across the diagonal. These changes need to be produced by only six segments in the DM and that is why there are dramatic difference in the real phase which is shown in Figure 3.20 (b) while Figure 3.20 (a) has more variation due to the unwrapping process error. Some of these steps represent the gap between two segments. These data illustrate that when the Zernike order increases and becomes more complicated, the segmented DM will gradually fail to produce suitable shapes.

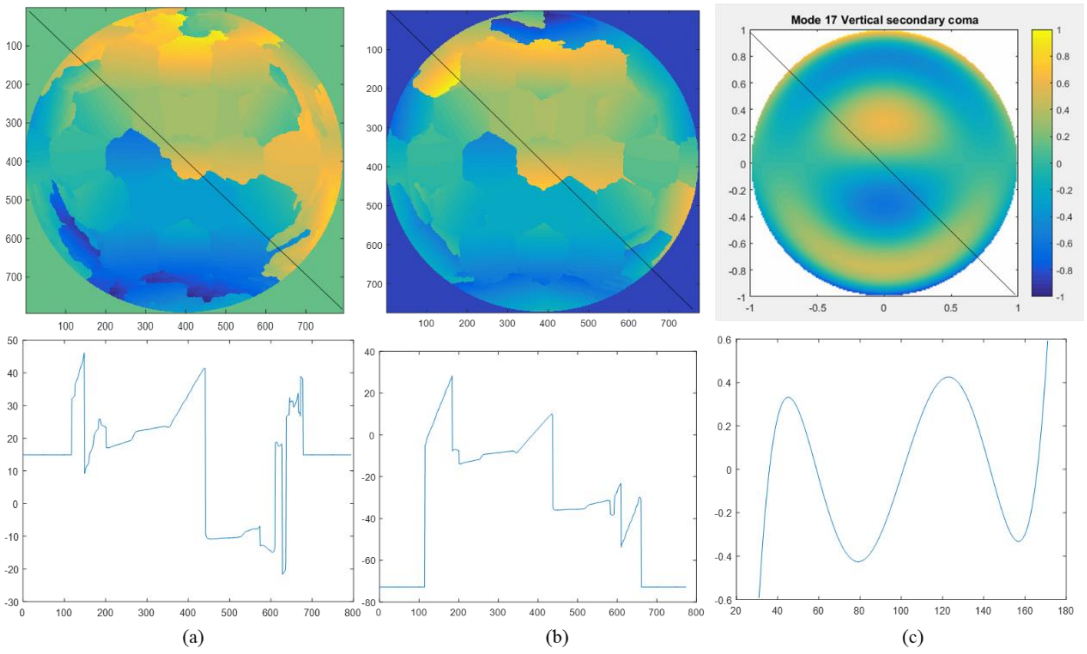
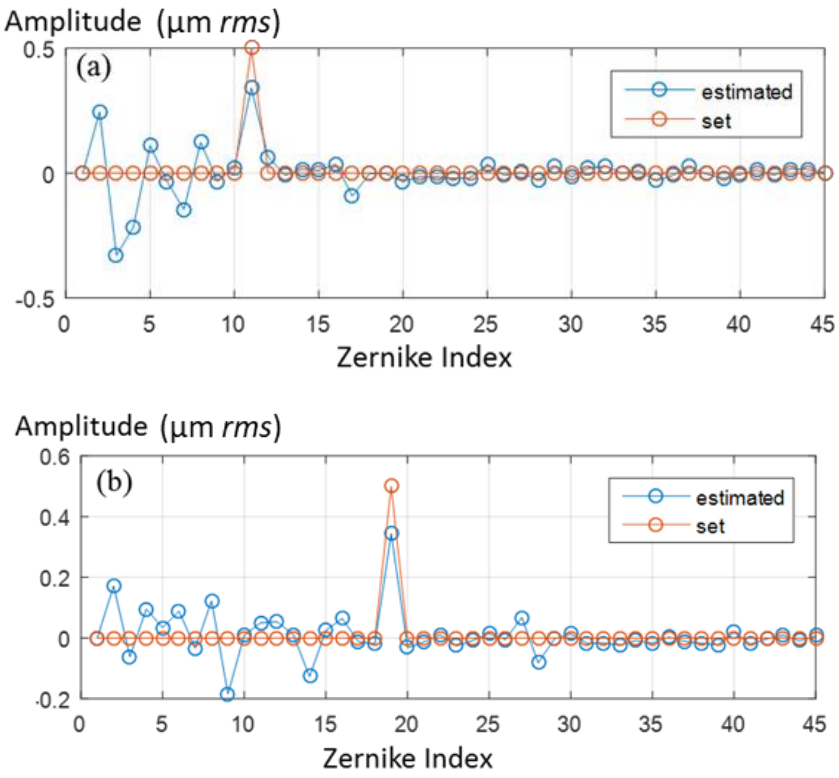


Figure 3. 20: (a) Cross-section phase analysis (b) Measured phase of mode 17 with an amplitude of 0.4 with normal mask (c) Measured phase of mode 17 with an amplitude of 0.4 with smaller mask (c) Ideal phase; the *x* axis is the pixel number along the diagonal and *y* axis is the relative amplitude.

Primary Spherical, Secondary Astigmatism & Secondary Trefoil

Modes 11, 12&13 and 18&19 all have very large errors and modes 18&19 are not even strictly monotonically increasing, especially seen for mode 19. Both of these pairs are nearly symmetrical about the origin. However, the measured amplitude is far away from the desired one. If the amplitude of other coefficients are extracted, it is find the value of other modes' components are very high. Figure 3.21 shows those with the high value of other components.



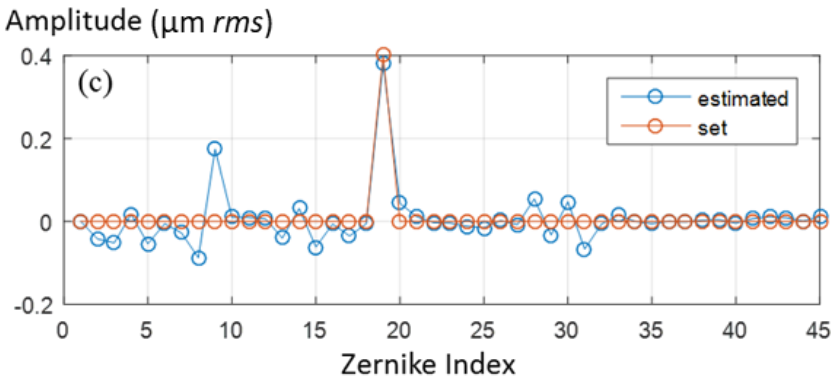


Figure 3. 21: Comparison between the set (red line) and measured (blue line) Zernike coefficients for different modes and amplitudes (a) Mode 11 at amplitude of 0.5 (b) Mode 19 with amplitude of 0.5 (c) Mode 19 with amplitude of 0.4

Some cross talk are observed between modes, in that when the DM was used to produce certain modes, modes of a similar form are produced. In Figure 3.21 (c), for example, there is an obvious non-zero component at mode 9, with an amplitude comparable to the mode 19. The equations for mode 19 and mode 9 are as follows:

$$Z_{19} = \sqrt{12}(5\rho^5 - 4\rho^3)\sin 3\theta \tag{3.9}$$

$$Z_9 = \sqrt{8}\,\rho^3 \sin 3\theta \tag{3.10}$$

Due to the ρ^3 dependence, it is understandable that the DM reproduction of mode 19 can include a component of mode 9.

Another key property is the rate of change of phase gradient or equivalently the second derivative of the phase with respect to radial variable. Table 3.2 list the first and second derivative of the each Zernike mode, as well as the maximum value of the second derivative, which is when $\rho = 1$. From the first derivative of ρ of Z, the phase change rate is represented along one direction. For example, in Figure 3.18, it can be seen that when $\theta = 0$, the phase does not change on the transverse direction. However, when $\theta = 90°$, the phase changes most rapidly.

3.4 Error analysis

According to the first derivative to ρ, the fastest phase change is able to be determined. From the last column, it can be seen that the higher values of the second derivate correlates well with the higher errors in Figure 3.15.

Table 3. 2 First and second derivative of the each Zernike mode

Index	$Z_n^m(\rho,\theta)$	$\frac{\partial Z}{\partial \rho}$	$\frac{\partial^2 Z}{\partial^2 \rho}$	$\frac{\partial^2 Z}{\partial^2 \rho}_{\rho=1}$
2	$2\rho\cos\theta$	$2\cos\theta$	0	0
3	$2\rho\sin\theta$	$2\sin\theta$	0	0
4	$\sqrt{3}(2\rho^2-1)$	$4\sqrt{3}\rho$	$4\sqrt{3}$	$4\sqrt{3}$
5	$\sqrt{6}\rho^2\sin 2\theta$	$2\sqrt{6}\rho\sin 2\theta$	$2\sqrt{6}\sin 2\theta$	$2\sqrt{6}\sin 2\theta$
6	$\sqrt{6}\rho^2\cos 2\theta$	$2\sqrt{6}\rho\cos 2\theta$	$2\sqrt{6}\cos 2\theta$	$2\sqrt{6}\cos 2\theta$
7	$\sqrt{8}(3\rho^3-2\rho)\sin\theta$	$\sqrt{8}(9\rho^2-2)\sin\theta$	$18\sqrt{8}\rho\sin\theta$	$18\sqrt{8}\sin\theta$
8	$\sqrt{8}(3\rho^3-2\rho)\cos\theta$	$\sqrt{8}(9\rho^2-2)\cos\theta$	$18\sqrt{8}\rho\cos\theta$	$18\sqrt{8}\cos\theta$
9	$\sqrt{8}\rho^3\sin 3\theta$	$3\sqrt{8}\rho^2\sin 3\theta$	$24\sqrt{8}\rho\sin 3\theta$	$24\sqrt{8}\sin 3\theta$
10	$\sqrt{8}\rho^3\cos 3\theta$	$3\sqrt{8}\rho^2\cos 3\theta$	$24\sqrt{8}\rho\cos 3\theta$	$24\sqrt{8}\cos 3\theta$
11	$\sqrt{5}(6\rho^4-6\rho^2+1)$	$\sqrt{5}(24\rho^3-12\rho)$	$12\sqrt{5}(6\rho^2-1)$	$60\sqrt{5}$
12	$\sqrt{10}(4\rho^4-3\rho^2)\cos 2\theta$	$\sqrt{10}(16\rho^3-6\rho)\cos 2\theta$	$6\sqrt{10}(8\rho^2-1)\cos 2\theta$	$42\sqrt{10}\cos 2\theta$
13	$\sqrt{10}(4\rho^4-3\rho^2)\sin 2\theta$	$\sqrt{10}(16\rho^3-6\rho)\sin 2\theta$	$6\sqrt{10}(8\rho^2-1)\sin 2\theta$	$42\sqrt{10}\sin 2\theta$
14	$\sqrt{10}\rho^4\cos 4\theta$	$4\sqrt{10}\rho^3\cos 4\theta$	$12\sqrt{10}\rho^2$	$12\sqrt{10}$
15	$\sqrt{10}\rho^4\sin 4\theta$	$4\sqrt{10}\rho^3\sin 4\theta$	$12\sqrt{10}\rho^2$	$12\sqrt{10}$
16	$\sqrt{12}(10\rho^5-12\rho^3+3\rho)\cos\theta$	$\sqrt{12}(50\rho^4-48\rho^2+3)\cos\theta$	$8\sqrt{12}(25\rho^3-12\rho)\cos\theta$	$104\sqrt{12}\cos\theta$
17	$\sqrt{12}(10\rho^5-12\rho^3+3\rho)\sin\theta$	$\sqrt{12}(50\rho^4-48\rho^2+3)\sin\theta$	$8\sqrt{12}(25\rho^3-12\rho)\sin\theta$	$104\sqrt{12}\sin\theta$
18	$\sqrt{12}(5\rho^5-4\rho^3)\cos 3\theta$	$\sqrt{12}(25\rho^4-12\rho^2)\cos 3\theta$	$4\sqrt{12}(25\rho^3-6\rho)\cos 3\theta$	$76\sqrt{12}\cos 3\theta$
19	$\sqrt{12}(5\rho^5-4\rho^3)\sin 3\theta$	$\sqrt{12}(25\rho^4-12\rho^2)\sin 3\theta$	$4\sqrt{12}(25\rho^3-6\rho)\sin 3\theta$	$76\sqrt{12}\sin 3\theta$
20	$\sqrt{12}\rho^5\cos 5\theta$	$5\sqrt{12}\rho^4\cos 5\theta$	$20\sqrt{12}\rho^3\cos 5\theta$	$20\sqrt{12}\cos 5\theta$
21	$\sqrt{12}\rho^5\sin 5\theta$	$5\sqrt{12}\rho^4\sin 5\theta$	$20\sqrt{12}\rho^3\sin 5\theta$	$20\sqrt{12}\sin 5\theta$

Figure 3.22 shows the average sum of the error from amplitude of -0.5 to 0.5 for different modes. Errors increase as the mode order increases but it is not monotonic. The errors become larger for mode 11 and 16 but then decrease for the modes 14 & 15 and 20 & 21 that have smaller second derivatives. Since the errors after mode 16 are large, it might be possible to generate more accurate shape with lower amplitudes. For the first 10 modes, they have good linearity and match with the ideal Zernike shape in all of the range. To know to which extent degrade, larger amplitudes were used.

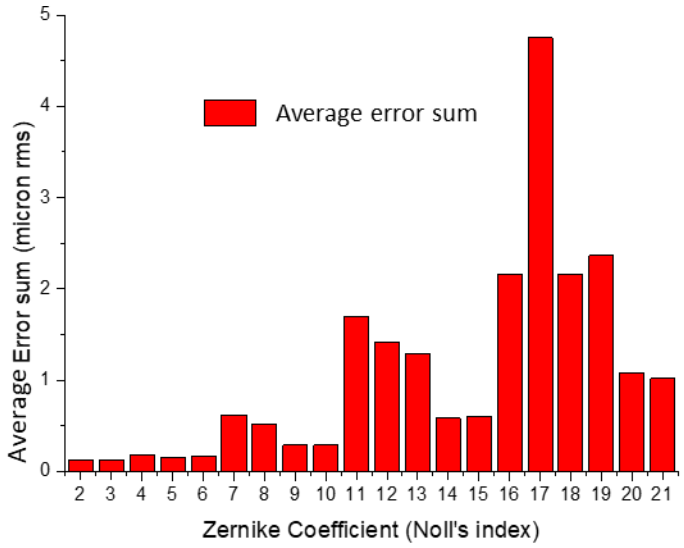


Figure 3. 22: Average error sum ε from amplitude of -0.5 to 0.5 at different modes.

3.4.2 Large amplitude and step size

Next, a larger range of amplitudes from -2 to 2 was sent to the mirror, with the step size of 1. Figure 3.23 shows the measured amplitude for some Zernike modes and corresponding errors.

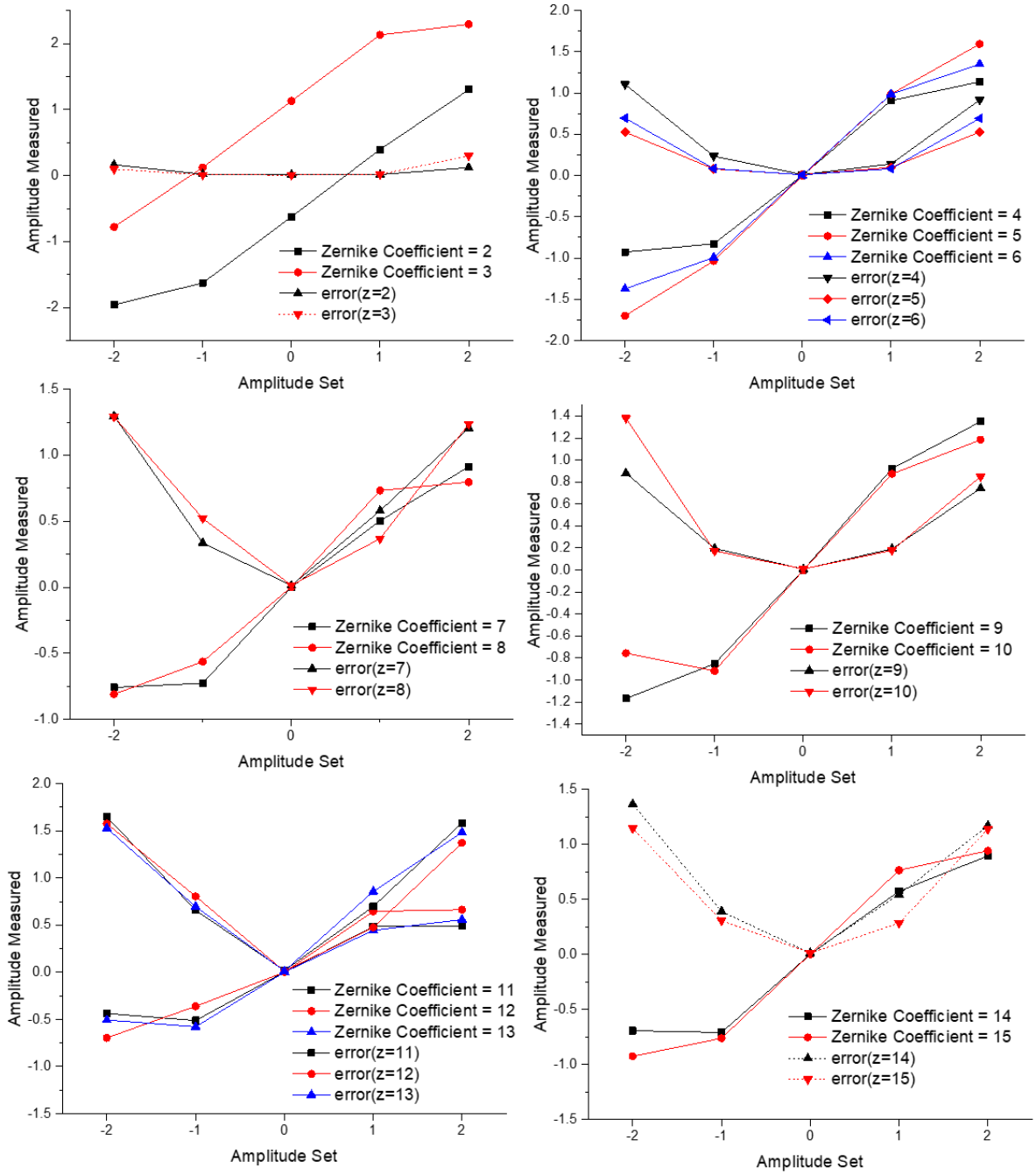


Figure 3. 23: The measured amplitude for Zernike modes 2–15 (Noll's index) and corresponding errors, with amplitude from -2 to 2 and step size of 1.

As the amplitude and step size increase, the linearity begins to disappear. For mode 2–6 and mode 9&10, the linearity remains for amplitudes in the range -1 to 1. However, for other modes, the accuracy at an amplitude of 1 decreases significantly and the errors are high. In this case,

it may not be adequate to generate amplitudes larger than 1. Besides, the lower modes have good symmetry with respect to the origin and two curves in each pair has similar trend. While for mode 7 & 8 and higher modes, their symmetry is not seen and two curves between each pair are not exactly following the same trend.

3.5 Summary

The performance for all of the individual Zernike modes on the DM using both small and large amplitudes and step sizes have been analysed. When the step size and amplitude increase, the accuracy of producing the Zernike mode decreases because they put a higher demands on the DM segment with regard to continuity and fast spatial response. Corresponding errors may stem from the mask mismatch, mirror saturation, segment arrangement orientation and anisotropy, random DM zero-state position, etc.

For modes 2−6 and modes 9 & 10, it is possible to set the amplitude to ± 1. Within this range, the gradient nearly equals 1 and calculated the gradient of the curves in each pair follow the same trend. They are always symmetric with respect to the origin.

For modes 7 & 8, the suitable range is not symmetrical any more. The safe region to produce an accurate shape will be from -0.5 to 0.3. In this region, the DM is able to generate accurate matched Zernike shapes. Other higher order modes are also possible to have a relative larger active range like for mode 14 & 15, 20 & 21, because they have smaller second derivatives. For 14 & 15, a suitable range may from -0.4 to 0.4 while for 20 & 21, it should be decreased to -0.2 to 0.3.

For mode 11−13, the accurate range should fall in the range of -0.2 to 0.2, while mode 16&17 and 18&19, better to keep it in the range of -0.1 to 0.1. Mode 17 is a problematic mode with very large error even at the amplitude of 0.1.

3.5 Summary

In this chapter, the limitation of a correction device on AO phase correction for a segmented DM was investigated. In summary, this DM is able to generate accurate lower-order Zernike modes at low amplitude. For higher-order Zernike modes, it becomes harder to produce the rapid spatial change between the segments. Besides, probably due to some manufacturing reason, not all of the segments have the same capability and flexibility, which also limits the precision.

Chapter 4 Calibration of SLM for Phase and Retardance Modulation

As other correction devices, the liquid crystal spatial light modulators (SLMs) have widespread use in many optical applications. Most applications draw upon the SLM's capabilities for phase modulation; these include quantum optics [67], beam shaping [68], direct laser writing in silicon photonic circuits [69], and aberration correction in various microscopes [70-72]. The SLM is also a fundamental element in some super-resolution microscopy techniques such as structured illumination microscopy (SIM) [73] and stimulated emission depletion (STED) microscopy [8, 74].

The SLM is based upon a liquid crystal array, in which the orientation of liquid crystal molecules can be modified using optical or electrical means. The liquid crystals in an SLM can be regarded as an array of variable retarders with fixed fast axis. Therefore, an SLM can also be used to manipulate beam polarization. This opens a window for more applications such as vortex beam generation [75-80], Pancharatnam-Berry device fabrication [81], color imaging [82], and quantum logic [83].

For all of these applications, accurate control of the SLM is required. The devices are not perfectly flat or uniform after manufacture, so one should expect spatial variations in their properties. Although correction files might be provided from manufacturing, the non-linear response between the drive voltage and the phase modulated by the SLM can be changed by

exogenous factors, such as temperature and aging. Therefore, the SLM needs to be fully calibrated before use. Previous research has focused on compensating phase errors and non-linearity [84-87] by using different set-ups such as ptychography [88], optical tweezers [89], self-generated grating [90], as well as various interferometers [91] like Mach-Zehnder [92-95], phase-shifting [96-98] and Twyman-Green [99, 100]. However, the phase calibration alone is not sufficient to enable accurate polarization control, as outlined later in this chapter.

The process of calibrating an SLM consists of identifying the drive voltage that flattens the device, as described above. In addition, it also involves establishing a look-up table or approximate model of the SLM response. As the response can vary across the device, one can use a region by region approach. Multi-region calibration has been performed for hologram displays [101, 102], but these procedures did not account for retardance calibration. In this chapter, a calibration method that overcomes this shortcoming is proposed.

It is also useful to be able to calibrate the SLM *in-situ*, to account for misalignment and changes in the response of the device due to mechanical or thermal drift, or changes in device properties over time. Hence, a method, including both hardware and algorithms, is presented that could be built into a simple optical system for calibration of both phase and retardance modulation. It is based on a Twyman-Green interferometer. The phase calibration process analyzes the response of the SLM both with horizontal and vertical polarized incident light. Fourier-based fringe analysis is used to extract the phase from the interferograms. Algorithms are designed to robustly gather calibration data from the interferometer in the presence of external disturbances. Data fitting and optimization are then used to obtain the phase response between the drive voltage and phase on each region. Thereafter, by just inserting an analyser and blocking the reference arm, the polarization calibration can be realized. Finally, a map providing the phase and retardance calibration for each region could be obtained. The full

calibration set-up and data processing methodology introduced in this chapter provides a comprehensive method for *in-situ* phase and retardance characterization.

4.1 Combining phase and retardance calibration

As a consequence of the manufacturing process, the SLM is not flat and so imparts a spatial phase variation (or aberration) across the beam profile. Hence, an appropriate voltage pattern is usually applied to the pixels of the SLM to cancel out the spatial variation in phase due to the effect of the non-flatness. Let us assume the SLM is used as a phase modulator designed to be used with x polarized illumination. The flatness correction phase function $\Psi(x, y)$ would ideally be defined as $\Psi(x, y) = -\Phi_x(x, y) + c$, where $-\Phi_x(x, y)$ is the phase delay experienced by x polarized light due to the non-flatness; c is an arbitrary constant phase offset.

When a voltage distribution is applied to the pixels of the SLM, then resultant phase $\Theta_x(x,y)$ seen by the x polarized light is given by:

$$\Theta_x\left(x, y\right) = \zeta_v(x, y) + \Phi_x\left(x, y\right) \tag{4.1}$$

where $\zeta_v(x, y)$ is the additional phase induced by the applied voltage. For flatness correction, this should be set equal to $\Psi(x, y)$. If the correct voltage is found such that $\zeta_v(x, y) = \Psi(x,y)$, the modulated phase then becomes

$$\Theta_x\left(x, y\right) = \Psi(x, y) + \Phi_x\left(x, y\right) \tag{4.2}$$

The y polarized components do not experience a change in phase when voltage is applied, hence

$$\Theta_y\left(x, y\right) = \Phi_y\left(x, y\right) \tag{4.3}$$

where $\Phi_y(x, y)$ is the phase delay experienced by y polarized light due to the non-flatness.

The thickness of the cell is defined as $t(x, y)$. When no voltage is applied to any of the pixels, then the OPL seen by the x polarized components of the input light would be $L_x(x, y) = 2n_e t(x, y)$ where the factor of two arises due to the reflected light passing twice through the cell. For the y polarized components, the equivalent OPL would be $L_y(x, y) = 2n_o t(x, y)$. n_o is the refractive index for the *o*-ray propagating in the liquid crystal and n_e is that for the *e*-ray. The phase delay experienced by the two polarization components is derived as:

$$\Phi_x(x,y) = \frac{2\pi}{\lambda} L_x(x,y) = \frac{4\pi n_e}{\lambda} t(x,y) \tag{4.4}$$

$$\Phi_y(x,y) = \frac{2\pi}{\lambda} L_y(x,y) = \frac{4\pi n_o}{\lambda} t(x,y) \tag{4.5}$$

where λ is the wavelength of the incident light. It is clear that:

$$\Phi_x(x,y) = \frac{n_e}{n_o} \Phi_y(x,y) \tag{4.6}$$

When substituting Eq. (4.6) into Eq. (4.3), Eq. (4.3) can be written as:

$$\Theta_y(x,y) = \Phi_y(x,y) = \frac{n_o}{n_e} \Phi_x(x,y) \tag{4.7}$$

the retardance of the SLM when the flatness correction is applied is hence

$$\Delta\Theta(x,y) = \Theta_x(x,y) - \Theta_y(x,y) = \left(1 - \frac{n_o}{n_e}\right)\Phi_x(x,y) + \Psi(x,y) = -\frac{n_o}{n_e}\Phi_x(x,y) + c \tag{4.8}$$

This makes it clear that applying a flatness correction derived for removal of phase variations in the x polarized component does not result in constant retardance across the SLM. If the SLM is used for polarization control, a re-calibration for the retardance difference is needed.

4.2 Methodology

4.2.1 Phase calibration

A simple set-up and procedure to do both phase and retardance/polarization calibration was proposed. A Twyman-Green interferometer combined with fringe analysis was used to capture the phase profile of the SLM. Here, the SLM was calibrated with both horizontal and vertical polarized incident light separately. The retardance calibration was then implemented by blocking the reference arm and inserting an analyzer before the camera.

Experimental set-up

A simple Twyman-Green interferometer for phase and polarization calibration was constructed. The schematic is shown in Figure 4.1 (a). The polarization state of the beam from the He-Ne laser (Melles Griot, 05-LHP-171, 632.8 nm) was *y* polarized. The beam was first modulated by the half wave plate (HWP) and polarizer to make sure it was perfectly *x* polarized, and the beam was then expanded to a size that overfilled the whole SLM window (LCOS-SLM Hamamatsu, X10468−07). The light passed through the Beam Splitter (BS), with one path incident onto a reference mirror and the other onto the SLM. A 4f system imaged the SLM onto the camera via the BS, from which the interferogram was captured. The lenses were configured so that one SLM pixel was equivalent to one pixel on the CMOS camera.

To determine any residual aberration in the interferometer, the SLM was initially replaced with a flat mirror and recorded an interferogram, as shown in Figure 4.1 (b). From this image a calibration measurement of the phase Φ_{static} was obtained, which represents a systematic error in measuring the phase with the interferometer. Φ_{static} was subsequently subtracted from all phase measurements of the SLM to obtain unbiased measurements. Still using the flat mirror

instead of the SLM, the susceptibility of the interferometer was verified to external disturbances such as temperature or drift, which inevitably affect our measurements. ε_i is used to denote the phase contribution due to these disturbances. Then the mean value of the phase of the plane mirror was measured every 0.75 seconds at a temperature of approximately 23°C. The recorded data is reported in Figure 4.2. It can be seen that during the three minutes, the phase offset varied due to the experimental conditions, such as mechanical drift, vibration, and temperature change. To ensure an accurate calibration of the SLM, it need to track the evolution of ε_i when collecting calibration data for the SLM.

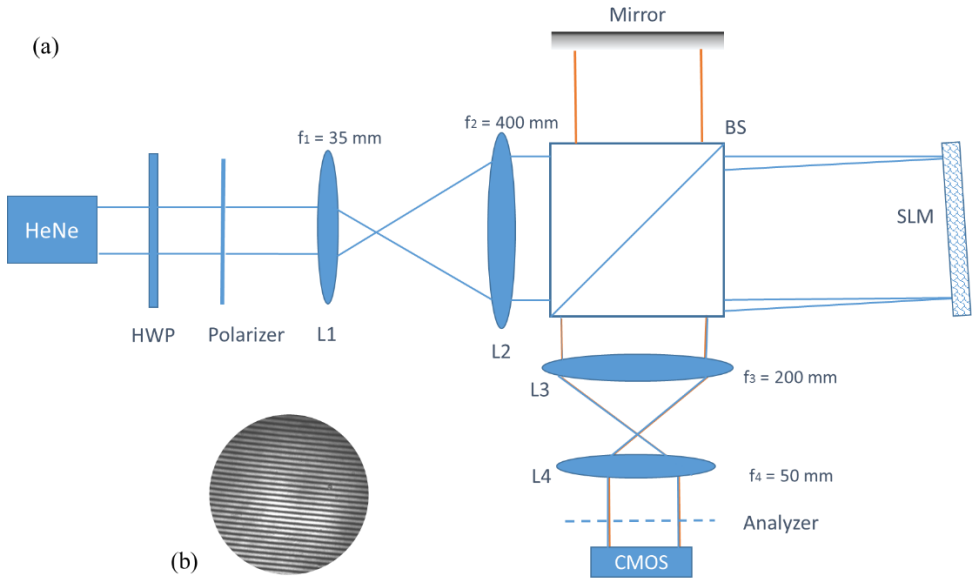


Figure 4. 1: (a) Schematic of the SLM calibration: Twyman−Green interferometer. The analyzer was inserted when doing the retardance calibration. HWP: half wave plate. BS: 50:50 beam splitter; SLM: spatial light modulator. (b) Interferogram obtained when the SLM was replaced with a flat mirror.

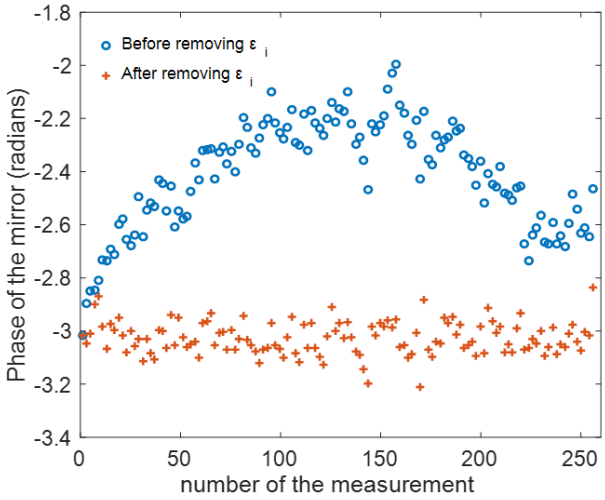


Figure 4. 2: Blue circles: mean value of the phase measured with the interferometer when the SLM was replaced with a flat mirror; Red crosses: remaining phase after removing ε_i. After removing ε_i the phase becomes stationary as expected for a flat mirror.

In order to use the SLM for precise phase modulation, it is necessary to calibrate the device to determine the relationship between the induced phase and the applied voltage. This SLM was designed for phase-only operation with the voltage-variable fast axis fixed along the *x*-axis. Hence, the HWP was set at 45° and polarizer at 0° to generate *x* polarized incident light. To perform the calibration and determine the introduced phase, a set of input-output measurements were collected. In each measurement, a uniform voltage across the whole SLM was applied and the corresponding interference pattern was measured using the CMOS camera. The voltage was represented in the control program by the integer pixel grayscale value (PGV) displayed on the SLM. The value of PGV was set to zero in the first measurement and gradually increased up to 255 in the last measurement. All the measurements were taken with the same time interval of 0.75 seconds. Throughout this process, the voltage maps were applied without use of the calibration look-up tables provided by the manufacturer.

The interferogram recorded by the camera can be expressed as:

$$I(x,y) = \left| Ae^{i\Phi_s(x,y)} + Be^{i\Phi_R(x,y)} \right|^2 = A^2 + B^2 + ABe^{i(\Phi_s(x,y)-\Phi_R(x,y))} + ABe^{i(\Phi_R(x,y)-\Phi_s(x,y))} \tag{4.9}$$

where I is the intensity, A, B are the electrical field amplitude of the light from the SLM and the reference mirror, respectively; while $\Phi_s(x, y)$ and $\Phi_R(x, y)$ are the corresponding phases.

By using the same FFT analysis in Chapter 3, the phase profile induced by the SLM could be extracted. Again, the algorithm provided the phase wrapped into the interval $(-\pi, \pi]$ radians. As a consequence, one needs to apply a phase unwrapping algorithm [66] to obtain the unwrapped phase Γ_i, where i denotes the i^{th} measurement in the set. Γ_i can be expanded into the following:

$$\Gamma_i = \Phi_i + 2k_i\pi + \varepsilon_i \tag{4.10}$$

where Φ_i is the phase modulated by the SLM; term $2k_i\pi$ with integer k_i is an arbitrary offset due to the phase unwrapping algorithm. The algorithm needs to invert the non-injective complex exponential function to build the unwrapped phase, which results in an arbitrary selection of branches given by k_i in each of the measurements. ε_i is the phase contribution caused by exogenous disturbances such as drift and temperature trends. Note that terms $2k_i\pi$ and ε_i are constant offsets that are not dependent on the spatial coordinates x and y. To perform the SLM calibration, one must obtain Φ_i and remove terms $2k_i\pi$ and ε_i as outlined in the two steps below.

Step 1: the values of k_i can be obtained by solving an ordinary one-dimensional phase unwrapping problem on the Γ_i. Then Eq. (4.10) becomes

$$\Gamma'_i = \Phi_i + \varepsilon_i \tag{4.11}$$

Step 2: to remove ε_i, a second set of reference measurements was simultaneously recorded to track the variation of the exogenous disturbances throughout time. The reference measurements are denoted with (R) and the normal, non-reference measurements with (N). The R and N

measurements were interleaved in time as depicted in Figure 4.3. In the R measurements, the PGV did not vary with index *i* and was kept at a constant value of zero throughout the set.

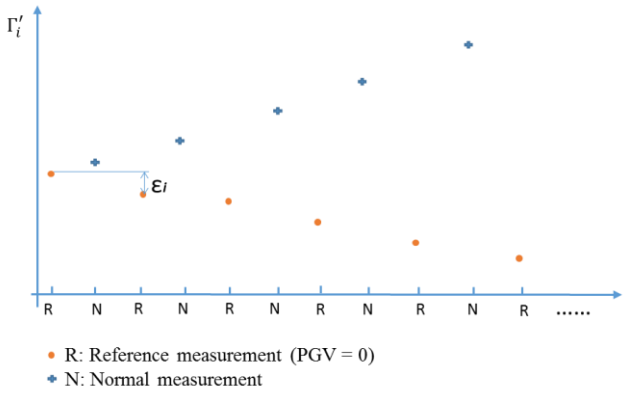


Figure 4. 3: Schematic of the measurement process. The sets of reference (R) and normal (N) measurements were interleaved in time as shown to subsequently apply interpolation and detrending.

As depicted in Figure 4.3, interpolation was used to deduce the value of ε_i in the set of the N measurements, which allowed to subtract ε_i from Γ'_i in Eq. (4.11) and finally obtain Φ_i. Figure 4.4 shows the results of this procedure for the pixel at the center of the SLM.

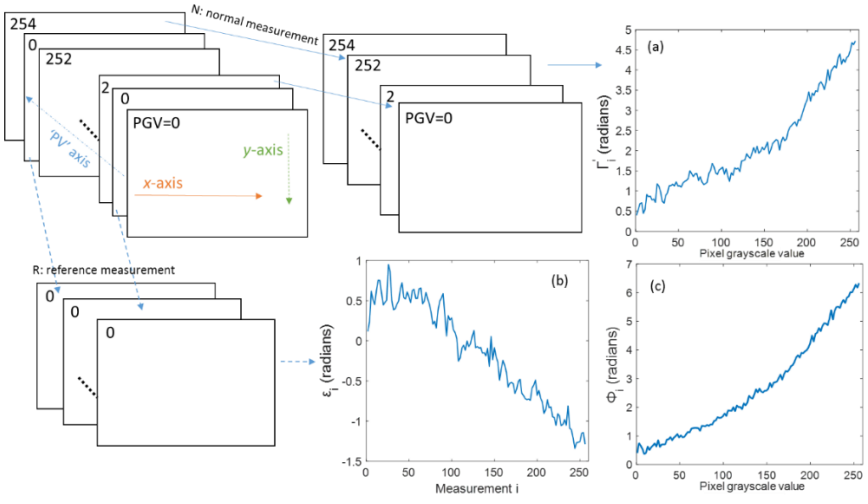


Figure 4. 4: Decomposition of the phase in the terms outlined in Eq. (11). (a) Γ'_i varying as a function of PGV at the center point of the SLM; (b) ε_i varying with the measurement *i* (c) calculated Φ_i varying as a function of PGV. For the SLM calibration, the values Φ_i shown in (c) are of interest.

Step 3: Generally, the corresponding phase can be represented by a polynomial function of the addressed voltage [24]. It is assumed the phase change varies as a third order polynomial function of voltage:

$$\Phi_S(x,y) = a_{x,y}V^3 + b_{x,y}V^2 + c_{x,y}V + d_{x,y} \tag{4.12}$$

where $d_{x,y}$ is the 'offset', which is the phase at PGV = 0. Higher order polynomials were also tried to fit the trend, but it is found that the fitting error does not change. The calibration data Φ_S was divided into a set of regions over the SLM window. Within each region, the coefficients $a_{x,y}$, $b_{x,y}$, and $c_{x,y}$ were determined by curve fitting.

Step 4: to visualize the difference of the coefficients for each region, $d_{x,y}$ was subtracted for each $\Phi_S(x, y)$, and analyzed the relative phase change comparing to PGV = 0. The whole process is illustrated in Figure 4.5.

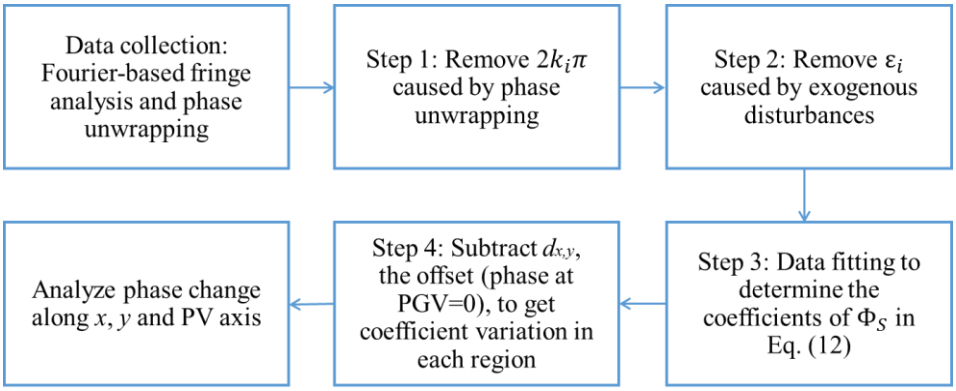


Figure 4. 5: Flow chart of the data processing and analysis method.

The above process provided calibration for the modulation of x polarized incident light. Following this, the HWP was rotated to 0° and the polarizer to 90° and the process was repeated to obtain the equivalent calibration for y polarized incident light. If the SLM performs in an

ideal way, then no phase modulation with applied voltage should be detected. However, this measurement is essential to detect any effect that may be present due to e.g. misalignment.

The previous steps provided phase calibration of the *x* and *y* polarizations separately. One could obtain the retardance by examining the difference between Φ_x and Φ_y. However, according to Eq. (4.8), there is an offset *c* that remains undetermined after the phase calibration only. Therefore, the separate retardance calibration is required.

4.2.2 Retardance calibration

For retardance calibration, the reference arm was blocked and an analyzer with transmission axes at 45° was inserted before the camera. Note that, the fast axis angle of the HWP should be fixed at 22.5°. Thus, the input light to the SLM was 45° linearly polarized and output light was viewed through a 45° analyzer.

The normalized Jones vector of the 45° linearly polarized light excluding the absolute phase was $[1, 1]^T$ and after reflection off the SLM the E_x and E_y components of the electric field both experience phase delay. This is represented by the Jones vector $[e^{i\Phi_x},\ e^{i\Phi_y}]^T$ where Φ_x and Φ_y are the phase introduced on the *x* and *y* components respectively. After passing through the analyzer, the intensity recorded on the camera can be represented as:

$$I = \left| e^{i\Phi_x} + e^{i\Phi_y} \right|^2 = 2 + 2\cos\left(\Phi_x - \Phi_y\right) = 4\cos^2\left(\frac{\Phi_x - \Phi_y}{2}\right) \tag{4.13}$$

For polarization modulation, the retardance difference introduced between the E_x and E_y components of the electric field is of interest, which is $\Phi_x - \Phi_y$. When the SLM voltage is addressed from the minimum to the maximum, the intensity should change accordingly. If

assuming the retardance variation as a function of the voltage is similar to Eq. (4.12), the intensity change can be written as Eq. (4.14), which is scaled $I \in [0,1]$:

$$I = \cos^2\left(aV^3 + bV^2 + cV + d\right) \tag{4.14}$$

Eq. (4.14) was then used to fit the intensity data I_{real} recorded from the camera to minimize error of $I_{real} - \cos^2(aV^3 + bV^2 + cV + d)$, where each measurement I_{real} was normalized to its maximum intensity. Hence, the relationship between retardance and voltage could be extracted.

4.3 Results and data processing

4.3.1 Phase calibration results with *x* polarized incident light

Figure 4.6 (a) shows Γ_i at the center point of the SLM extracted via the FFT analysis as the PGV was changed. It is seen that due to phase unwrapping, there is an arbitrary offset of $\pm 2k\pi$ radians for each data point. These piston offsets were removed in step 1 for both the R and N sets of measurements, resulting in the time series shown in Figure 4.6 (b). From the adjusted phase measurements in Figure 4.6 (b), the offsets ε_i can be extracted and removed to obtain the phase modulated by the SLM, as described in Step 2.

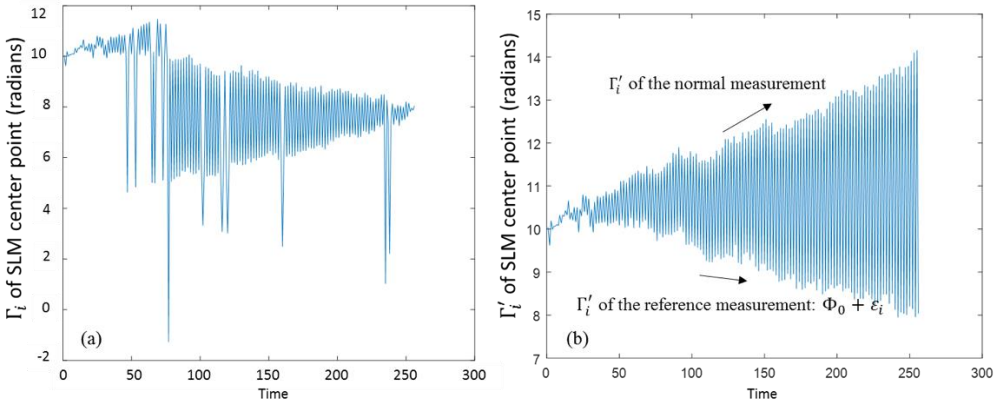


Figure 4. 6: Phase extraction results from the SLM center point (a) Γ_i (b) Γ'_i after removal of the piston offset $2k_i\pi$ introduced by the phase unwrapping algorithm.

Figure 4.7 compares Γ'_i and Φ_i as a function of PGV before and after removing the phase disturbance ε_i. The resulting phase range spans approximately 2π radians as expected. Thereafter, a third order polynomial, Eq. (4.12) was used to fit the data to get a smooth relationship between PGV and phase Φ_S. To select the order of the fitting polynomial, the fitting errors were calculated when using third order and fourth order polynomials respectively. Since this error was about 0.097 *rms* in both cases, the third order polynomial was chosen for computational simplicity.

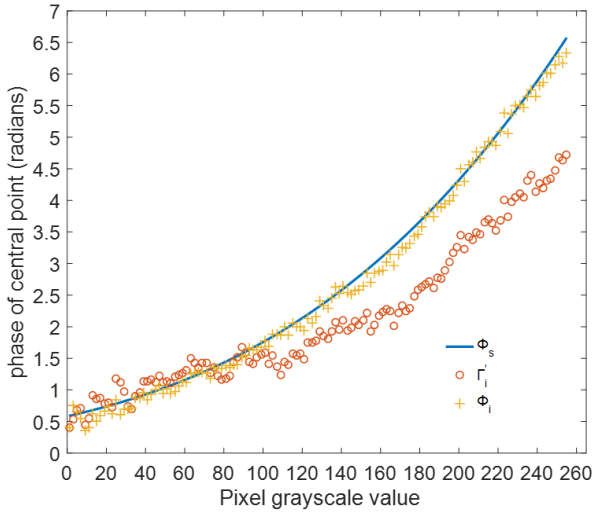


Figure 4. 7: Comparison of phase varying as PGV before and after Step 2 and 3. Red circle: Γ'_i in Eq. (4.11); yellow cross: Φ_i in Eq. (4.11); blue line: Φ_S, 3rd order polynomial fit in Eq. (4.12).

The phase was obtained from the measurement shown in Figure 4.8. As the liquid crystal devices forms a continuum, one should expect that the optical properties vary smoothly across the profile. Hence, to reduce the measurement noise and calculation complexity, the original 600×800 pixels of the SLM were divided into 30×40 sub-regions for the purposes of analysis, as shown in Figure 4.8 (a). The intensity of the acquired images was averaged over each of these sub-regions. Note that in the bottom-left hand corner a phase singularity can be seen, where the illumination intensity was low. This did not affect the measurements nearer the center of the SLM, which would be within the circular aperture of the full optical system.

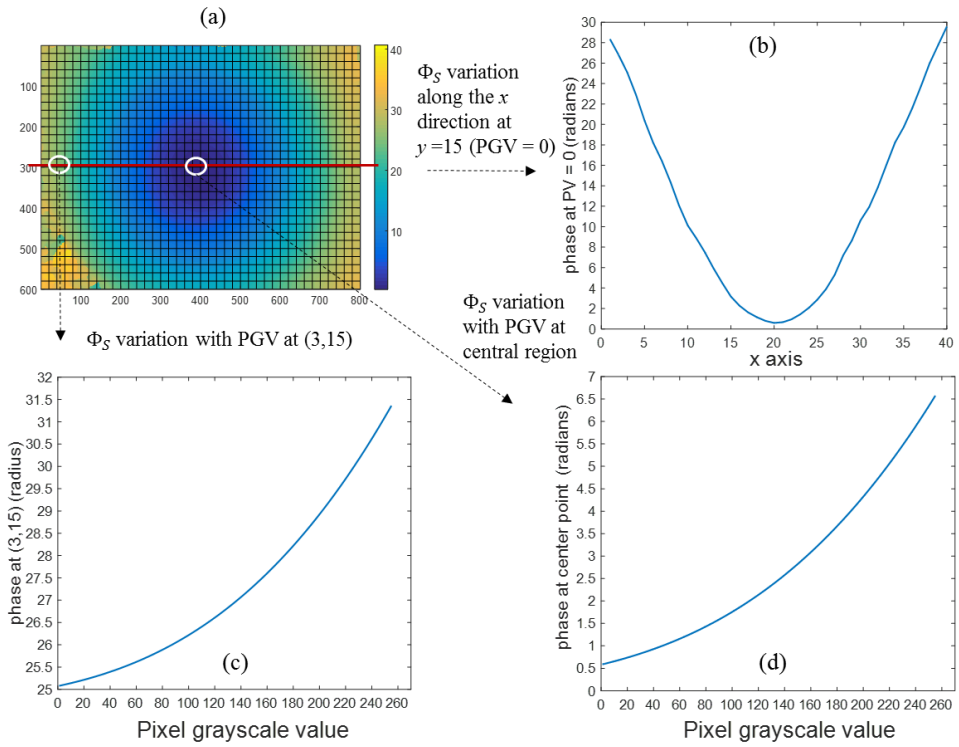


Figure 4. 8: (a) The phase map at PGV = 0, SLM was divided into 30×40 sub-regions for phase response analysis. (b) Φ_S variation along the SLM x direction at y = 15, PGV = 0; the x axis represents the x coordinate of the SLM sub-region (c) Φ_S variation with PGV at region (3,15). (d) Φ_S variation with PGV at center region.

Figure 4.8 (b) shows the unwrapped phase variation across the central line of the SLM at PGV = 0. This reveals that the SLM had significant curvature, and this curvature introduced a phase variation. Figures 4.8 (c) and 4.8 (d) show how the phase varied with PGV at different coordinates, (3,15) and (20,15) respectively. Although the initial phase offset at PGV = 0 was different, the trend after data fitting looked similar.

Figure 4.9 shows results after step 4: subtraction of the phase profile obtained for PGV = 0; this allows us to see the difference of the phase introduced by the SLM at different regions. Figure 4.9 (d) shows how the relative phase, i.e. $\Phi_S - d$ in Eq. (4.12), varies with PGV at the central region. Figures 4.9 (b) and 4.9 (c) show orthogonal cross sections through the phase modulation at PGV = 155, relative to the reference at PGV = 0. Ideally, the SLM should provide a uniform phase profile in this case. However, our data shows a non-uniform profile, which

can possible be attributed to the effects of interference with spurious reflections in the system. In the next section, a mathematical derivation of a possible explanation for the effects of such reflections is provided.

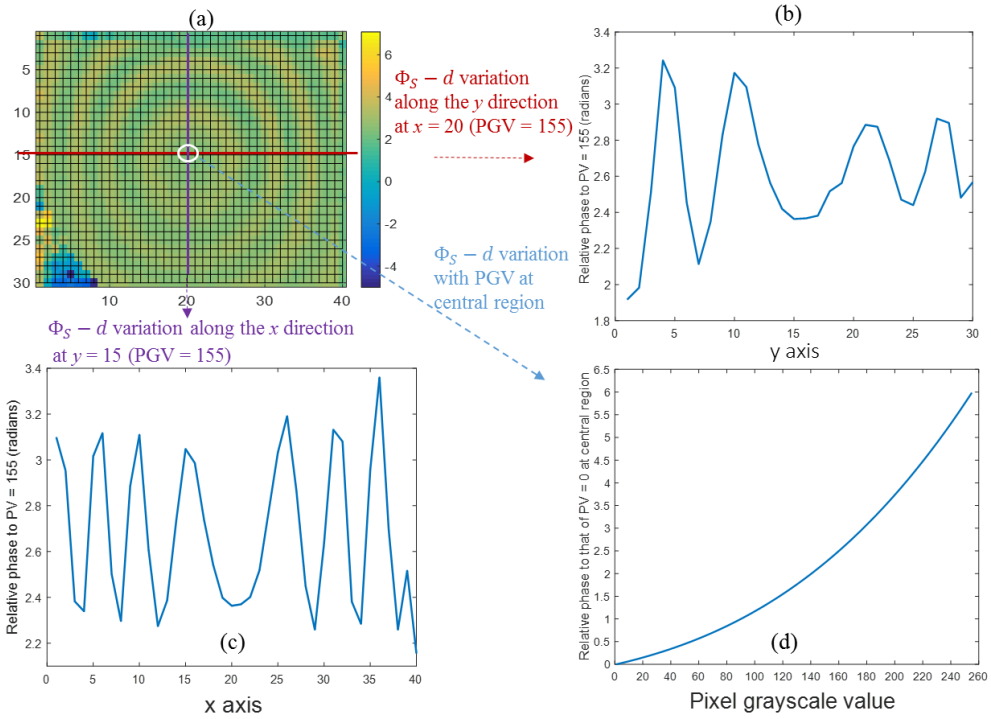


Figure 4. 9: Results after Step 4: subtraction of the phase at PGV = 0 for visualizing the polynomial coefficient differences at SLM different regions (a) The relative phase map, $\Phi_S - d$, at PGV = 155 (b) $\Phi_S - d$ variation along y direction at x = 20, PGV = 155; the y axis represents the y coordinates of the SLM sub-region (c) $\Phi_S - d$ variation along x direction, at y = 20, PGV = 155 (d) $\Phi_S - d$ variation as PGV at the center region.

4.3.2 Phase calibration results with *y* polarized incident light

Since the liquid crystal's fast axis orientation is along the x-axis, when the incident light is y polarized, there should ideally be no phase modulation. In order to measure any effects, the HWP fast axis angle and the following polarizer transmission axes were set to 90° to have y polarized incident light. The same procedure outlined in the flowchart of Figure 4.5 was followed.

Figure 4.10 (a) shows how the phase varies as a function of PGV at the center region. The circles in blue show the phase Γ' and the dots in red show the phase and Φ in Eq. (4.10) after removing the disturbance ε. It is shown that for y polarized light, the phase is predominantly constant with PGV. The cross section of Φ_S along the x direction is also shown in Figure 4.10(b). Note that without applying the procedure outlined in section 4.2 one would erroneously detect a significant phase variation due to exogenous disturbances instead of correctly detecting the negligible phase modulation induced by the SLM.

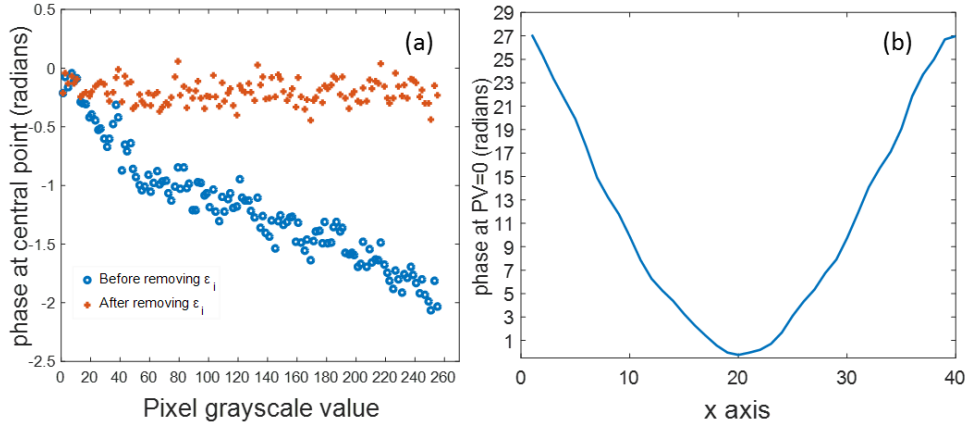


Figure 4. 10: Calibration for y polarized incident light. (a) Phase varying as a function of PGV before and after removing phase disturbance ε. Blue circle: before step 2: removing the phase disturbance; Red Cross: after step 2: removing the disturbance. (b) Phase variation along x direction at y = 15, PGV = 0.

The diffraction efficiency was then compared by applying a blazed grating. Table 4.1 reports the diffraction efficiency using, no calibration, the manufacturer calibration, and calibration described here respectively. The results are reported for two different grating periods p. The diffraction efficiency was calculated as I_1/I_0, where I_1 was the first order diffraction intensity and I_0 was the total intensity. It is seen that without calibration the diffraction efficiency is the lowest, and calibration described here shows improved performance with respect to the manufacturer calibration, on both of the grating periods.

Table 4. 1 Diffraction efficiency comparison with different SLM calibration and different blazed grating periods

Grating period	Without calibration	Manufacturer calibration	Our calibration
p = 40 pixels	84.1%	93.1%	93.5%
p = 50 pixels	84.4%	93.3%	93.9%

4.3.3 Retardance calibration

In order to perform retardance calibration, the procedure described in Section 4.3 was followed: the HWP was rotated to 22.5°, the polarizer and the analyzer transmission axes were both placed at 45° to have 45° linearly polarized incoming light. The reference path was blocked.

The intensity profiles measured for different example PGVs are shown in Figure 4.11. The variations in intensity at different positions on the SLM show that there are variations in retardance across the SLM.

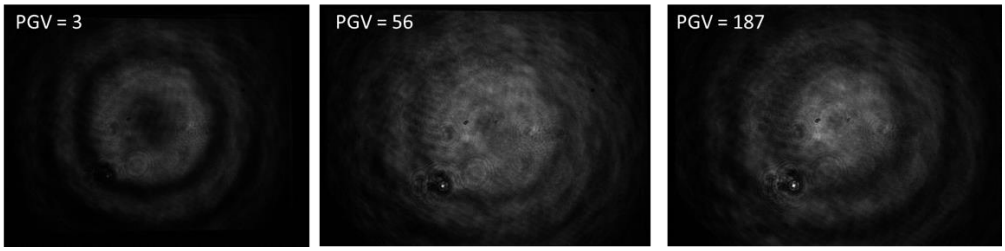


Figure 4. 11: Retardance calibration: intensity profile recorded by the camera with 45° linearly polarized input light and viewed after the analyzer at (a) PGV = 3 (b) PGV = 56 (c) PGV = 187.

Eq. (4.13) and (4.14) were used to fit the measured variation of intensity with PGV in order to obtain the retardance calibration. Figure 4.12 shows the examples of intensity data and the fit data at two different regions. The red dots in Figures. 4.12 (a) and 4.12 (c) denote the intensity recorded by the camera; the blue line is the fit obtained. Using the obtained fit, the change of retardance with PGV could be derived, as plotted in Figures. 4.12 (b) and 4.12 (d). These examples show that the SLM had a spatially variant retardance response.

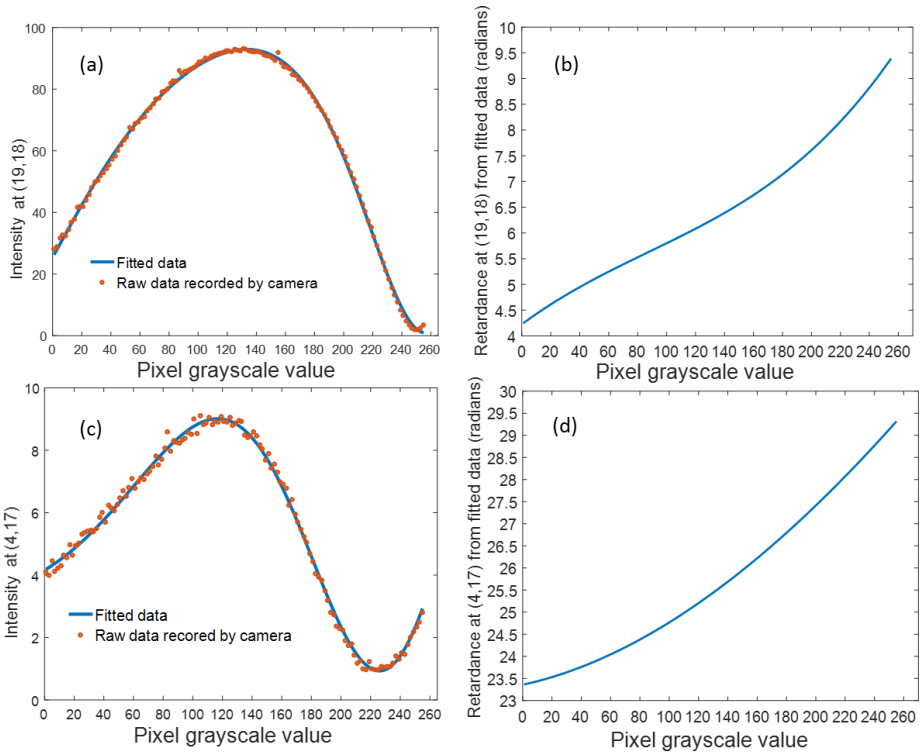


Figure 4. 12: Retardance calibration. (a) Red Dot: intensity change with PGV at region (19,18) recorded by camera. Blue Line: Fit obtained. (b) Retardance variation with PGV at (19,18) according to fitting result. (c) Red Dot: intensity change with PGV at region (4,17). Blue Line: fit obtained. (d) Retardance variation with PGV at (4,17).

4.4 Effects of the reflections from front surface of the SLM

Here the effects on the interferometer phase measurements of any unwanted reflections in the system was investigated. The effect of the front window of the SLM was modeled specifically, although the analysis is applicable to other spurious reflections in the system. For simplicity, it is assumed that there are only reflections from one surface of the cover glass and that the amplitude reflection coefficient is given by γ. Any effects of multiple reflections are ignored. Also, for simplicity, the incoming light is assumed to be *x* polarized and that the *e*-axis of the liquid crystal is aligned with the *x*-axis. As only have *x* polarized components here, the electric

field vector is described in terms of the *x* component alone. Variation across the SLM using the coordinate *x* is also shown, although in reality the coordinate variables should be (*x*,*y*).

The SLM input field is defined as $E_{in}(x) = 1$. The interferometer reference is taken to be the same: $E_{ref} = 1$. Following modulation by the SLM, the output field is:

$$E_{out}(x) = (1-\gamma)e^{i\Phi_x(x)} \tag{4.15}$$

The reflected light would have the field:

$$E_{refl}(x) = \gamma e^{iF(x)} \tag{4.16}$$

where $F(x)$ is the is the phase profile of the reflected light due to the non-flat front surface of the SLM, according to Eq. (4.4), it can be denoted as $F(x) = OPL \times 4\pi/\lambda$. The total output field after the SLM would be the sum of the output and reflected fields:

$$E'_{out}(x) = E_{out} + E_{refl} = (1-\gamma)e^{i\Phi_x(x)} + \gamma e^{iF(x)} \tag{4.17}$$

Let $\xi(x) = F(x) - \Phi_x(x)$ so that:

$$E'_{out}(x) = e^{i\Phi_x(x)}\left[1+\gamma\left(e^{i\xi(x)}-1\right)\right] = A(x)e^{i\Phi_x(x)} \tag{4.18}$$

where $A(x) = 1 + \gamma(e^{i\xi(x)} - 1)$. It is noted that for $\gamma << 1$, then $|A| \approx 1$. For the same approximation, the argument is given by:

$$\arg(A) = \arctan\left(\frac{\gamma\sin\xi}{1-\gamma+\gamma\cos\xi}\right) \approx \arctan\left(\gamma\sin\xi\right) \approx \gamma\sin\xi \tag{4.19}$$

The interference field would be the output field plus the reference field, which is:

$$E_{\text{int}}(x) = E'_{out}(x) + E_{refl} = 1 + Ae^{i\Phi_x(x)} \approx 1 + e^{i\left(\Phi_x(x)+\gamma\sin\xi(x)\right)} \tag{4.20}$$

and the measured interference intensity would be:

$$I(x) = \left|E_{\text{int}}(x)\right|^2 \approx \left|1 + e^{i(\Phi_x(x) + \gamma \sin \xi(x))}\right|^2 = 4\cos^2\left(\frac{\Phi_x(x) + \gamma \sin \xi(x)}{2}\right) \tag{4.21}$$

From these expressions, it is clear to see that the effective phase measured by the interferometer will be:

$$\Phi_{measured} \approx \Phi_x + \gamma \sin \xi = \Phi_x + \gamma \sin\left(F - \Phi_x\right) \tag{4.22}$$

which illustrates that the reflection from the front and back cell could be possible explanation of the apparent shape of the phase ripple in Figure 4.9 (a). The specific calculation here has modelled the effect of a reflection from the front surface of the SLM. However, the analysis could be more generally extended to reflections from other surfaces in the system.

The results in Figure 4.9 suggest phase variations in the range 0.5 to 1 radian peak to peak. Using this modelling, it is found that ripples of the order of 0.5 radians can be obtained for situations where $\gamma = 0.2$, which corresponds to an intensity reflection of around 4% of the illumination. This hypothesis matches the shape of the phase patterns, which in turn depends on the distortion of the front and back surfaces of the SLM cell. Experimental measurements show the spurious reflection from the SLM to be <1% with same wavelength. However, there are additional reflections from other components, such as the beam splitter, that have a compounded effect.

4.5 Summary

Since liquid crystals are sensitive to exogenous factors, such as temperature, and since SLMs exhibit spatial variations due to manufacturing, calibration of SLMs is important in precision

applications. In this chapter, it shows that using an SLM for polarization modulation requires performing an ad-hoc calibration procedure that is fundamentally different from conventional phase-only calibrations. Our arguments and data show that one should expect non-negligible errors in the control of the retardance when using phase-only calibrated SLMs. Therefore, a different calibration procedure that addresses these shortcomings is provided here.

The presented method requires only simple interferometer hardware, thus making this compatible with *in-situ* calibration, within an adaptive optical system. As the algorithm allows us to remove the effects of external phase disturbance, the requirements for stability of the interferometer are reduced, which permits implementation with simpler hardware. The methodology presented in this chapter for region by region calibration of the SLM for both phase and polarization modulation will have valuable applications in adaptive correction systems.

Chapter 5 Polarization State Generation and Imaging Polarimeter

Adaptive optics has predominantly focused on the correction of phase aberrations [13, 17, 103], but there are many optical systems where polarization errors can also have detrimental effects on performance. While polarization control of a whole beam is a commonplace component of many optical systems, spatially variant control of polarization across a beam profile is also used, such as for manipulation of vector beams [104-106]. However, there are many reasons why spatially varying polarization errors can be introduced in a system, such as the effects of internal stresses in optical components, dielectric coatings, or birefringent materials [107]. In microscopes, for example, spatially varying dependent polarization errors can arise from specimen birefringence or Fresnel effects when focusing by high numerical aperture optics through interfaces with refractive index mismatch [108-112]. In certain microscope applications, polarization plays an important role e.g.in STED microscopy, polarization errors can cause a non-zero intensity at the center of the depletion beam [113]; in SIM, the contrast of the sinusoidal illumination patterns is dependent upon the use of appropriate polarization [12, 114]. It is therefore clear that adaptive control of polarization could be beneficial in such cases.

The basic concept of adaptive polarization correction is similar to that used for correction of phase aberrations. To achieve adaptive polarization control, both a method of polarization modulation and a method for sensing the polarization state are required. The principle is shown in Figure 5.1. Strategies for building an arbitrary polarization generator and imaging polarimeter are introduced in this chapter.

A liquid crystal SLM based polarization generator was selected for polarization control as it has been implemented in various configurations for different applications such as investigating the principal modes in a multimode fiber [75], arbitrary polarization generation [76, 79] and quantum logic [83]. As for the polarization sensing, a wide range of imaging polarimeters could be employed by using prisms [115, 116], liquid crystal variable retarders [117] or interferometric methods [118-120]. In this chapter, the Sagnac interferometer and Stokes polarimeter were compared.

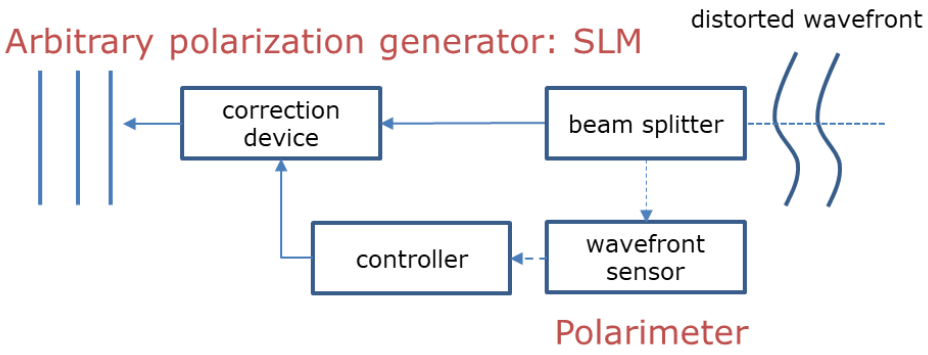


Figure 5. 1: The principle of adaptive polarization control is similar to phase control principle. The polarization state generator (PSG) serves as the correction device while the polarimeter serves as the wavefront sensor in AO.

5.1 Polarization state generator

5.1.1 Methodology

An SLM can control the polarization state across a beam as each pixel acts like a separate retarder [50, 76, 79, 121-123]. Since the pattern can be adapted to apply to the SLM, the retardance of the beam can be controlled.

However, a single pass off the SLM will perform like a retarder at a fixed orientation and it cannot alter the input light to any polarization state. Linear retarders have two eigenmodes (along fast and slow axis) that are vectors starting at the origin of a Poincaré sphere and have opposite directions *i.e.* together they form a continuous line through the centre of the sphere. A linear retarder's action on the polarization state can be visualised easily on the sphere, as shown in Figure 5.2: rotate the initial position on the sphere about the line that makes an angle 2θ to the S_1 axis by an angle equal to the retardance; θ is the angle of the fast axis to the horizontal. Full polarization control is equivalent to being able to access each point on the sphere, which cannot be done by a single pass off the SLM. In order to access the whole surface of the Poincaré sphere, a fast axis rotation on the Poincaré sphere is needed after the first pass off the SLM, which is then followed by another rotation on the sphere by using another pass off another SLM. This double pass process is shown in Figure 5.3 (a). If start from the 45° linear polarization state and the first pass of the SLM would change the state around S_1 axis and end at any point on the green circle, e.g. point A; then the second pass will start from point A, and rotate the polarization state across S_2 axis. In this way, all the points on the sphere are accessible. However, if the input polarization state is not perfect 45° linearly polarized, as

shown in Figure 5.3 (b), since the green circle is not a great circle, the sphere surface to the right of the orange circle is inaccessible.

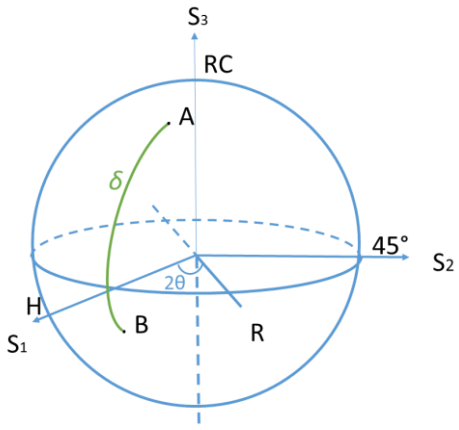


Figure 5. 2: A linear retarder effect on the polarization state on the Poincaré sphere. The input state is at point A. It rotates across the axis that has an angle of 2θ to S_1 axis, and change the retardance of δ.

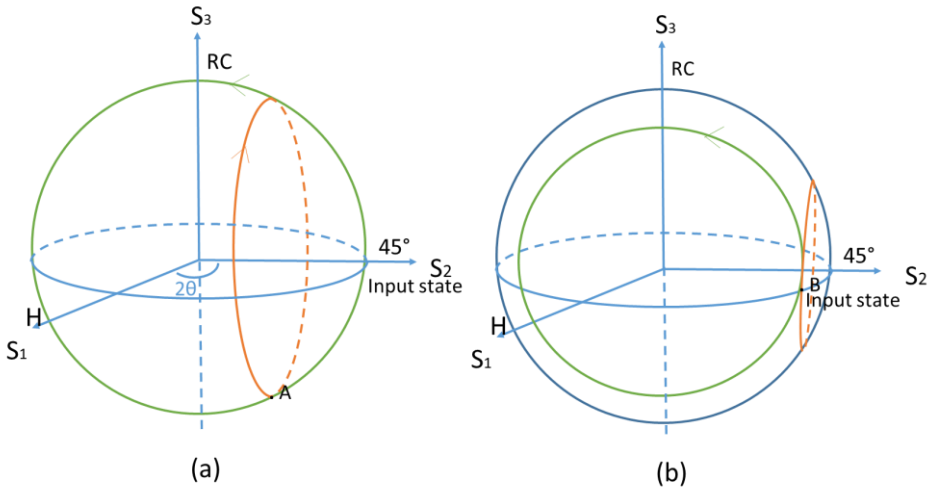


Figure 5. 3: (a) The first pass on the SLM is equivalent to rotate the polarization state from the input 45° linear polarization to any point on the green circle. The second pass on the SLM is equivalent to rotate the polarization state from the ending point on the first pass around S_2 axis (orange). (b) When the input polarization state is not 45° linearly polarized, the sphere surface to the right of the orange circle is not accessible.

5.1.2 Experimental set-up

In reality, using two separate SLMs will increase the complexity and difficulty in system integration [79, 124, 125]. Instead, a single SLM can be used twice. The SLM surface was divided into two parts as shown in the dashed line window in Figure 5.4. In order to operate the SLM to modulate the phase shift between E_x and E_y, the illuminating light should be polarized at 45 degrees to the ordinary axis. The laser source used is the same with the one used in Chapter 3. As most laser sources have a vertical/horizontal polarization state, before the first pass on the SLM, a HWP was used to rotate the angle of the polarization state. After the first pass of the SLM, the polarization state is rotated. By using a QWP and a mirror. After passing the QWP twice, the returning beam axis was rotated 90 degrees and now can change its polarization state again by passing the second time through the SLM. As a result, the final state of this beam was modulated and can research any point on the Poincaré sphere surface. The system used two passes from an SLM to control the polarization state. The two halves of the SLM were oriented 45° relative to each other, such that the first pass rotated the polarization state about the S_1 axis and the second pass rotated about the S_2 axis as shown in Figure 5.3 (a). In doing this, It can be seen that every point on the sphere can be accessed. Figure 5.4 shows the schematics of the modulation part.

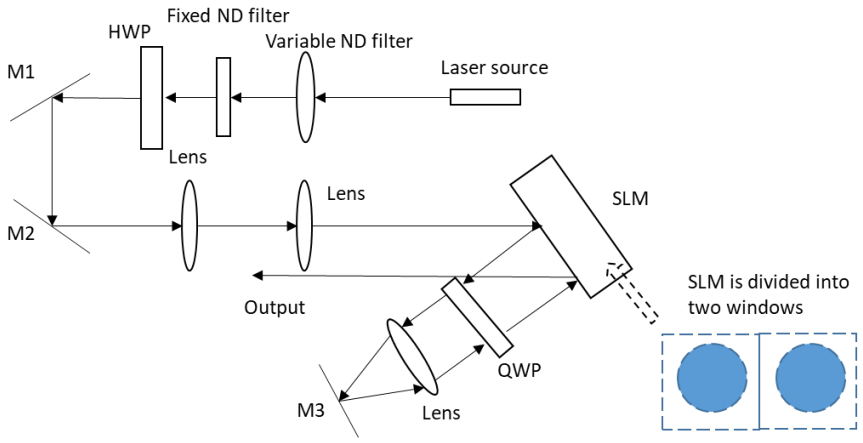


Figure 5. 4: Schematics of the dual pass SLM polarization modulation scheme. The SLM was divided into two windows to realize dual-pass modulation.

Here, Jones matrix is used to show the derivation of the output Jones vector and how this system could access all the polarization states. As introduced in Chapter 2, the output polarization state can be represented as: $\overrightarrow{J_{out}} = J_{mod}\overrightarrow{J_{in}}$, where J_{mod} is the Jones matrix of the modulation part. Here the input light is vertically polarized, so the input light Jones vector is simply $[0, 1]^T$. The Jones matrix of a retarder is:

$$J_R(\varphi) = \begin{pmatrix} e^{i\varphi/2} & 0 \\ 0 & e^{-i\varphi/2} \end{pmatrix} \tag{5.1}$$

where ϕ is the retardance. When the fast axis of a retarder has an angle θ to the polarization direction of with the incident beam, the rotation matrix should be applied and the output field will be equal to:

$$J_R(\varphi, \theta) = J(-\theta)J_R(\varphi)J(\theta) \tag{5.2}$$

where, $J(\theta)$ is the rotation matrix:

$$J(\theta) = \begin{pmatrix} \cos\theta & \sin\theta \\ -\sin\theta & \cos\theta \end{pmatrix} \tag{5.3}$$

For the pattern applied on the SLM, the retardance is customized. In terms of the HWP and QWP, the rotation angle is 22.5° to the horizon axis. It should be noted that the state changes

after the first pass beam is reflected by the mirror because of the change of propagation direction and thus the angle of the second pass of the QWP should be -22.5°. According to these matrices, the polarization state after each component can be calculated. Figure 5.5 shows an example of the output field with the retardance of the SLM set to 0.

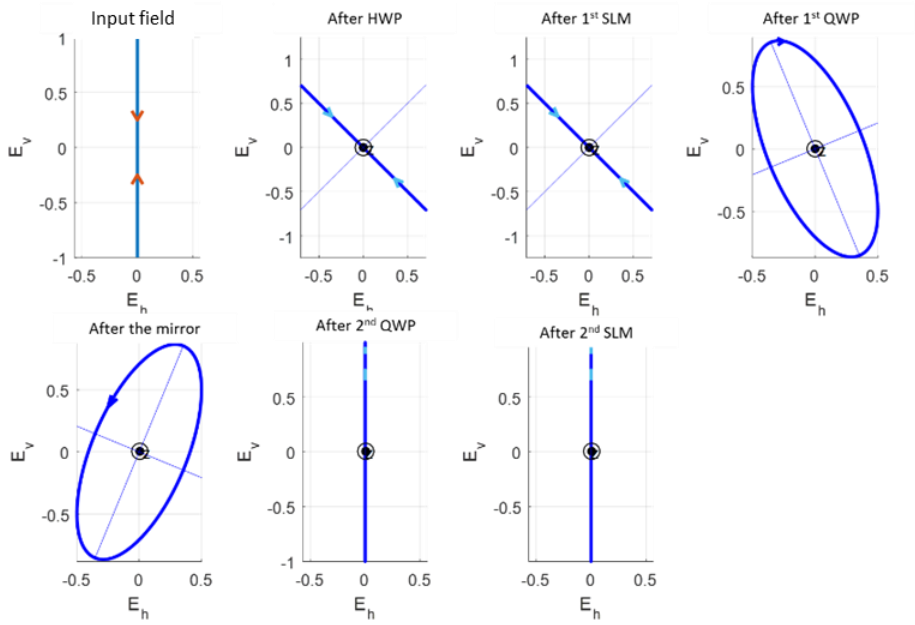


Figure 5. 5: Polarization state after each component with the SLM retardance set to 0.

As mentioned above, two passes off a single reflection mode SLM is used with two passes through a QWP in between the SLM passes. The Jones vector from the output light can be represented in the following form:

$$\overrightarrow{J_{out}}(x,y) = J_{\mathrm{SLM2}}(\delta_2,x,y)\, J_{\mathrm{QWP}}(-22.5°)\, J_{\mathrm{mirror}}\, J_{\mathrm{QWP}}(22.5°)\, J_{\mathrm{SLM1}}(\delta_1,x,y)\, J_{\mathrm{HWP}}(22.5°)\, \overrightarrow{J_{in}} \quad (5.4)$$

where the matrices represented in the form J are the Jones matrices of the relevant optical component, δ_1 is retardance set on the first pass of the SLM surface, δ_2 is the retardance on the second pass, x, y represent the coordinates on the SLM. Therefore, the vector $\overrightarrow{J_{out}}(x,y)$ could be simplified as:

$$\overrightarrow{J_{out}}(x,y)=\begin{bmatrix}\sin\frac{\delta_1(x,y)}{2}\, e^{\frac{\pi-\delta_2(x,y)}{2}} \\ \cos\frac{\delta_1(x,y)}{2}\, e^{\frac{\delta_2(x,y)}{2}}\end{bmatrix} \tag{5.5}$$

By controlling the voltages applied to the SLM, one could set the desired δ_1 and δ_2 to reach any point on the Poincaré sphere.

5.1.3 Calibration and alignment

Since the windows for the two passes on the SLM need to be accurate and conjugated to each other, careful system alignment and calibration is needed. In this section, the alignment method is described.

As shown in Figure 5.4, the incident light is not perpendicular to the SLM. Due to the limited space of the double pass system, the angle of the incident beam from the SLM is larger, which is around 8°. In this case, the fast axis misalignment of the liquid crystal in the SLM can introduce a small but problematic error and the error accumulates in the two passes. Therefore, the effect of fast axis misalignment is investigated later in this section.

Alignment

Since the SLM window is divided into two parts, the two effective areas need to be aligned. To make sure the second beam is perfectly aligned with the first pass on the SLM, a lens after the second pass was included and a camera was placed at the conjugate plane. The diagram is shown in Figure 5.6. By applying an image with two quartered circles that is shown in Figure 5.7 (a), the position of the second beam on the SLM can be checked, and tuned by translating M3.

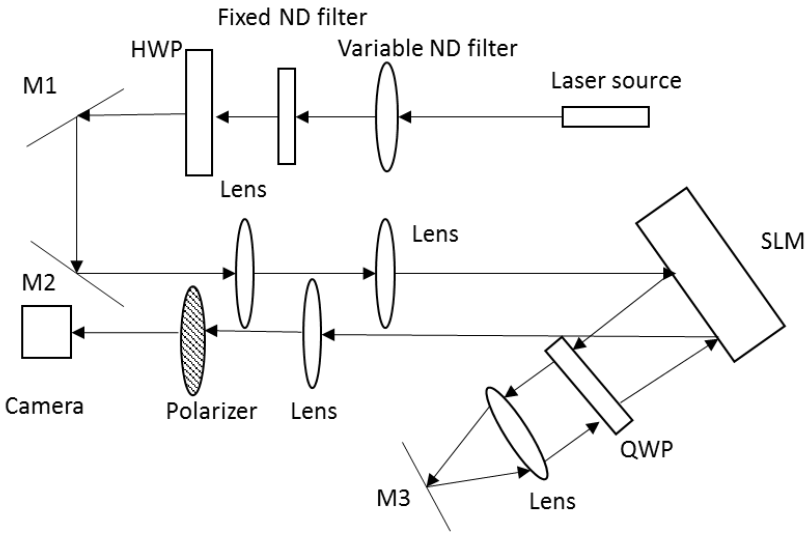


Figure 5. 6: Schematic of the PSG alignment set up.

The 4f system between the first and second pass can therefore be tuned according to the image recorded by the camera. To verify if the beam after twice passing off the SLM has the expected polarization state, different patterns were generated and observations were made of the output light. The patterns loaded on the SLM and the images recorded by the camera with vertical and horizontal polarizer axis are shown in Figure 5.7.

5.1 Polarization state generator

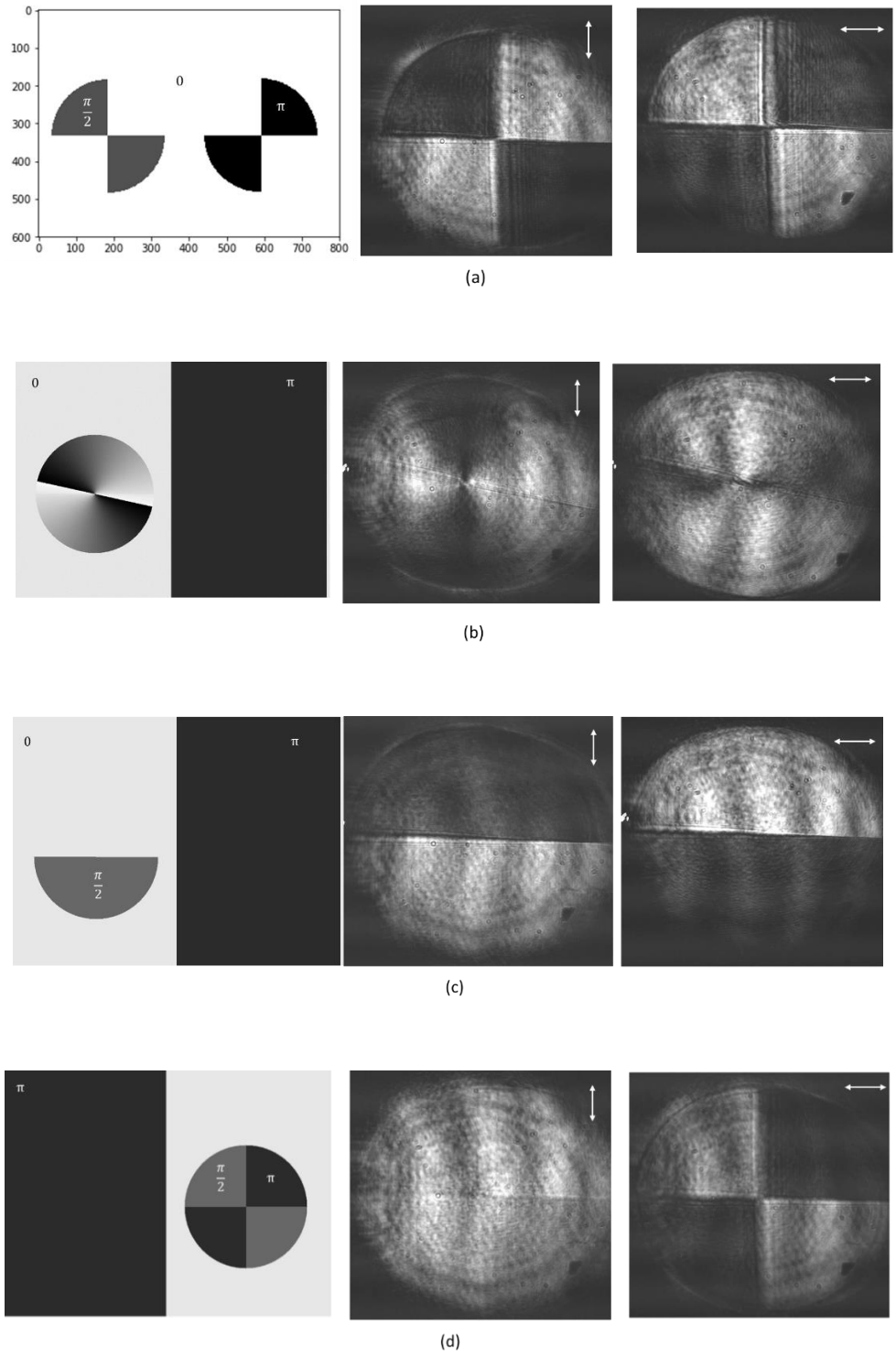


Figure 5. 7: Generated pattern with retardance labelled on different parts (left image); and its image recorded by camera after applying the pattern on the SLM through a linear polarizer with transmission axis aligned with white arrows at vertical (middle image) and horizontal (right image)

In Figure 5.7 (a), the dark part of the left window has the retardance of π and the right window of π/2. Other parts are 0. In Figure 5.7 (b), in each half circle, the retardance changes from 0 to π; the right window has the constant retardance of π. The left window of Figure 5.7 (c) only have half circle retardance of π/2 (bottom part) and the right window is still π. For Figure 5.7 (d), the left window keeps as π while the other parts outside the circle on the right window is 0; inside the circle, two of the quarters have the value of π/2 and the other two have the value of π. It is seen that as the loaded pattern changes, the polarization of the different parts of the beam is correspondingly different with no cross-talk. It proves that the two SLM windows have been aligned. Nevertheless, if the liquid crystal in the SLM has fast axis misalignment during manufacturing, it would impair the polarization modulation accuracy.

Simulation of the liquid crystal fast axis misalignment effect

In the previous chapter, calibration of the SLM with a single pass method has been introduced. The SLM used in the double pass system is different to that demonstrated in Chapter 4, as this SLM (Hamamatsu, LCOS-SLM, X10468-02) was a different model specified of 780 nm. However, when doing the individual calibration for this SLM using the method described in Chapter 4, it was found that for pixel values from around 150 to 255, there was minimal change to the state of the SLM. In other words, when PGV was varied in the range 150 to 255, there was no appreciable change in phase modulation. Also, the phase range was as large as 4π radians for *x* polarized light within the PGV range from 0 to 150. This again proves that SLM calibration is important to give a reference when using for phase/polarization control.

To see the effect of the misalignment of the liquid crystal on the Stokes parameters, one need to investigate the ideal Stokes parameters. Therefore, the Müller matrix is used here. In general, the Müller matrix of a variable retarder can be written as:

$$M_r = \begin{bmatrix} 1 & 0 & 0 & 0 \\ 0 & \cos^2 2\theta_r + \sin^2 2\theta_r \cos\delta & 0.5 \sin 4\theta_r \, (1 - \cos\delta) & -\sin 2\theta_r \sin\delta \\ 0 & 0.5 \sin 4\theta_r \, (1 - \cos\delta) & \sin^2 2\theta_r + \cos^2 2\theta_r \cos\delta & \cos 2\theta_r \sin\delta \\ 0 & \sin 2\theta_r \sin\delta & -\cos 2\theta_r \sin\delta & \cos\delta \end{bmatrix} \quad (5.6)$$

where θ_r is the fast axis angle of the retarder and δ is the retardance. If the fast axis angle $\theta_r = 0$, then $M_{r,0}$ becomes:

$$M_{r,0} = \begin{bmatrix} 1 & 0 & 0 & 0 \\ 0 & 0 & 0 & 0 \\ 0 & 0 & \cos\delta & \sin\delta \\ 0 & 0 & -\sin\delta & \cos\delta \end{bmatrix} \quad (5.7)$$

The Stokes vector of the output light after the double pass is represented as:

$$S_{\text{out},x,y} = M_{\text{SLM2}}(\delta_2, x, y) M_{\text{QWP}}(\text{-}22.5°) M_{\text{mirror}} M_{\text{QWP}}(22.5°) M_{\text{SLM1}}(\delta_1, x, y) M_{\text{HWP}}(22.5°) \, S_{\text{in}} \quad (5.8)$$

If the fast axis of the liquid crystal is perfectly aligned to the *x*-axis, then the output light Stokes parameters can be calculated as:

$$\begin{bmatrix} S_0 \\ S_1 \\ S_2 \\ S_3 \end{bmatrix} = \begin{bmatrix} 1 \\ -\cos\delta_1 \\ \sin\delta_1 \sin\delta_2 \\ \sin\delta_1 \cos\delta_2 \end{bmatrix} \quad (5.9)$$

However, if the fast axis orientation is slightly misaligned, the Stokes parameters will change. Figure 5.8 shows simulations when the liquid crystal fast axis was at a small angle of $\frac{\pi}{100}$ rad; the graphs show how S_1, S_2 and S_3 varied when the first pass retardance was fixed and only the second pass retardance was changed. Ideally, S_1 should not change as indicated in Eq. (5.9); the curves for S_2, S_3 should be symmetric about the horizontal axis. However, when the fast axis angle was changed to $\frac{\pi}{100}$ rad, S_1 was no longer constant and S_2 and S_3 were not symmetric about the horizontal axis.

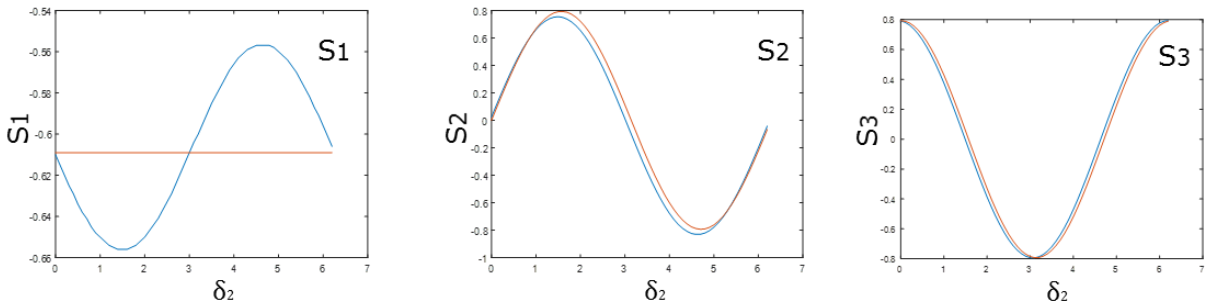


Figure 5. 8: Simulation of the Stokes parameters when the retardance of the first pass is fixed at an arbitrary value of $\delta_1 = \frac{7\pi}{24}$ rad (this angle is chosen since the deviation is obvious to see) and the second pass of the retardance is changed from 0-2π. The blue line is the Stokes parameter when $\theta = \frac{\pi}{100}$ rad and the red line is ideal case: when θ = 0 rad.

Then a simulation keeping the second pass retardance fixed and changing the first pass retardance was performed. From Eq. (5.9), S_1, S_2 and S_3 should all be symmetric about the horizontal axis. However, even when the misalignment angle was as small as $\frac{\pi}{100}$ rad, the distortion of the Stokes parameters was larger, as can be seen in Figure 5.9.

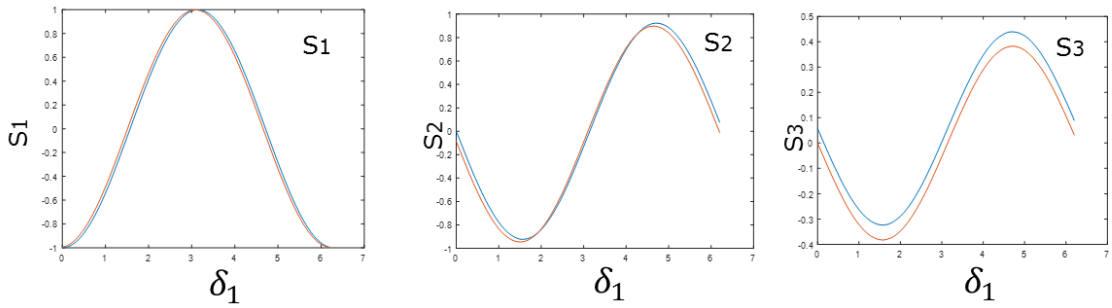


Figure 5. 9: Simulation of the Stokes parameters when the retardance of the second pass is fixed at an arbitrary value of $\delta_2 = \frac{11\pi}{8}$ rad and the second pass of the retardance, δ_1, is changed from 0−2π. Blue line is the Stokes parameter when $\theta = \frac{\pi}{100}$ rad and the red line is ideal case: when θ = 0 rad.

However, if the QWP in the PSG was removed, the compounded error would be reduced since the QWP is operated to rotate the fast axis of the liquid crystal. If the liquid crystal fast axis is misaligned, the second pass would have more compounded errors. Figure 5.10 shows the

misalignment effect after removal of the QWP. In summary, the QWP can accumulate the errors if the SLM liquid crystal fast axis is misaligned so calibration on the double pass system is needed.

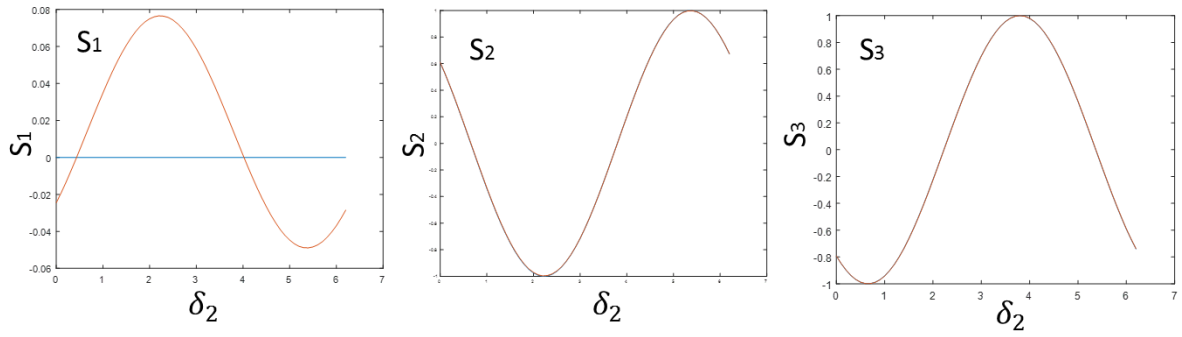


Figure 5. 10: Simulation of the Stokes parameters after removing the QWP, fixing the retardance of the first pass of $\delta_1 = \frac{7\pi}{24}$ rad, and changing the second pass of the retardance, δ_2, from 0−2π. The blue line is the Stokes parameter when $\theta = \frac{\pi}{100}$ rad and the red line is ideal case: when θ = 0 rad.

Examination of the SLM liquid crystal fast axis

Based on the above simulations, the Stokes parameters were tested to find out whether the fast axis was misaligned in the SLM in our system. First, the PGV of the first pass was fixed and only the second pass was changed from 0 to 255 as shown in Figure 5.11. The S_3 was not exactly symmetric to the line of y = 0 and S_1 was not constant. It is noted that the response was flat at high PGV, and that is because the effective range of this SLM as confined to PGVs approximately from 0 to 150 as stated at the beginning of this section.

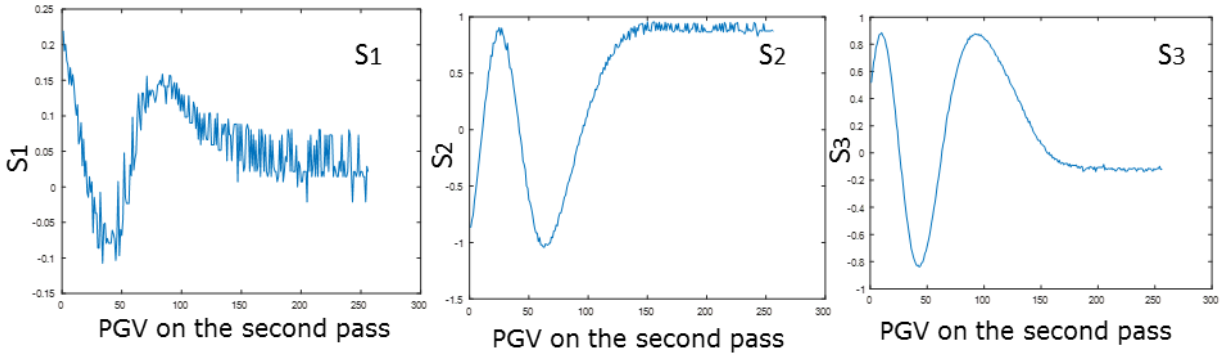


Figure 5. 11: Stokes parameters measurement of the center region of the output light when the first pass PGV was fixed at 100 and the second pass PGV was varied from 0−255.

When the second pass PGV was fixed and the first pass retardance was changed, the response of the SLM is shown in Figure 5.12 and 5.13. The difference in the two figures are the different first pass fixed retardance. It is seen that the asymmetry of the Stokes parameters also related to the first pass fixed pass retardance. S_2 has smaller deviation but S_3 has larger deviation in Figure 5.12 compared to those in Figure 5.13. Hence, the SLM used in the PSG needed to be calibrated with the system.

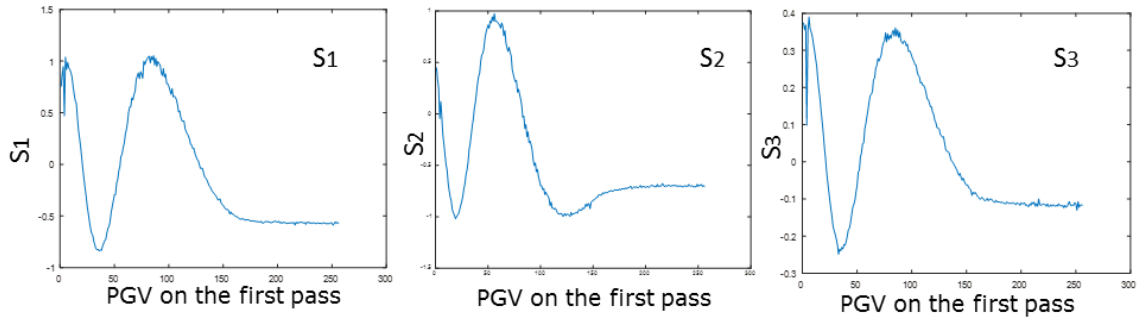


Figure 5. 12: Stokes parameters measurement of the center region of the output light when the second pass PGV was fixed at 140 and the first pass PGV was varied from 0−255.

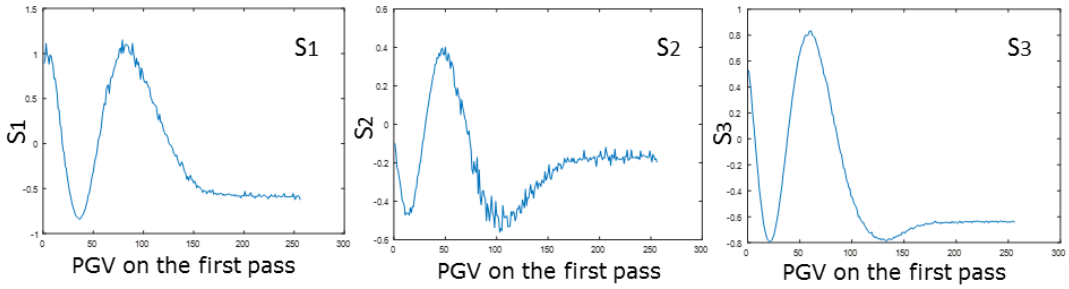


Figure 5. 13: Stokes parameters measurement of the center region of the output light when the second pass PGV was fixed at 100 and the first pass PGV was varied from 0−255.

5.2 Imaging polarimeter

In order to measure the spatial variations of polarization properties across the beam, an imaging polarimeter is required. Several polarimeter configurations could potentially be used, such as those based on a Sagnac interferometer [126], Wollaston-prism [115], compensators arrays [127], optimized Stokes polarimeter [128] etc. Two kinds of polarimeters were built and tested here, a modified Sagnac interferometer and the optimized Stokes polarimeter. The pros and cons of each polarimeter are discussed in this section.

5.2.1 The modified Sagnac interferometer

An interferometer which is similar to a Sagnac interferometer was used to analyse the beam polarization states [126]. The schematics of the interferometer is shown in Figure 5.14. This set-up permits the retrieval of polarization information from the interference patterns obtained on a camera. The method was modified by inserting two lenses between the polarization beam splitter (PBS) and one of the mirrors to have a better control of the fringe pattern on the camera. An example fringe image from the system is shown in Figure 5.15.

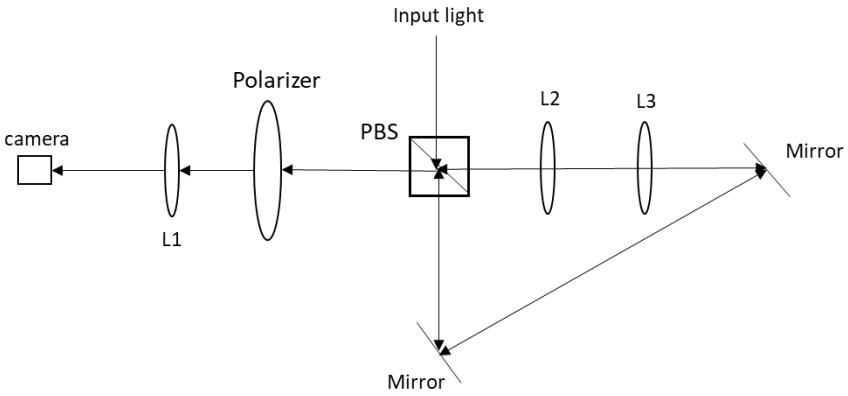


Figure 5. 14: Schematics of the interferometer imaging polarimeter.

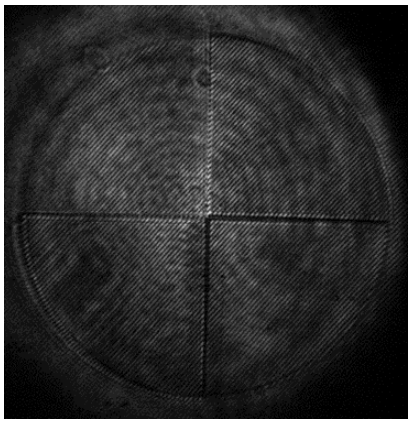


Figure 5. 15: Example fringe image from the modified Sagnac interferometer.

The input light was split as E_x and E_y by the PBS. The two split beams pass through the triangular path in opposite directions. The reflected beam went through the telescope first and was then reflected by the mirrors, while the transmitted beam was reflected by the mirrors first and then passes through the two lenses. The pair of lenses was required in order to shear the beams slightly before interference and hence create dense interference fringes at the camera. At the exit of the interferometer, the beams have polarizations along two orthogonal directions, a polarizer was required before the camera in order to analyse interference fringes in one direction.

Since one of the beams transmitted via the PBS twice and the other is reflected twice, the electrical field of the combined beam can be represented in the following form [126]:

$$E_1 = P(\theta)P(0)P(0)\begin{pmatrix}E_x\\E_y\end{pmatrix}e^{(i\varphi_1)}$$

$$E_2 = P(\theta)P\left(\frac{\pi}{2}\right)P\left(\frac{\pi}{2}\right)\begin{pmatrix}E_x\\E_y\end{pmatrix}e^{(i\varphi_2)} \quad (5.10)$$

here, ϕ_1 and ϕ_2 are the initial phase of the two beam, $P(\theta)$ is the Jones matrix of a polarizer orientated at angle of θ that can be written as :

$$J_p(\theta) = \begin{pmatrix}\cos^2\theta & \sin\theta\cos\theta\\ \sin\theta\cos\theta & \sin^2\theta\end{pmatrix} \quad (5.11)$$

The intensity when the two beam interference at any point Q is $I(Q,\theta) = \langle(E_1 + E_2)\cdot(E_1^* + E_2^*)\rangle = I_c(Q,\theta) + I_{int}(Q,\theta)$, where the '<>' represents time average. The total intensity can be represented as the sum of incoherent addition $I_c(Q,\theta)$ and the interference $I_{int}(Q,\theta)$ of the orthogonal components of the incident light (I_m=J_{mm}) at the direction of the polarizer:

$$I_c(Q,\theta) = I_x cos^2\theta + I_y sin^2\theta \quad (5.12)$$

$$I_{int}(Q,\theta) = 2\sin\theta\cos\theta\, Re[J_{xy}e^{i\Delta}] \quad (5.13)$$

where $\Delta = \varphi_2 - \varphi_1$ is the initial phase difference. If we normalize J_{xy} to the diagonal element of the coherence matrix, the degree of polarization is:

$$\mu_{xy} = \frac{J_{xy}}{\sqrt{J_{xx}J_{yy}}} = |\mu_{xy}|e^{i\delta} \quad (5.14)$$

$$P = \left\{1 - \frac{4\det(J)}{[tr(J)]^2}\right\}^{1/2} = \left[1 - \frac{4I_xI_y(1-|\mu_{xy}|^2)}{(I_x+I_y)^2}\right]^{1/2} \quad (5.15)$$

where δ is the relative phase between the two orthogonal electrical field components. This can be calculated by detecting the difference in the contrast related to the reference image that only contains the initial difference Δ. The degree of the polarization is $P = |\mu_{xy}|$, if I_x is equal to I_y. the I_{int} is arranged as:

$$I_{int}(Q,\theta) = 2\sin\theta\cos\theta\sqrt{I_x I_y}\left|\mu_{xy}\right|\cos\ (\Delta+\delta) \tag{5.16}$$

If two particular angles of the polarizer were chosen that are at 0° and 45°, the total intensity at 0° will be I_x while that of the 45° will be:

$$I\left(\frac{\pi}{4}\right) = \frac{I_x + I_y}{2} + (I_x I_y)^{1/2}\left|\mu_{xy}\right|\cos\ (\Delta+\delta) \tag{5.17}$$

If the intensity image are obtained at both 0° and π/4, I_x could be known from the image at 0°, so could I_y from the I(π/4). The difference in fringe position compared to the reference image will gives the relative phase difference δ. Therefore, three images are needed to obtain the polarization information. One is recorded as the reference image, to record the initial phase. This is obtained when the input beam is linear polarized with the polarizer at any angle in addition to the 0° and 90°. The other two images are recorded by orientating the polarizer at 0° and 45° respectively. From the intensity of each pixel, the polarization state across the beam can be calculated. The whole data recording process is shown as follows:

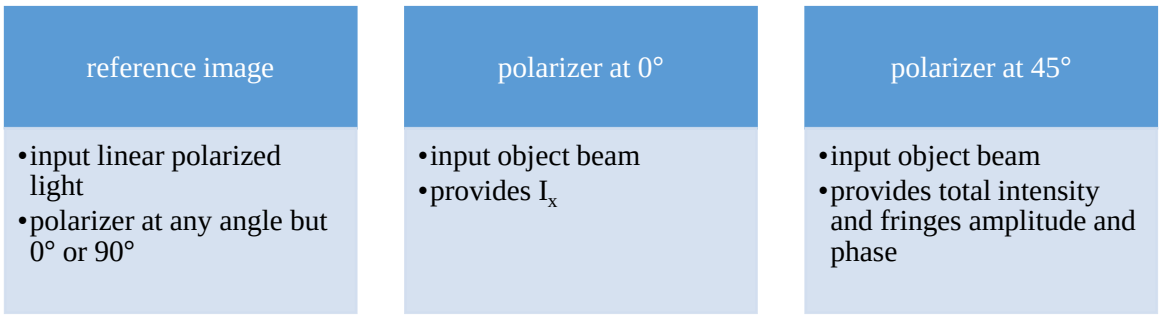


Figure 5. 16: Data recording process and notation.

Algorithm

The first step is to analyse the reference image. The FFT method described in Chapter 3 is used to extract the initial phase from the reference image.

In terms of the image obtained at 0°, the background noise needs to be removed to get the intensity of I_x. Hence, the image is transformed to the frequency domain, passing a low pass filter. Then the new data is transformed back to the spatial domain by inverse Fourier transform.

When analysing the image at 45° and calculating the total intensity, the fringes components are removed and only the low frequency part is left. After transferring back to the spatial domain, the intensity of each pixel represents $(I_x+I_y)/2$ as Eq. (5.17) shows. In this case, the total intensity is obtained.

Next, the amplitude and phase of the interference need to be extracted. When the image is transformed to frequency domain, the position of the 1st order should be the same as in the reference image. By using the 2D FFT method, the amplitude and the phase of the interference can be extracted. A model fringe image was simulated to verify the algorithm. The model image and its corresponding amplitude and phase are shown in Figure 5.17.

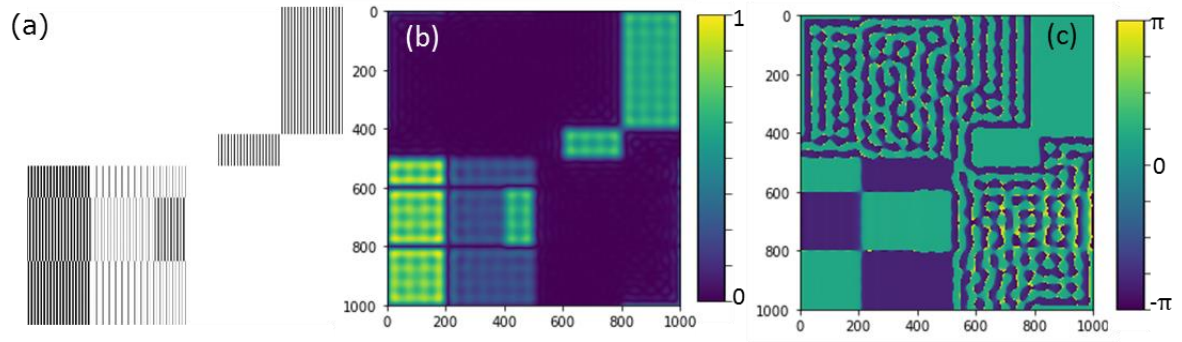


Figure 5. 17: (a) Simulated model image (b) calculated amplitude (c) calculated phase. Note that the phase values in the low amplitude regions have arbitrary values.

The phase extracted from the 45° now contains both Δ and δ. In order to get the related phase difference δ, subtract the initial phase calculated in the reference image. Now, we have all the information needed and the Stokes parameter can be written in the following forms to get the spatial profile of polarization:

$$I = I_x + I_y$$

$$Q = I_x - I_y$$

$$U = 2A\cos\delta$$

$$V = 2A\sin\delta \tag{5.18}$$

where A is the amplitude of the fringe and δ is the phase difference between the E_x and E_y.

Reducing the measurement times

The method to use three images to calculate the polarization state is introduced above. It is rather complex and may slow down the process when integrated on a microscope because it takes time to take images by rotating the polarizer to different angles. Instead of rotating the polarizer, it would be faster to use the SLM system to introduce varied illumination for parallel measurements. In other words, modulating the input light with a static polarizer can make the system robust and response fast. In this case, the polarizer could be fixed at 45° and each time the image obtained is the intensity of $I(\pi/4)$. The derivation below indicates that with some prior information, it might be possible to obtain the polarization state with a single image measurement.

According to Eq. (5.17), If the light is fully polarized and make $|\mu_{xy}| = 1$, $I_x + I_y/2 = A$, and $(I_x I_y)^{1/2} = B$, Eq. (5.17) has the form:

$$I\left(\frac{\pi}{4}\right) = A + B\cos(\Delta + \delta) \tag{5.19}$$

I_x and I_y are solved from Eq. (5.19):

$$I_x = A \pm \sqrt{A^2 - B^2}$$

$$I_y = A \mp \sqrt{A^2 - B^2} \tag{5.20}$$

Now two sets of I_x and I_y are given in Eq. (5.20). The output field can be written as:

$$\overrightarrow{J_{out}}\left(\frac{\pi}{4}\right) = \begin{pmatrix} \sqrt{I_x} \\ \sqrt{I_y}e^{i\delta} \end{pmatrix} \tag{5.21}$$

where δ is the phase difference between the two electrical fields. If $C = \sqrt{A^2 - B^2}$, the output matrix has the form of either J_{out1} or J_{out2}:

$$\overrightarrow{J_{out1}} = \begin{pmatrix} \sqrt{A + C} \\ \sqrt{A - C}e^{i\delta} \end{pmatrix}$$

$$\overrightarrow{J_{out2}} = \begin{pmatrix} \sqrt{A - C} \\ \sqrt{A + C}e^{i\delta} \end{pmatrix} \tag{5.22}$$

It is found that these two matrices have an interesting relation:

$$\overrightarrow{J_{out1}} = \begin{pmatrix} 0 & e^{-i\delta} \\ e^{i\delta} & 0 \end{pmatrix}\overrightarrow{J_{out2}}$$

$$\overrightarrow{J_{out2}} = \begin{pmatrix} 0 & e^{-i\delta} \\ e^{i\delta} & 0 \end{pmatrix}\overrightarrow{J_{out1}} \tag{5.23}$$

Let us assume $\overrightarrow{J_{out1}}$ is the correct output field and there is an unknown object of spatially varying optical elements introduced in the system, so the output field is: $\overrightarrow{J_{out1}} = J_{obj} \times J_{mod} \times \overrightarrow{J_{in}}$. If the object only introduces retardance and no diattenuation or depolarization, J_{obj} will have the correct general form of a linear retarder that is:

$$J_{obj}(\varphi, \theta) = \begin{pmatrix} \cos^2\theta + e^{-i\varphi}\sin^2\theta & \left(1 - e^{-i\varphi}\right)\cos\theta\ \sin\theta \\ \left(1 - e^{-i\varphi}\right)\cos\theta\ \sin\theta & e^{-i\varphi}\cos^2\theta + \sin^2\theta \end{pmatrix} \tag{5.24}$$

where ϕ is the retardance and θ is the angle between the fast axis of the retarder and the propagation direction of the beam. It is noted that the off-diagonal elements are identical. If the correct form of the output field is chosen, an object Jones matrix that has identical off-diagonal

elements can been obtained. According to the relation between $\overrightarrow{J_{out1}}$ and $\overrightarrow{J_{out2}}$, if $\overrightarrow{J_{out2}}$ is chosen as the output:

$$\overrightarrow{J_{out2}} = \begin{pmatrix} 0 & e^{-i\delta} \\ e^{i\delta} & 0 \end{pmatrix} \overrightarrow{J_{out1}} = \begin{pmatrix} 0 & e^{-i\delta} \\ e^{i\delta} & 0 \end{pmatrix} \times J_{obj} \times J_{mod} \times \overrightarrow{J_{in}} = J'_{obj} \times J_{mod} \times \overrightarrow{J_{in}} \quad (5.25)$$

where J'_{obj} has the form:

$$J'_{obj} = \begin{pmatrix} 0 & e^{-i\delta} \\ e^{i\delta} & 0 \end{pmatrix} \times J_{obj}$$

$$= \begin{pmatrix} e^{-i\delta}\left(1 - e^{-i\varphi}\right)\cos\theta\ \sin\theta & e^{-i\delta}(e^{-i\varphi}cos^{\,2}\theta + sin^2\theta) \\ e^{i\delta}(cos^2\theta + e^{-i\varphi}sin^2\theta) & e^{i\delta}\left(1 - e^{-i\varphi}\right)\cos\theta\ \sin\theta \end{pmatrix} \quad (5.26)$$

Here, the off-diagonal elements are no longer identical. This provides a way to judge if the correct form of the output field is selected. By using this mathematical observation, it is possible to obtain the correct result using only one image.

5.2.2 Stokes polarimeter

Another polarimeter with simple configuration is the Stokes polarimeter. The polarimeter can calculate the Stokes parameters across the beam based on the intensity of the images captured using the four different fast axis orientations of the QWP. The general configuration of a polarimeter is shown in Figure 5.18. The polarizer transmission axis is fixed to be horizontal. The fast axis orientation of the QWP in an optimized Stokes polarimeter are 15.1°, 51.7°, 128.3°, and 164.9° respectively. These angles are optimized to accurately calculate the polarization state in Ref [128].

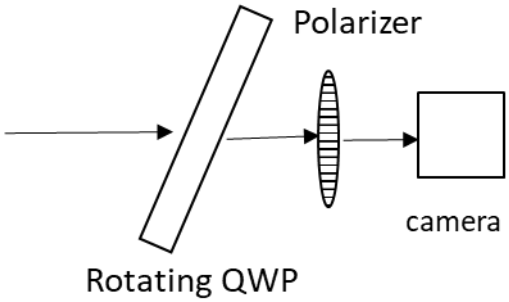


Figure 5. 18: Basic configuration of a Stokes polarimeter.

The Stokes parameters were then calculated as:

$$\vec{S}_{out} = A^{-1}\vec{I} \tag{5.27}$$

where A is a 4×4 matrix. Each row in A is the first row of the Müller multiplication of the polarizer and the QWP, $M_pM_{QWP}(\theta)$, where M_p is the Müller matrix of the linear polarizer, whose fast axis was fixed to be horizontal; $M_{QWP}(\theta)$ is the Müller matrix of the QWP, with the fast axis orientation of θ. Matrix A can be determined when substituting θ = 15.1°, 51.7°, 128.3°, and 164.9° respectively. The intensities obtained at each fast axis orientation θ were recorded in sequence and forms a 4×1 vector I. Then, the output Stokes parameters can be calculated using Eq. (5.27). This is referred to as one PSA measurement.

The Stokes polarimeter was then tested by using 45° polarized input light, the intensity images recorded by the camera are shown in Figure 5.19, and the calculated Stokes parameters using Eq. (5.27) are shown in Figure 5.20. It can be seen that the calculated Stokes parameters S_1, S_2 and S_3 are around $[0, 1, 0]^T$ as expected.

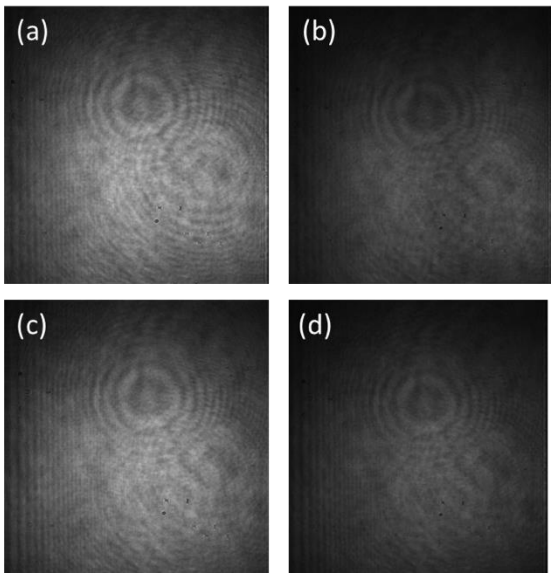


Figure 5. 19: Intensity image recorded by camera at different QWP fast axis orientation. (a) 15.1° (b) 51.7° (c) 128.3° (d) 164.9°

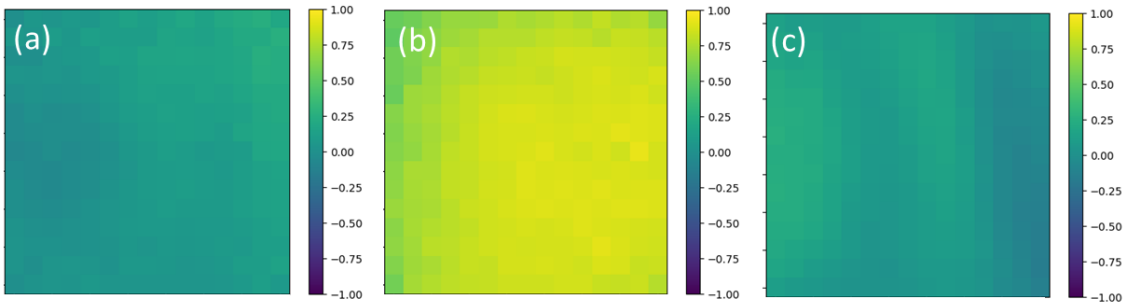


Figure 5. 20: Stokes parameters calculated (a) S_1 (b) S_2 (c) S_3, theoretical Stokes parameters of 45° polarized light is $[S_1, S_2, S_3]^T = [0, 1, 0]^T$

5.3 Comparison and conclusion

One polarimeter solution needs to be chosen as the PSA in the APC system. The modified Sagnac interferometer is stable and requires less measurements, with one reference measurement when the system was built up. Two extra measurements are needed when analysing the polarization state of different output light. However, it also has some drawbacks.

5.3 Comparison and conclusion

First, the interferometer is not able to measure polarization states that are near to either *x* or *y* polarized because no fringes would be detected. In addition, if the light is -45° polarized, image recorded at polarizer transmission axis at 45° would also have lower intensity, as shown in Figure 5.21 (a). The lower fringe contrast therefore decreased the measurement accuracy.

Besides, the optical elements in the polarimeter also introduces some aberrations. In the polarization correction system, the aberration introduced by the system should be as lower as possible. The PBS and the two lenses in the Sagnac interferometer introduce some aberrations.

In addition, since the interferometer requires separating the two beams and then superposition them, if the superposition is perfect, the accuracy of the calculated polarization state is also compromised. As shown in Figure 5.21 (b), in reality, it was difficult to superpose the two beams perfectly.

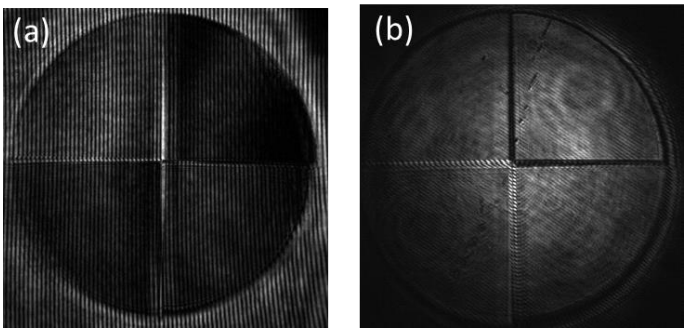


Figure 5. 21: (a) Interferogram recorded if the beam is nearly -45° polarized. The low intensity decreases the accuracy to calculate the polarization state. (b) Two beams after the PBS was hard to be superposed perfectly.

Although the Stokes polarimeter requires two more measurements, the configuration is simple and the calculation method is straightforward compared to the Sagnac interferometer. Lower aberrations and calculation noise were observed. For reasons of practical implementation and lower system errors, the Stokes polarimeter was chosen, although other solutions may be preferable in applications where speed is important.

5.3 Comparison and conclusion

It is clear that slight misalignments of the SLM in the system can cause problematic errors in the output polarization state. Therefore, the whole system should be calibrated carefully. It was realized by accessing all combinations of PGV both on first pass and second pass to find the mapping between the PSG and PSA. First, the first pass PGV was changed from 0 to 150 and the second pass PGV was fixed to 0; the Stokes parameters were recorded by the PSA accordingly. Then the second pass PGV increased by 1 and changed the first pass PGV again from 0 to 150; the output Stokes parameters were recorded again. Therefore, a mapping between the different PGV on the dual pass and the corresponding Stokes parameters is obtained. If one would like to generate a specific polarization state, searching on the nearest Stokes parameters and the PGV applied on the SLM could be obtained.

Chapter 6 Adaptive Polarization Control

In this chapter, an adaptive polarization control (APC) system is introduced, encompassing both hardware and algorithms, which allow us to control the output polarization profile of a beam, even when disturbed by a specimen. The APC system consists of two hardware modules, which introduced in last chapter: a PSG, in the form of a dual pass liquid crystal SLM, and a PSA, comprising a rotating waveplate based imaging Stokes polarimeter. The APC system can extract the birefringence profile of a specimen and then adaptively manipulate the output polarization state through control of the input beam using the PSG.

The operation is described in terms of Jones calculus. As the Jones matrix of an unknown birefringence cannot be determined unambiguously through a single polarimeter measurement in the APC system, different strategies are investigated that can be employed depending upon the amount of prior information one has about the specimen. Through the assumption that the specimen is purely birefringent and introduces no diattenuation, it is found that between one and three PSA measurements are required, dependent upon the knowledge of the specimen. Four kinds of samples are demonstrated for system validation: a vortex half wave retarder, a stressed plastic plate, a customized liquid crystal device and excised mouse brain tissue. In each case how the polarized component of the output light can be restored through feedback correction to the desired state is shown, despite the disturbance.

6.1 Methodology

The schematic basis of the system is shown in Figure 6.1. The purpose of the system is to generate a desired polarization state at the output, even when an unknown birefringent disturbance is introduced by an object. Compensation for the disturbance is implemented by producing the input the necessary polarization state using the PSG at the input. A sequence of measurements is taken by the PSA, the number of which depends on the degree of prior information that is known about the disturbance. Using these measurements, the polarizing characteristics of the object are determined and the necessary input state is generated.

The theoretical model is based on the scheme shown in Figure 6.1. According to Jones calculus, the polarization of the output light is represented as Eq. (6.1), assuming there is no loss and attenuation during beam propagation:

$$\overrightarrow{J_{out}} = J_{sample}\,\overrightarrow{J'_{mod}} \tag{6.1}$$

where $\overrightarrow{J_{out}}$ is the normalized Jones vector of the output light. J_{sample} is the Jones matrix of the birefringent disturbance and $\overrightarrow{J'_{mod}} = J_{mod} \times \overrightarrow{J_{in}}$ is the Jones vector of the modulated input light, which is created by the PSG and will be discussed in next section. In all cases presented here, the quantities are functions of the spatial coordinates across the beam profile. For brevity, the explicit dependence on these coordinates is omitted from the notation. For the normalized Jones vector, the absolute phase is removed and retardance information is kept, which is sufficient for our analysis of polarization; hence, the vector represents the polarization state in terms of the amplitude ratio and retardance between the electric field components E_x and E_y. The aim of the system is to obtain a specified $\overrightarrow{J_{out}}$ in the presence of an unknown J_{sample}. As $\overrightarrow{J'_{mod}}$ can be controlled, output measurements can be obtained using different input polarizations in order

to determine the unknown J_{sample}. According to Chapter 2, the Jones matrix of an arbitrary birefringent material could be simplified as:

$$J_{sample} = \begin{bmatrix} \cos^2\theta + e^{i\phi}\sin^2\theta & (1-e^{i\phi})e^{-i\eta}\cos\theta\sin\theta \\ (1-e^{i\phi})e^{i\eta}\cos\theta\sin\theta & \sin^2\theta + e^{i\phi}\cos^2\theta \end{bmatrix} \tag{6.2}$$

where θ is the fast axis orientation with respect to the x-axis, ϕ is the retardance between E_x and E_y, and η is the circularity. Therefore, as a minimum three measurements are needed to be taken to obtain the matrix. If η = 0, e.g. for linear retarders [129], the unknown variables are reduced to two. Further, if the prior knowledge of the magnitude of the retardance of the disturbance is known, only one measurement is sufficient. Hence, in different situations where having different prior knowledge of the disturbance, different settings of $\overrightarrow{J'_{mod}}$ can be applied to measure the corresponding $\overrightarrow{J_{out}}$. The Jones matrix of the sample can be calculated according to Eq. (6.1). After the J_{sample} is obtained, the $\overrightarrow{J'_{mod}}$ can be calculated for each desired output polarization state $\overrightarrow{J_{out}}$. The PSG is then used to generate the corresponding $\overrightarrow{J'_{mod}}$.

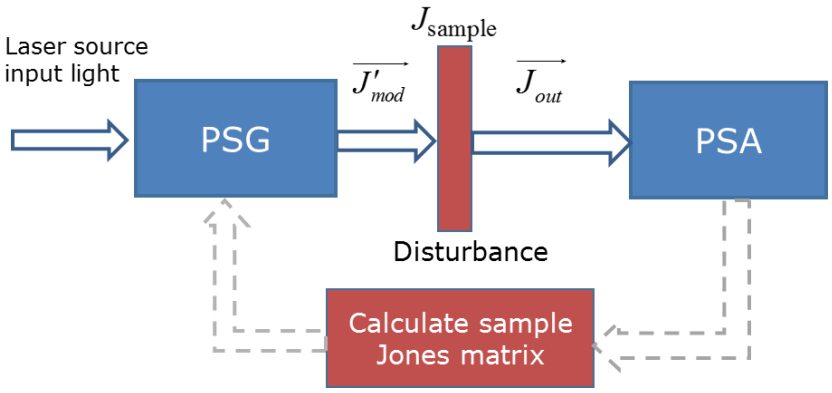


Figure 6. 1: Principle of the APC system operation. Blue solid line: beam propagation direction; grey dashed line: calculation path.

6.2 Experiment set-up

A schematic of the APC system is shown in Figure 6.2. The input light comes from the laser source (Coherent Cube L94160801, 786 nm, 40 mW). The PSG used a dual-pass system on the SLM (LCOS-SLM Hamamatsu, X10468−02), which was able to generate any spatially variant polarization state. The PSA was able to calculate the polarization state of the output light by rotating the QWP to four different angles and recording the intensity profile of the beam. The disturbing sample was placed between the PSG and PSA. The sample was conjugated using 4f systems to the SLM in the PSG and the CMOS camera in the PSA.

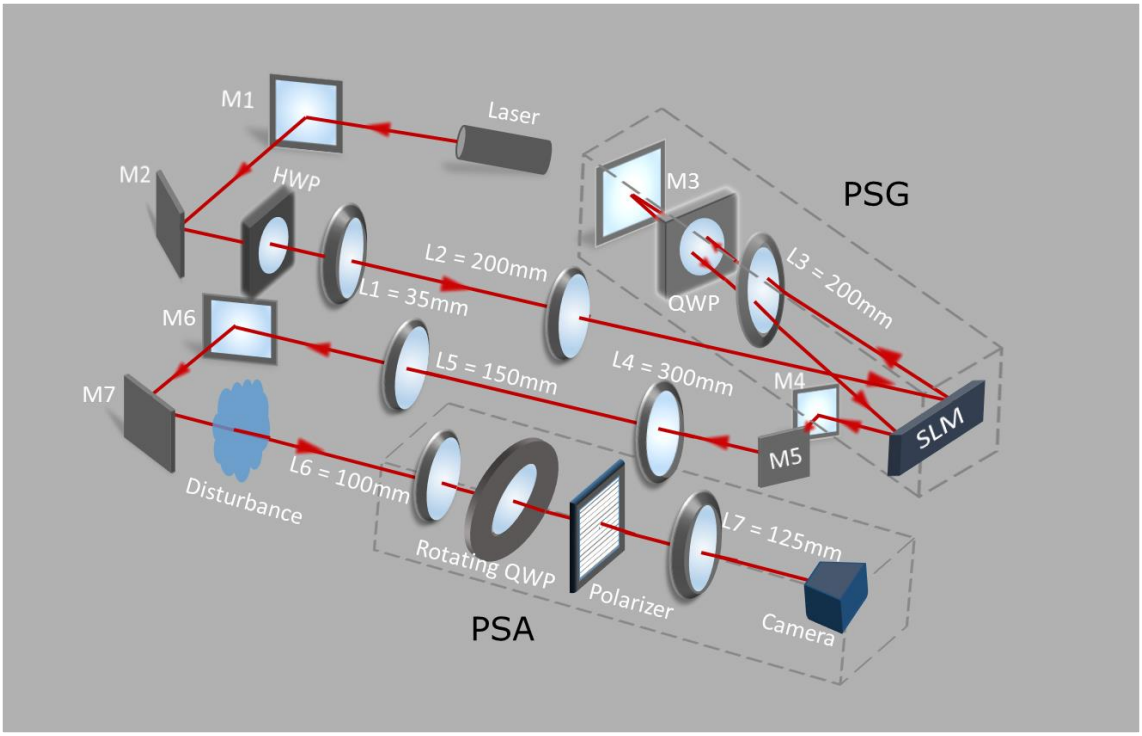


Figure 6. 2: Schematic of the experimental setup of the APC system. PSG and PSA are labeled in the dashed line. M1 to M7: mirrors. HWP: half wave plate with fast axis at 22.5°. L1 to L7: lens. SLM: spatial light modulator. QWP: quarter wave plate with fast axis at 22.5°. Fast axis of the polarizer was fixed to be horizontal and of the rotating QWP were at 15.1°, 51.7°, 128.3°, and 164.9° respectively when measuring the polarization state [128].

As mentioned in the last chapter, after the PSG, the output light has Jones vector of:

$$\overrightarrow{J_{out}} = \begin{bmatrix} \sin\frac{\delta_1}{2}\, e^{\frac{\pi-\delta_2}{2}} \\ \cos\frac{\delta_1}{2}\, e^{\frac{\delta_2}{2}} \end{bmatrix} \tag{6.3}$$

It is seen that the amplitude ratio between E_x and E_y is decided by δ_1, the first SLM pass retardance, and the phase shift between E_x and E_y is determined by the second pass retardance δ_2. Therefore, assuming δ_1 and δ_2 can take any value between 0 and 2π radians, the polarization of the output light can be manipulated to any state by using the dual-pass SLM system.

Using the PSA, the polarization could be determined by a sequence of four measurements. As it is concerned here with restoring the desired polarization state through birefringence transformations, the implicit assumption is using fully polarized light. Then convert the Stokes vectors to the corresponding normalized Jones vectors [130], as in Eq. (6.1), which describe only the polarized component of the beam. The detailed conversion method is shown in the Appendix. Due to the nature of Müller polarimetry, it is not possible to retrieve the overall phase of the beam.

6.3 Results and Discussion

This APC system can be controlled in different ways depending on what prior assumptions can be made about the specimen's birefringent properties. In order to illustrate this, four different kinds of samples are demonstrated here, each of which required different numbers of measurements for analysis.

6.3.1 Vortex half wave retarder

The first sample was a vortex half wave retarder (Thorlabs, WPV10L-780). This consists of a spatially variant half wave plate, whose retardance value is fixed, but whose fast axis is distributed as shown in Figure 6.3(a). Figure 6.3(b) shows the expected fast axis distribution of the HWR and the intensity profile created when the device is place between crossed polarizers. This provides us a reference object to test the system and calculation algorithm.

According to Eq. (6.2), if the retardance of the phase retarder is known to be π radians, the Jones matrix of the vortex half wave retarder can be simplified as

$$J_{sample} = \begin{bmatrix} \cos^2\theta - \sin^2\theta & 2\cos\theta\sin\theta \\ 2\cos\theta\sin\theta & \sin^2\theta - \cos^2\theta \end{bmatrix} \tag{6.4}$$

Hence, only one measurement is need to get the value of θ modulo π radians. Set the PSG to generate horizontal polarized input light, e.g. $\overrightarrow{J'_{mod}} = \begin{bmatrix} 1 & 0 \end{bmatrix}^T$. The output Jones vector using this illumination is therefore:

$$\overrightarrow{J_{out}} = J_{sample}\overrightarrow{J'_{mod}} = \begin{bmatrix} \cos^2\theta - \sin^2\theta & 2\cos\theta\sin\theta \\ 2\cos\theta\sin\theta & \sin^2\theta - \cos^2\theta \end{bmatrix}\begin{bmatrix} 1 \\ 0 \end{bmatrix} = \begin{bmatrix} 2\cos 2\theta \\ \sin 2\theta \end{bmatrix} \tag{6.5}$$

By using the PSA and converting the measured Stokes parameters to Jones vectors, θ can be calculated. After the sample Jones matrix was determined, given the desired output polarization state, $\overrightarrow{J'_{mod}}$ can be worked out by:

$$\overrightarrow{J'_{mod}} = J^{-1}_{sample}\overrightarrow{J_{d_out}} \tag{6.6}$$

where $\overrightarrow{J_{d_out}}$ is the Jones vector of the desired output light. If one wants to restore the light to still be horizontal polarized after the sample disturbance, $\overrightarrow{J'_{mod}}$ can be calculated and the corresponding voltage on the SLM can ensure the necessary input polarization.

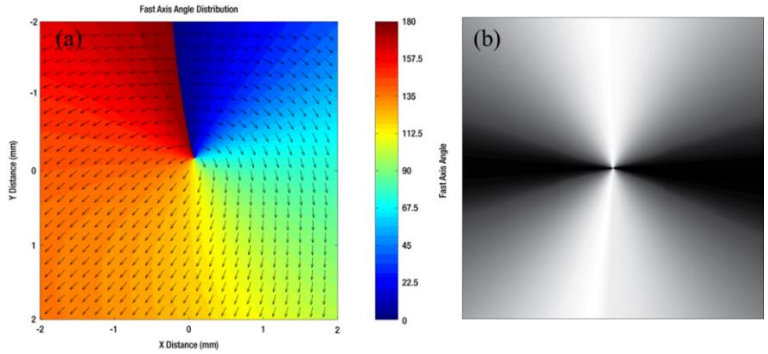


Figure 6. 3: (a) Fast axis angle distribution of the HWR. (b) The intensity profile when viewed between crossed polarizers. Image provided by Thorlabs. [131]

To simplify the calibration process, as the SLM properties are expected to vary only slowly across its profile, the SLM is considered as a combination of 20×20 pixel sub-regions. This also helped reduce the intensity noise and calculation time. Here, the region used on half of the SLM was set to be 300×300 pixels which encompassed 15×15 sub-regions. Thereafter, according to the magnification relation, the output light region could map to the SLM region. Figure 6.4 (a) – (c) shows the calculated Stokes parameters calculated after using −45° linear polarized illumination light.

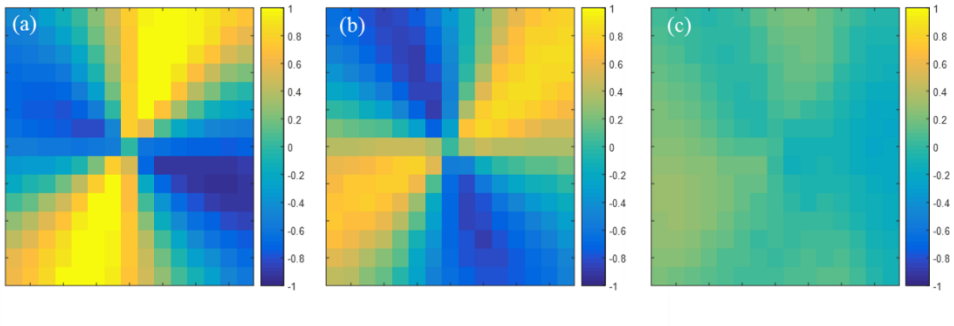


Figure 6. 4: Stokes parameters calculated from the polarimeter measurements of the output light after using −45° linear polarized light incident onto the vortex HWR. (a) S_1 (b) S_2 (c) S_3. S_1, S_2 and S_3 are all normalized between -1 to 1. The measurements show the expected distribution corresponding to a radially polarized light field.

Since the input light is −45° linear polarized, whatever the fast axis is of the HWR, the output light should be all linear polarized. It means the Stokes component S_3 should be all 0 across the whole plane. In Figure 6.4 (c), it can been seen that S_3 is close to the theoretical value across the whole beam. The small deviations can be due to a variety of reasons, including non-ideal operation of the PSG or PSA that the sample does not have an exact retardance of π radians at the wavelength of 780 nm.

After obtaining the orientation of the fast axis, it was possible to return the output light to the desired state by using the method described above. In this case, to restore the light to uniform horizontal polarization is the target. Figure 6.5 compares the intensity distribution and of the final output light before and after correction viewed through different fast angles of the QWP. Just two of the four angles have been chosen for the purposes of illustration. Also shown is the output light polarization ellipse orientation (or equivalently, the orientation of polarization if linearly polarized) before and after correction.

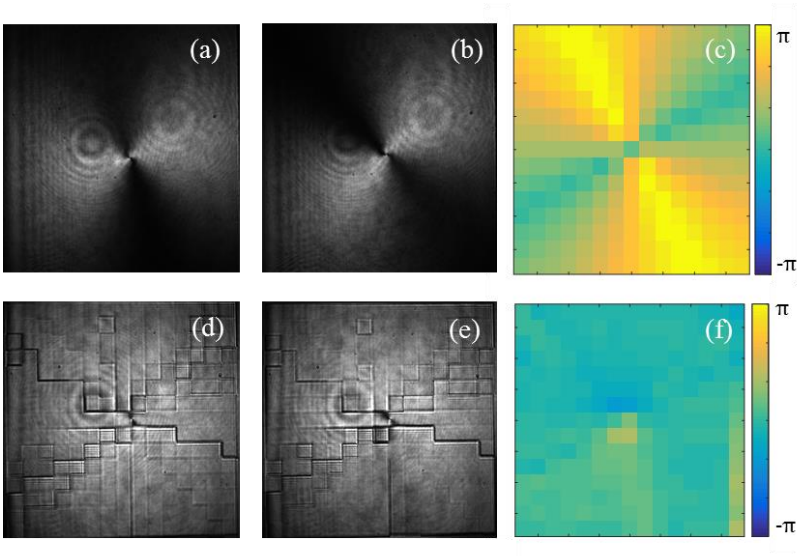


Figure 6. 5: (a) The intensity distribution detected by the camera before polarization correction using a fast axis angle of 15.1° for the QWP (b) with 164.9° fast axis angle (c) corresponding orientation of the polarization state of the output light before correction, showing a near-radially polarized beam. (d) The intensity distribution after the QWP with 15.1° fast axis angle, when using the customized polarized beam to incident on the vortex HWR to restore the output to horizontal polarization. (e) with 164.9° fast axis angle (f) orientation of the polarization state of the output light after correction, showing near-zero angles across the beam.

It can be seen that the intensity profile and the orientation of the polarization state look more uniform after correction, showing that the compensation has succeeded. The square patterns arise due to diffraction effects at the edges of the grid of 15×15 correction sub-regions on the SLM.

The residual errors might be due to several reasons. As the calibration of the SLM was based on 20×20 pixel sub-regions, there may be non-uniformity across a sub-region and there can be sudden spatial transitions between liquid crystal states at the edges of the sub-regions. One could expect a reduction in these effects by reducing the size of the sub-region and increasing the calculation time and complexity. There will be a tradeoff between the calibration region size and retrieval accuracy and at the lower size. The performance would be limited by the cross-talk between adjacent pixels due to the liquid crystal properties.

Next, the APC system was tested for reconstructing the output light to an arbitrarily chosen uniform polarization state. The target reconstructions for the output light were chosen to be horizontal, 45° linear and right circular polarized, respectively. Figure 6.6 shows the Stokes parameters S_1, S_2 and S_3 of the output under different reconstructing situations, as retrieved by the PSA. It is seen that the APC system is able to manipulate the polarization state as expected.

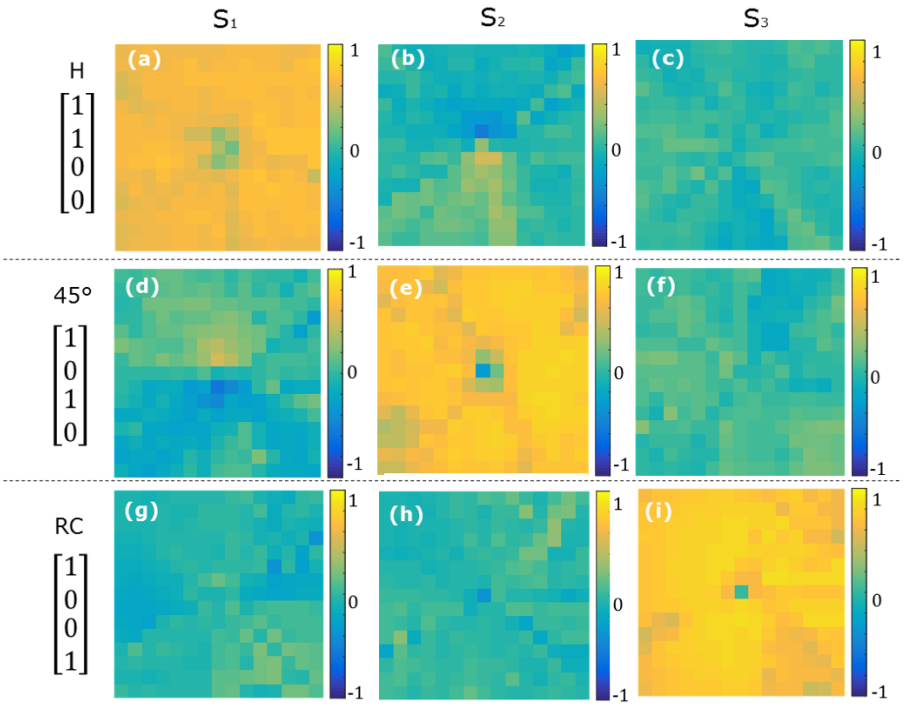


Figure 6. 6: Stokes parameters measured by the PSA under different reconstructing situations. (a) – (c): S_1, S_2 and S_3 for horizontally polarized output. (d) – (f): Stokes parameters for 45° linearly polarized output. (g) – (i): Stokes parameters for right circular polarized output

6.3.2 Stressed plastic plate

Stressed polycarbonate is a biaxial birefringent material, whose in-plane and lateral refractive indices are different [132, 133]. The difference in the refractive index would introduce a retardance depending on the orientation of the optical axis of the plastic substrate. A stressed plastic plate was then tested whose both retardance and fast axis orientation were unknown to

demonstrate our system. The birefringent effect of the plastic plate sample viewed through crossed polarizers is shown in Figure 6.7 (a).

If the retardance and fast axis orientation are unknown, the Jones matrix of the sample can be represented as:

$$J_{sample} = \begin{bmatrix} \cos^2\theta + e^{i\phi}\sin^2\theta & (1-e^{i\phi})\cos\theta\sin\theta \\ (1-e^{i\phi})\cos\theta\sin\theta & \sin^2\theta + e^{i\phi}\cos^2\theta \end{bmatrix} \tag{6.7}$$

It is seen that the off-diagonal elements are equal. This observation can be used to extract the Jones matrix of the sample using two PSA measurements, with horizontally and vertically polarized illumination. The Jones vectors after using horizontal and vertical illumination are:

$$\overrightarrow{J_{out1}} = J_{sample}\overrightarrow{J'_{mod1}} = \begin{bmatrix} A & B \\ B & C \end{bmatrix}\begin{bmatrix} 1 \\ 0 \end{bmatrix} = \begin{bmatrix} A \\ B \end{bmatrix} = \alpha_1 \begin{bmatrix} A_1 \\ B_1 \end{bmatrix} \tag{6.8}$$

$$\overrightarrow{J_{out2}} = J_{sample}\overrightarrow{J'_{mod2}} = \begin{bmatrix} A & B \\ B & C \end{bmatrix}\begin{bmatrix} 0 \\ 1 \end{bmatrix} = \begin{bmatrix} B \\ C \end{bmatrix} = \alpha_2 \begin{bmatrix} B_2 \\ C_2 \end{bmatrix} \tag{6.9}$$

where *A*, *B* and *C* are all complex numbers in the sample Jones matrix. A_1, B_1 are the elements of the (normalized) Jones vector calculated from the conversion of Stokes parameters from the PSA of the first measurement, and α_1 is the scaling factor to the original matrix element. Similarly, α_2 is the equivalent factor for the second measurement. Since it is known that the two off-diagonal elements are the same, the relationship between the scaling factor α_1 and α_2 can be easily calculated and the normalized Jones matrix of the sample determined. Eq. (6.6) can then be used to determine the necessary input light field to produce the desired output.

Figure 6.7 (b) shows plots of the polarization ellipse of each sub-region before correction when using vertical polarized light to illuminate the plastic plate. The output polarization state is non-uniformly distributed across the pupil because of the uneven birefringence. Figure 6.7 (c) − (e)

show the polarization ellipses under different reconstruction situations by using the APC system. It is seen that the system is able to reconstruct across most of the field the output polarization state, even with an unknown retardance and fast axis orientation of the disturbance. The mismatch of a few regions in Figure 6.7 (d) and (e) is because those sub-regions are areas of rapidly changing birefringence, which can be seen from the inset aperture of the illumination region from Figure 6.7 (a). Since the intensity was averaged in PSA when calculating the Jones matrix for each sub-region, there could still be mismatches in correction in such regions.

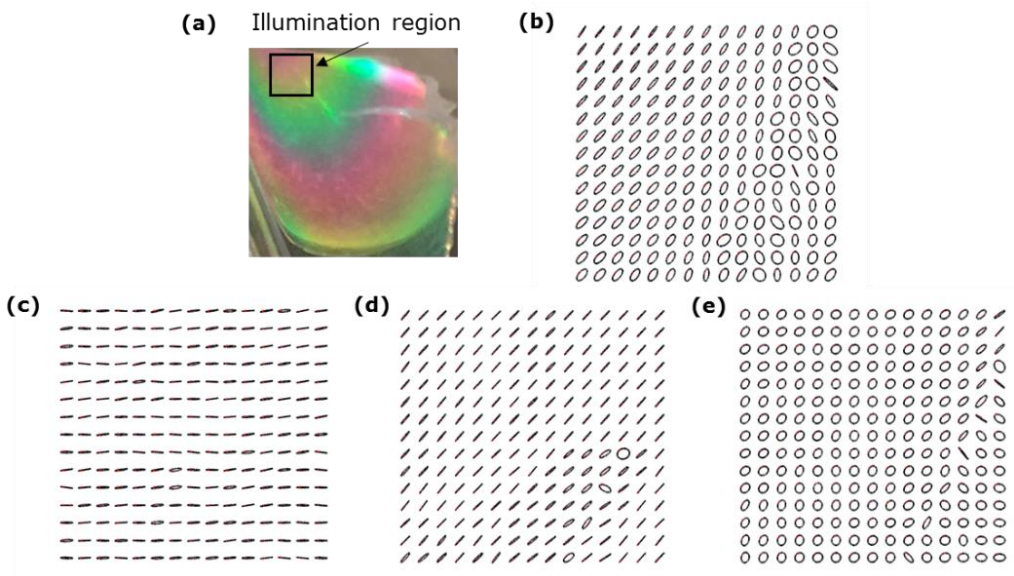


Figure 6. 7: (a) Birefringent effects of a stressed plastic plate illuminated by a lamp when viewed through cross polarizers with white light illumination. (b) Plotted polarization ellipse of the output before correction when using vertical polarized illumination. (c) Polarization ellipse under horizontal polarization state reconstruction (d) Polarization ellipse under 45° linear polarization state reconstruction. (e) Plotted polarization ellipse of the output light under right circular polarization state reconstruction.

6.3.3 Liquid crystal device

A liquid crystal (LC) device was used to show how the APC could adapt to changes in a dynamic system. This LC device was a 20 µm thick anti-parallel rubbed cell (Instec Inc). It had

a 5×5 mm electrode region and was filled with E7 liquid crystal. The liquid crystal device was connected to a signal generator and placed it at the sample plane. The device was designed to have two different regions, which is refered to as the static region and the dynamic region. The birefringence in the static region, which was away from the electrode structure, did not vary with the external voltage, denoted *U*, while the dynamic region, in the vicinity of the electrodes, changed with a varying drive voltage. The schematic of the device is shown in Figure 6.8 (a). The system's dynamic functionality was tested by changing the voltage to the device and to see if APC could react to the different birefringence disturbance and reconstruct to the same polarization state.

Figure 6.8 (b) − (e) shows the measurements represented on a Poincaré Sphere when the sample was illuminated with a horizontally polarized light. Figure 6.8 (b) shows the output polarization state at different sub-regions (one point corresponds to one sub region) before correction when the drive voltage U = 1.8 volts. The output polarization state of the static and dynamic regions were distributed away from the desired horizontal polarization state because of the spatially varying birefringent disturbance introduced by the LC cell. After applying correction using the APC system, the polarization state became more uniform and concentrated to the horizontal polarization state as shown in Figure 6.8 (c). Figure 6.8 (d) plots the output polarization state without APC compensation when the drive voltage was set to U = 2.5 volts. It can be seen that the polarization state of the reference region is similar to the equivalent measurements shown in part (b); due to the birefringence change in the dynamic region, the polarization state of that region had a different distribution. Despite the disturbance change, after APC correction the polarization of the output light still could be reconstructed to the uniform horizontal polarization as shown in Figure 6.8 (e). With this customized sample, the APC is demonstrated to be able to track dynamically changing disturbances.

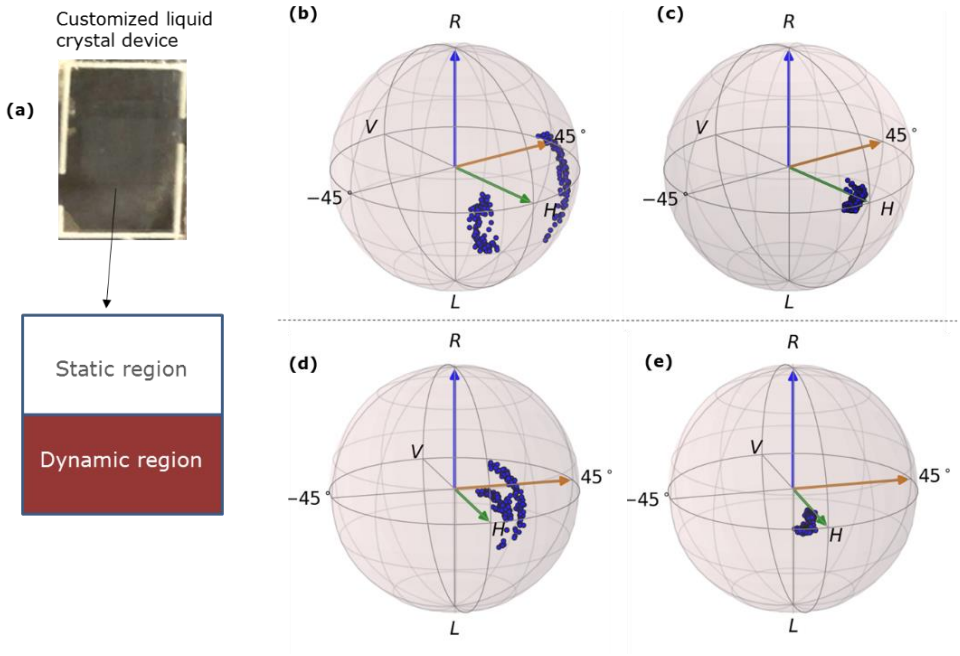


Figure 6. 8: (a) Schematic of the liquid crystal device, the birefringence of the dynamic region can be changed according to drive voltage while the static region does not. (b) Output light polarization state of each sub-region representing on Poincaré Sphere before correction, at U = 1.8 volts. (c) Polarization state distribution after correction at U = 1.8 volts. (d) Polarization state distribution before correction at U = 2.5 volts. (e) Polarization state distribution after correction at U = 2.5 volts.

6.3.4 Mouse brain tissue

The system was also demonstrated in a more general scenario, where no assumptions were made about the nature of the birefringent effects. When the disturbance is an arbitrary birefringent material showing zero diattenuation, according to Eq. (6.1), three measurements are needed to reconstruct the polarization state. The operation of the APC system in this regime was then tested using a sample of mouse brain tissue [134, 135]. A thin tissue sample was used here to ensure minimal light loss and attenuation introduced from the sample. The sample was a 60-μm thick fixed coronal brain slice from a Thy1-GFP line M mouse. A transmission microscope image of the tissue is provided in Figure 6.9 (a).

According to Eq. (6.2), to measure the sample Jones matrix, three independent measurements need to be taken; this is implemented by controlling the PSG to generate horizontal, vertical and 45° linearly polarized illumination light, respectively. The output Jones vectors then can be represented as:

$$\overrightarrow{J_{out1}} = J_{sample}\overrightarrow{J'_{mod1}} = \begin{bmatrix} A & B \\ C & D \end{bmatrix}\begin{bmatrix} 1 \\ 0 \end{bmatrix} = \begin{bmatrix} A \\ B \end{bmatrix} = \alpha_1 \begin{bmatrix} A_1 \\ B_1 \end{bmatrix} \tag{6.10}$$

$$\overrightarrow{J_{out2}} = J_{sample}\overrightarrow{J'_{mod2}} = \begin{bmatrix} A & B \\ C & D \end{bmatrix}\begin{bmatrix} 0 \\ 1 \end{bmatrix} = \begin{bmatrix} C \\ D \end{bmatrix} = \alpha_2 \begin{bmatrix} C_2 \\ D_2 \end{bmatrix} \tag{6.11}$$

$$\overrightarrow{J_{out3}} = J_{sample}\overrightarrow{J'_{mod3}} = \begin{bmatrix} A & B \\ C & D \end{bmatrix}\begin{bmatrix} 1 \\ 1 \end{bmatrix} = \begin{bmatrix} A+B \\ C+D \end{bmatrix} = \alpha_3 \begin{bmatrix} \alpha_1\left(A_1+B_1\right) \\ \alpha_2\left(C_2+D_2\right) \end{bmatrix} \tag{6.12}$$

where A, B, C and D are complex elements of the sample's Jones matrix; A_1, B_1, C_1 and D_1 are normalized output Jones vector elements; α_1, α_2 and α_3 are scaling factors between the matrix elements and normalized output Jones vectors. A and B are first determined using the horizontal polarized illumination. The sample normalized Jones matrix can be determined if the relationship between α_1 and α_2 is found in Eq. (6.10) and (6.11). This can be worked out by having the additional measurement, Eq. (6.12).

A control measurement was performed using an empty region of the microscope slide adjacent to the brain tissue; this showed negligible birefringence effects, where the RMS variation of the Stokes parameters were all less than 0.01. Figure 6.9 (b) and (c) show, as examples, the intensity images of the recorded by the camera when using horizontally polarized light illumination, with the QWP oriented to 128.3° before and after restoration to horizontal polarization, respectively. It can be seen from the uneven intensity distribution before compensation and the more uniform intensity after compensation that the brain tissue introduced a disturbance through birefringence. Figure 6.9 (d) − (f) give the Stokes parameters of S_1, S_2 and S_3 calculated from the PSA before compensation. The variance across the sample

in S_1, S_2 and S_3 was then corrected by the APC after the restoration as shown in Figure 6.9 (g) − (i). These results demonstrate the functionality of this system using three measurements to compensate for an arbitrary birefringent sample.

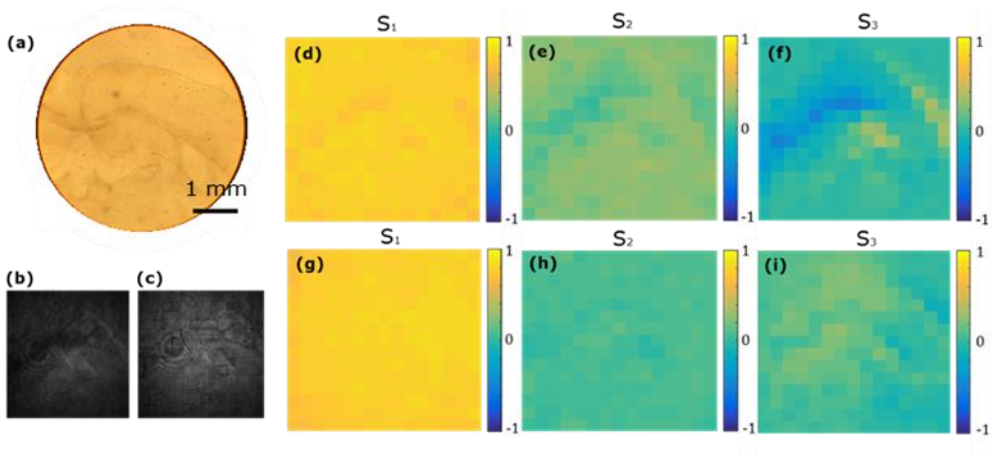


Figure 6. 9: (a) Microscope image of the mouse brain tissue sample. (b) Intensity image recorded by the camera of the brain tissue sample before correction at the rotating QWP of 128.3°. (c) Intensity image of the sample after correction. (d) − (f) S_1, S_2 and S_3 of the polarization state after the brain tissue when using horizontal polarized illumination before correction. (g) − (i) S_1, S_2 and S_3 of the polarization state following correction.

6.4 Summary

In this chapter, the APC system designed to reconstruct the polarization state when there is a birefringent disturbance in the system has been described. Through implementation of the APC, it is shown how an external complex disturbance of the polarization profile across a beam can be corrected using appropriate feedback from the PSA to the PSG. By using different samples with different birefringent features, it is seen that the APC system allows us to restore the polarization state dynamically. In principle, for non-diattenuating specimens, there are three unknowns in the Jones matrix, and hence three independent measurements of the output Jones vector are required. If unknown diattenuation were also present, then more measurements

would be required to determine the optical properties of the specimen. The speed of the correction depends on the measurements needed from the PSA. If only one is required, it can complete the correction within 30 seconds.

With different kinds of samples representing different cases, the APC system has been tested to be able to reconstruct the polarization state as expected. Thus, the adaptive optics on polarization control has been demonstrated to be possible and realisable.

Chapter 7 Conclusion and Outlook

7.1 Conclusion

Adaptive optics has been studied broadly to improve the optical imaging system performance. It helps to correct aberrations and reconstruct the wavefront through the correction elements like deformable mirror and spatial light modulator. Each device has limitations on the correction ability e.g. correction range and accuracy. Besides, most AO research has concerned with only phase aberration correction, whereas polarization errors are also important such as in imaging microscopes and in systems with birefringent disturbances. Therefore, in this thesis, the investigation on the capability of a DM is first provided, and then the idea and implementation of adaptive optics in polarization correction is proposed.

The DM is characterized by building up an interferometer and measuring its phase change through a phase extraction algorithm. The DM generated different aberrated wavefronts (Zernike modes), and compared it with the ideal phase. The experiments set here demonstrated the essence and ability to characterize a DM. It could be made more compact to be accessible within an optical system. For example, a similar method has been implemented in a compact system for insertion into adaptive microscopes developed in our group and helps to calibrate the DM *in-situ*.

Considering the polarization aberration, the adaptive polarization control system (APC) is then developed. Similar to AO system for phase correction, the APC was designed with a

polarization state generator and polarization state analyser, to benefit the system that would have external polarization disturbance. The SLM used in PSG needs prior calibration. So a calibration method is provided in this thesis to calibrate the SLM both for phase and polarization modulation.

The demonstrations of APC presented here illustrate possibilities for implementation in different practical scenarios. The number of measurements required in practice depends upon the assumptions one can make about the specimen, where knowledge about, for example, the retardance or orientation of the birefringence can be used. Using such prior knowledge would help increase the speed of operation of the APC system. The current implementation uses sequential measurements with four positions of the rotating waveplate in the PSA for each Stokes vector measurement. If speed was of the essence, then it would be possible to employ other forms of imaging polarimeter for single shot measurement.

In summary, the work has opened for a possibility AO polarization control in the future where the results on the APC could also benefit other related areas e.g. polarization imaging.

7.2 Outlook

In this section, the limitation, the improvements and potential applications on the methods described throughout the thesis will be discussed.

The algorithm used to extract phase in the interferometer built for DM characterization and SLM calibration would introduce some errors when selecting the Fourier mask manually during the FFT. Therefore, other phase extraction techniques could be alternatives, such as phase shifting, if the system size is not a major concern. Since the light only passes once on the SLM during calibration, one needs to recalibrate the APC system since a dual-pass system

was used and the polarization modulation would change when light is incident on the SLM with a different angle. Hence, the calibration process could be optimized in the future to consider to the angle used in the dual-pass system.

The algorithms designed for APC could also be used to characterize the birefringent feature of a sample. Therefore, it has potential for biological applications e.g. cancer identification and monitoring. The APC is an integrated closed-loop system that extract the sample feature and reconstruct the polarization at the same time. It is ideal to compensate the polarization errors brought by the unknown external birefringent disturbance. If the sample also introduces some diattenuation or depolarization, the algorithm needs to be improved by using Müller matrix instead of Jones matrix calculation. Hence, more measurements are required from the polarimeter. A single shot based polarimeter is needed of the PSA to speed up the whole process.

The work has potential for further studies. Some proposed directions are listed below:

Polarization correction applied in super resolution microscopy:

STED microscopy relies fundamentally on having a depletion beam that is ring shaped with a zero intensity in the centre. The zero is important in order to ensure that fluorescence remains at the centre, but is depleted in the rest of the ring - this is the essence of the STED super-resolution process. Small phase aberrations can however cause the central intensity to be non-zero - hence phase aberrations can severely affect the performance of STED microscopes [8, 13]. It is also the case that polarization aberrations cause the central intensity to be non-zero.

Polarization aberration is also a concern for the structured illumination microscopy (SIM), which uses non-uniform illumination patterns projected onto the sample. By orienting the structured patterns at different positions, frequencies beyond the pass band of the microscope

can be retrieved [136]. SIM is again sensitive to small phase aberrations; they can influence the contrast and phase of the illumination grid pattern and cause very low image quality [12]. However, SIM is also sensitive to the polarization state of the light that creates the illumination grid pattern. Besides, since SIM illumination can be implemented with just three illuminated points instead of the whole pupil, polarization variations across the illuminated object field can be important.

However, the implementation of APC on STED or SIM might require some different configurations. The APC system requires a fixed polarization state in the PSG. If the beam is pre-aberrated, the PSG is not able to generate all the polarization states. Two SLMs or dual-pass is able to generate arbitrary polarization state only from a fixed state as in the APC. Hence, when designing the close-loop correction, we require a PSG that could change the polarization from any arbitrary state. If we want to change the polarization state from arbitrary state, another SLM is required. Another point to note when combining APC with microscopy is that, the birefringent disturbance brought by the sample would usually be based on reflection instead of transmission. Therefore, a different design is required using either sensor-less polarization control or considering the polarization difference between the reflection and transmission.

Combining phase and polarization correction:

The demonstrations here have concerned purely restoration of the polarization profile of the beam to its desired state. However, as discussed in the introduction, phase aberrations also play an important role in system performance. If phase and polarization aberrations are both pre-set to correct them simultaneously (or separately) would bring advantages to super resolution microscopes. The methods described in this thesis could be combined with conventional phase adaptive optics methods to provide further benefits in system correction.

7.2 Outlook

If the SLM is the only modulation device used in the system, it is possible to transfer the polarization to arbitrary state from an arbitrary state when using three SLMs (or three passes), and it can change both the phase and polarization from a fixed polarization state. However, three SLMs are not enough to realize full phase and polarization control with an arbitrary incoming polarization state. Therefore, another SLM is needed. Alternatively, one could also use a polarization-insensitive device to modulate the phase such as DM or mirror-based SLM.

The choice of the correction device is also an interesting topic to find the advantages and limitations of each device, and seek for a possibility to combine the DM and SLM together in the future to maximize their value and compensate their drawbacks.

Polarization reconstruction:

A further potential related area is to do the object reconstruction based on polarization like that based on phase reconstruction. As we know, the phase reconstruction is always studied by identifying the object after a scattering media, or restore the original 2D image or 3D object based on limited information. If the polarization reconstruction discussed here could be used as part of the effective evidence for identification, the 3D reconstruction might have an alternative method to realize. This needs investigation on how the polarization changes after the scattering media. The reconstruction therefore is not to restore the polarization state to the original state, but to link the changes of the polarization to its original phase, which contains the object information.

In conclusion, the work presented in this thesis explored a new direction in adaptive optics. It could form the basis of a polarization compensation system in optical systems that are affected by spatially variant polarization errors. Such an approach would have benefit in applications ranging from quantum optics, and microscopy imaging to clinical use.

Appendix: Conversion between Stokes parameters and Jones vectors

In the calculation of the Jones matrix of the birefringent disturbance, the Stokes parameters measured by PSA need to be converted to Jones vector for each measurement. To calculate the voltage sent to the SLM to generate the desired polarization state in PSG, the Jones vector needs to be converted to Stokes parameters. In this appendix, the conversion methods between these two vectors used in this work are listed [130].

Stokes parameters to Jones vectors:

According to Eq. (1.14), if we have the normalized Jones vector, $[|E_x|, |E_y|e^{i\delta}]^T$, where δ is the retardance between E_x and E_y. The Stokes parameters can be converted as:

$$S_0 = |E_x|^2 + |E_y|^2$$

$$S_1 = |E_x|^2 - |E_y|^2$$

$$S_2 = E_x * E_y^* + E_y * E_x^*$$

$$S_3 = i\left(E_x * E_y^* - E_y * E_x^*\right) \quad \text{(A1)}$$

Jones vector to Stokes parameters:

Given that the Stokes parameters measured by PSA are $[S_1, S_2, S_3]^T$, the Jones vector $[J_0, J_1]^T$ can be calculated as :

$$J_0 = \sqrt{\frac{1 + S_1/p}{2}}$$

$$J_1 = \frac{S_2 - iS_3}{p * 2J_0} \tag{A2}$$

where p is the degree of the polarization, $p = \sqrt{S_1^2 + S_2^2 + S_3^2}$. If $J_0 = 0$, J_1 will be automatically set to 1.

Publications during DPhil study

---

[1]. Dai, Yuanyuan, et al. "Active compensation of extrinsic polarization errors using adaptive optics." *Optics Express* 27.24 (2019): 35797-35810.

[2]. Dai, Yuanyuan, Jacopo Antonello, and Martin J. Booth. "Calibration of a phase-only spatial light modulator for both phase and retardance modulation." *Optics Express* 27.13 (2019): 17912-17926.

[3]. Dai, Yuanyuan, et al. "Adaptive measurement and correction of polarization aberrations." *Adaptive Optics and Wavefront Control for Biological Systems V*. Vol. 10886. International Society for Optics and Photonics, 2019.

[4]. Hu, Q., Dai, Y., He, C., & Booth, M. J. (2019). Arbitrary vectorial state conversion using liquid crystal spatial light modulators. *Optics Communications*.

[5]. Dai, Yuanyuan et al. "Polarization Adaptive Optics in Microscopy", XI Workshop on Adaptive Optics for Industry and Medicine, March. 5th, 2018

References

1. Ji, N., D.E. Milkie, and E. Betzig, *Adaptive optics via pupil segmentation for high-resolution imaging in biological tissues.* Nature methods, 2010. **7**(2): p. 141-147.
2. Azucena, O., et al., *Wavefront aberration measurements and corrections through thick tissue using fluorescent microsphere reference beacons.* Optics express, 2010. **18**(16): p. 17521-17532.
3. Burns, S.A., et al., *In vivo adaptive optics microvascular imaging in diabetic patients without clinically severe diabetic retinopathy.* Biomedical optics express, 2014. **5**(3): p. 961-974.
4. Burns, S.A., et al., *Introduction to special issue on adaptive optics for vision*. 2017, Elsevier.
5. Marcos, S., et al., *Vision science and adaptive optics, the state of the field.* Vision research, 2017. **132**: p. 3-33.
6. Li, M., W. Gao, and M. Cvijetic, *Slant-path coherent free space optical communications over the maritime and terrestrial atmospheres with the use of adaptive optics for beam wavefront correction.* Applied Optics, 2017. **56**(2): p. 284-297.
7. Tao, X., et al., *Adaptive optics confocal microscopy using direct wavefront sensing.* Optics letters, 2011. **36**(7): p. 1062-1064.
8. Gould, T.J., et al., *Adaptive optics enables 3D STED microscopy in aberrating specimens.* Optics express, 2012. **20**(19): p. 20998-21009.
9. Débarre, D., et al., *Image-based adaptive optics for two-photon microscopy.* Optics letters, 2009. **34**(16): p. 2495-2497.
10. Zheng, G., et al., *Characterization of spatially varying aberrations for wide field-of-view microscopy.* Optics express, 2013. **21**(13): p. 15131-15143.
11. Marsh, P., D. Burns, and J. Girkin, *Practical implementation of adaptive optics in multiphoton microscopy.* Optics Express, 2003. **11**(10): p. 1123-1130.
12. Débarre, D., et al., *Adaptive optics for structured illumination microscopy.* Optics express, 2008. **16**(13): p. 9290-9305.
13. Booth, M.J., *Adaptive optical microscopy: the ongoing quest for a perfect image.* Light: Science and Applications, 2014. **3**(4): p. e165.
14. Booth, M., et al., *Aberrations and adaptive optics in super-resolution microscopy.* Microscopy, 2015. **64**(4): p. 251-261.
15. Patton, B.R., et al., *Three-dimensional STED microscopy of aberrating tissue using dual adaptive optics.* Optics express, 2016. **24**(8): p. 8862-8876.
16. Zurauskas, M., et al., *IsoSense: frequency enhanced sensorless adaptive optics through structured illumination.* bioRxiv, 2018: p. 448613.
17. Ji, N., *Adaptive optical fluorescence microscopy.* Nature methods, 2017. **14**(4): p. 374.
18. Hecht, E., *Optics*. 2017: Pearson Education.
19. Gurevich, A.G. and G.A. Melkov, *Magnetization oscillations and waves*. 1996: CRC press.
20. Young, H.D., et al., *University physics*. Vol. 2. 1996: Addison-Wesley Reading, MA.
21. Bruning, J.H., et al., *Digital wavefront measuring interferometer for testing optical surfaces and lenses.* Applied optics, 1974. **13**(11): p. 2693-2703.
22. Kubby, J.A., *Adaptive Optics for Biological Imaging*. 2013: CRC press.

23. Roorda, A., et al., *Adaptive optics scanning laser ophthalmoscopy.* Optics express, 2002. **10**(9): p. 405-412.
24. Török, P., S. Hewlett, and P. Varga, *The role of specimen-induced spherical aberration in confocal microscopy.* Journal of microscopy, 1997. **188**(2): p. 158-172.
25. Booth, M.J. and B.R. Patton, *Adaptive optics for fluorescence microscopy.*
26. Schwertner, M., M.J. Booth, and T. Wilson, *Characterizing specimen induced aberrations for high NA adaptive optical microscopy.* Optics express, 2004. **12**(26): p. 6540-6552.
27. Zeng, J., et al., *3D resolved mapping of optical aberrations in thick tissues.* Biomedical optics express, 2012. **3**(8): p. 1898-1913.
28. Mahajan, V.N., *Zernike circle polynomials and optical aberrations of systems with circular pupils.* Applied optics, 1994. **33**(34): p. 8121-8124.
29. Booth, M.J., et al., *Adaptive aberration correction in a confocal microscope.* Proceedings of the National Academy of Sciences, 2002. **99**(9): p. 5788-5792.
30. Zhu, L., et al., *Wave-front generation of Zernike polynomial modes with a micromachined membrane deformable mirror.* Applied optics, 1999. **38**(28): p. 6019-6026.
31. Han, I.W., *New method for estimating wavefront from curvature signal by curve fitting.* Optical Engineering, 1995. **34**(4): p. 1232-1237.
32. Mahajan, V.N., *Zernike polynomial and wavefront fitting.* Optical Shop Testing, Third Edition, 2007: p. 498-546.
33. Zernike, F., *Phase contrast, a new method for the microscopic observation of transparent objects.* Physica, 1942. **9**(7): p. 686-698.
34. Love, G.D., *Wave-front correction and production of Zernike modes with a liquid-crystal spatial light modulator.* Applied optics, 1997. **36**(7): p. 1517-1524.
35. Noll, R.J., *Zernike polynomials and atmospheric turbulence.* JOsA, 1976. **66**(3): p. 207-211.
36. Chandrasekhar, S., *Radiative transfer*. 2013: Courier Corporation.
37. Goldstein, D.H., *Polarized light*. 2016: CRC press.
38. Notomi, á., *Theory of light propagation in strongly modulated photonic crystals: Refractionlike behavior in the vicinity of the photonic band gap.* Physical Review B, 2000. **62**(16): p. 10696.
39. Simon, M.C. and K.V. Gottschalk, *Waves and rays in uniaxial birefringent crystals.* Optik-International Journal for Light and Electron Optics, 2007. **118**(10): p. 457-470.
40. Lesso, J.P., et al., *Aberrations introduced by a lens made from a birefringent material.* Applied optics, 2000. **39**(4): p. 592-598.
41. Avendaño-Alejo, M. and M. Rosete-Aguilar, *Optical path difference in a plane-parallel uniaxial plate.* JOSA A, 2006. **23**(4): p. 926-932.
42. Gil, J.J., *Polarimetric characterization of light and media: physical quantities involved in polarimetric phenomena.* The European Physical Journal-Applied Physics, 2007. **40**(1): p. 1-47.
43. Azzam, R., *Arrangement of four photodetectors for measuring the state of polarization of light.* Optics letters, 1985. **10**(7): p. 309-311.
44. Girkin, J.M., S. Poland, and A.J. Wright, *Adaptive optics for deeper imaging of biological samples.* Current opinion in biotechnology, 2009. **20**(1): p. 106-110.
45. Stanton, S.T., *Illumination system and method employing a deformable mirror and diffractive optical elements*. 1997, Google Patents.
46. Fernández, E.J. and P. Artal, *Membrane deformable mirror for adaptive optics: performance limits in visual optics.* Optics express, 2003. **11**(9): p. 1056-1069.
47. Zhu, L., et al., *Adaptive control of a micromachined continuous-membrane deformable mirror for aberration compensation.* Applied Optics, 1999. **38**(1): p. 168-176.
48. Haber, A., et al., *Iterative learning control of a membrane deformable mirror for optimal wavefront correction.* Applied optics, 2013. **52**(11): p. 2363-2373.
49. Chen, J., et al., *High speed liquid crystal over silicon display based on the flexoelectro-optic effect.* Optics express, 2009. **17**(9): p. 7130-7137.
50. Vinas, M., et al., *Comparison of vision through surface modulated and spatial light modulated multifocal optics.* Biomedical Optics Express, 2017. **8**(4): p. 2055-2068.

51. Murali, S., K.P. Thompson, and J.P. Rolland, *Three-dimensional adaptive microscopy using embedded liquid lens.* Optics letters, 2009. **34**(2): p. 145-147.
52. Hecht, E., *Optik*. 1987: McGraw-Hill.
53. Collett, E., *Mathematical formulation of the interference laws of Fresnel and Arago.* American Journal of Physics, 1971. **39**(12): p. 1483-1495.
54. Mujat, M., A. Dogariu, and E. Wolf, *A law of interference of electromagnetic beams of any state of coherence and polarization and the Fresnel–Arago interference laws.* JOSA A, 2004. **21**(12): p. 2414-2417.
55. Chen, R. and H. Chen, *New method of interference fringes extraction and thining.* Journal of Laser, 2005. **26**(5): p. 40-41.
56. Takeda, M., H. Ina, and S. Kobayashi, *Fourier-transform method of fringe-pattern analysis for computer-based topography and interferometry.* JosA, 1982. **72**(1): p. 156-160.
57. Arines, J., *Least-squares modal estimation of wrapped phases: application to phase unwrapping.* Applied optics, 2003. **42**(17): p. 3373-3378.
58. Ghiglia, D.C. and M.D. Pritt, *Two-dimensional phase unwrapping: theory, algorithms, and software*. Vol. 4. 1998: Wiley New York.
59. Carmona, R.A., W.L. Hwang, and B. Torrésani, *Characterization of signals by the ridges of their wavelet transforms.* IEEE transactions on signal processing, 1997. **45**(10): p. 2586-2590.
60. Sciammarella, C.A. and T. Kim, *Determination of strains from fringe patterns using space-frequency representations.* Optical Engineering, 2003. **42**(11): p. 3182-3193.
61. Gdeisat, M.A., D.R. Burton, and M.J. Lalor, *Spatial carrier fringe pattern demodulation by use of a two-dimensional continuous wavelet transform.* Applied optics, 2006. **45**(34): p. 8722-8732.
62. Iris AO, I., *PTT111 Deformable Mirror System.* http://www.irisao.com/product.ptt111.html Feb 2016.
63. Jiang, M. and Y. Shang, *Adaptive performances of different membrane wave-front correctors in introducing Zernike aberrations.* Optik-International Journal for Light and Electron Optics, 2016. **127**(7): p. 3527-3530.
64. Peck, M., *Interferometry mathematics, algorithms, and data.* 2010.
65. Van Werkhoven, T., et al., *Snapshot coherence-gated direct wavefront sensing for multi-photon microscopy*. Optics express, 2014. **22**(8): p. 9715-9733.
66. Herráez, M.A., et al., *Fast two-dimensional phase-unwrapping algorithm based on sorting by reliability following a noncontinuous path.* Applied optics, 2002. **41**(35): p. 7437-7444.
67. Ndagano, B., et al., *Characterizing quantum channels with non-separable states of classical light.* Nature Physics, 2017. **13**(4): p. 397.
68. Sun, B., et al., *Four-dimensional light shaping: manipulating ultrafast spatiotemporal foci in space and time.* Light: Science & Applications, 2018. **7**(1): p. 17117.
69. Bruck, R., et al., *All-optical spatial light modulator for reconfigurable silicon photonic circuits.* Optica, 2016. **3**(4): p. 396-402.
70. Corbett, A.D., et al., *Microscope calibration using laser written fluorescence.* arXiv preprint arXiv:1806.05457, 2018.
71. Matsumoto, N., et al., *Aberration correction considering curved sample surface shape for non-contact two-photon excitation microscopy with spatial light modulator.* Scientific reports, 2018. **8**(1): p. 9252.
72. Maurer, C., et al., *What spatial light modulators can do for optical microscopy.* Laser & Photonics Reviews, 2011. **5**(1): p. 81-101.
73. Žurauskas, M., et al., *IsoSense: frequency enhanced sensorless adaptive optics through structured illumination.* Optica, 2019. **6**(3): p. 370-379.
74. Willig, K.I., et al., *Nanoscale resolution in GFP-based microscopy.* Nature methods, 2006. **3**(9): p. 721.
75. Carpenter, J., B.J. Eggleton, and J. Schröder, *Observation of Eisenbud–Wigner–Smith states as principal modes in multimode fibre.* Nature Photonics, 2015. **9**(11): p. 751.
76. Han, W., et al., *Vectorial optical field generator for the creation of arbitrarily complex fields.* Optics express, 2013. **21**(18): p. 20692-20706.

77. Lu, T., et al., *Generation of flower high-order Poincaré sphere laser beams from a spatial light modulator.* Scientific reports, 2016. **6**: p. 39657.
78. Naidoo, D., et al., *Controlled generation of higher-order Poincaré sphere beams from a laser.* Nature Photonics, 2016. **10**(5): p. 327-332.
79. Kenny, F., et al., *Complete polarization and phase control for focus-shaping in high-NA microscopy.* Optics express, 2012. **20**(13): p. 14015-14029.
80. Chen, J., L. Kong, and Q. Zhan, *Demonstration of a vectorial optical field generator with adaptive close loop control.* Review of Scientific Instruments, 2017. **88**(12): p. 125111.
81. Li, Y., et al., *Single-exposure fabrication of tunable Pancharatnam-Berry devices using a dye-doped liquid crystal.* Optics Express, 2019. **27**(6): p. 9054-9060.
82. Tsai, T.-H., X. Yuan, and D.J. Brady, *Spatial light modulator based color polarization imaging.* Optics express, 2015. **23**(9): p. 11912-11926.
83. Kagalwala, K.H., et al., *Single-photon three-qubit quantum logic using spatial light modulators.* Nature Communications, 2017. **8**(1): p. 739.
84. Haist, T., et al., *Parallelized genetic optimization of spatial light modulator addressing for diffractive applications.* Applied optics, 2014. **53**(7): p. 1413-1418.
85. Gupta, D.K., B. Tata, and T. Ravindran, *Optimization of a spatial light modulator driven by digital video interface graphics to generate holographic optical traps.* Applied optics, 2018. **57**(28): p. 8374-8384.
86. Yu, Z., et al., *Implementation of digital optical phase conjugation with embedded calibration and phase rectification.* Scientific reports, 2019. **9**(1): p. 1537.
87. Harriman, J.L., A. Linnenberger, and S.A. Serati. *Improving spatial light modulator performance through phase compensation*. in *Advanced Wavefront Control: Methods, Devices, and Applications II*. 2004. International Society for Optics and Photonics.
88. McDermott, S., et al., *Characterizing a spatial light modulator using ptychography.* Optics letters, 2017. **42**(3): p. 371-374.
89. Engström, D., et al., *Calibration of spatial light modulators suffering from spatially varying phase response.* Optics express, 2013. **21**(13): p. 16086-16103.
90. Fuentes, J.L.M., et al., *Interferometric method for phase calibration in liquid crystal spatial light modulators using a self-generated diffraction-grating.* Optics Express, 2016. **24**(13): p. 14159-14171.
91. Ferreira, F.P. and M.S. Belsley, *Direct calibration of a spatial light modulator by lateral shearing interferometry.* Optics express, 2010. **18**(8): p. 7899-7904.
92. Kelly, T.-L. and J. Munch, *Phase-aberration correction with dual liquid-crystal spatial light modulators.* Applied optics, 1998. **37**(22): p. 5184-5189.
93. Reichelt, S., *Spatially resolved phase-response calibration of liquid-crystal-based spatial light modulators.* Applied optics, 2013. **52**(12): p. 2610-2618.
94. Wang, H., et al., *Characterization of Spatial Light Modulator Based on the Phase in Fourier Domain of the Hologram and Its Applications in Coherent Imaging.* Applied Sciences, 2018. **8**(7): p. 1146.
95. Yamauchi, M., et al., *Interferometric phase measurements for polarization eigenvectors in twisted nematic liquid crystal spatial light modulators.* Optics communications, 2000. **181**(1-3): p. 1-6.
96. Xun, X. and R.W. Cohn, *Phase calibration of spatially nonuniform spatial light modulators.* Applied optics, 2004. **43**(35): p. 6400-6406.
97. Baker, K. and E. Stappaerts, *A single-shot pixellated phase-shifting interferometer utilizing a liquid-crystal spatial light modulator.* Optics letters, 2006. **31**(6): p. 733-735.
98. Mukhopadhyay, S., et al., *Polarization phase shifting interferometric technique for phase calibration of a reflective phase spatial light modulator.* Optical Engineering, 2013. **52**(3): p. 035602.
99. Calderon-Hermosillo, C., et al., *Inspection of complex amplitudes of spatial light modulators using moiré techniques.* Optics and Lasers in Engineering, 2013. **51**(5): p. 610-615.
100. Zhang, H., J. Zhang, and L. Wu, *Evaluation of phase-only liquid crystal spatial light modulator for phase modulation performance using a Twyman–Green interferometer.* Measurement Science and Technology, 2007. **18**(6): p. 1724.

101. Zhao, T., et al., *Multi-region phase calibration of liquid crystal SLM for holographic display.* Applied optics, 2017. **56**(22): p. 6168-6174.
102. Gupta, D.K., B. Tata, and T. Ravindran. *A technique to calibrate spatial light modulator for varying phase response over its spatial regions*. in *AIP Conference Proceedings*. 2018. AIP Publishing.
103. Hardy, J.W., *Adaptive optics for astronomical telescopes*. Vol. 16. 1998: Oxford University Press on Demand.
104. Abouraddy, A.F. and K.C. Toussaint Jr, *Three-dimensional polarization control in microscopy.* Physical review letters, 2006. **96**(15): p. 153901.
105. Zhan, Q., *Cylindrical vector beams: from mathematical concepts to applications.* Advances in Optics and Photonics, 2009. **1**(1): p. 1-57.
106. Naidoo, D., et al., *Controlled generation of higher-order Poincaré sphere beams from a laser.* Nature Photonics, 2016. **10**(5): p. 327.
107. Ruoff, J. and M. Totzeck, *Orientation Zernike polynomials: a useful way to describe the polarization effects of optical imaging systems.* Journal of Micro/Nanolithography, MEMS, and MOEMS, 2009. **8**(3): p. 031404.
108. Smith, B.W. and J.S. Cashmore. *Challenges in high NA, polarization, and photoresists*. in *Optical Microlithography XV*. 2002. International Society for Optics and Photonics.
109. Enderlein, J., E. Toprak, and P.R. Selvin, *Polarization effect on position accuracy of fluorophore localization.* Optics express, 2006. **14**(18): p. 8111-8120.
110. Spring, K. and S. Inoué, *Video microscopy: the fundamentals*. 1997, New York: Plenum Press.
111. Inoué, S. and R. Oldenbourg, *Microscopes.* Handbook of Optics, 1995. **2**: p. 17.1-17.52.
112. Knell, H. and H.-M. Heuck. *Birefringence measurement in complex optical systems.* in *Optical Measurement Systems for Industrial Inspection X*. 2017. International Society for Optics and Photonics.
113. Willig, K.I., et al., *STED microscopy reveals that synaptotagmin remains clustered after synaptic vesicle exocytosis.* Nature, 2006. **440**(7086): p. 935.
114. Wicker, K. and R. Heintzmann, *Single-shot optical sectioning using polarization-coded structured illumination.* Journal of Optics, 2010. **12**(8): p. 084010.
115. Perreault, J.D., *Triple Wollaston-prism complete-Stokes imaging polarimeter.* Optics letters, 2013. **38**(19): p. 3874-3877.
116. Oka, K. and T. Kaneko, *Compact complete imaging polarimeter using birefringent wedge prisms.* Optics express, 2003. **11**(13): p. 1510-1519.
117. Bueno, J.M. and P. Artal, *Double-pass imaging polarimetry in the human eye.* Optics letters, 1999. **24**(1): p. 64-66.
118. Kudenov, M.W., et al., *White-light channeled imaging polarimeter using broadband polarization gratings.* Applied optics, 2011. **50**(15): p. 2283-2293.
119. Li, J., et al., *Broadband snapshot complete imaging polarimeter based on dual Sagnac-grating interferometers.* Optics express, 2018. **26**(20): p. 25858-25868.
120. Mu, T., et al., *Static hyperspectral imaging polarimeter for full linear Stokes parameters.* Optics express, 2012. **20**(16): p. 18194-18201.
121. Mitchell, K.J., et al., *Polarisation structuring of broadband light.* Optics express, 2017. **25**(21): p. 25079-25089.
122. Eriksen, R.L., P.C. Mogensen, and J. Glückstad, *Elliptical polarisation encoding in two dimensions using phase-only spatial light modulators.* Optics communications, 2001. **187**(4-6): p. 325-336.
123. Rong, Z.-Y., et al., *Generation of arbitrary vector beams with cascaded liquid crystal spatial light modulators.* Optics Express, 2014. **22**(2): p. 1636-1644.
124. Zhu, L. and J. Wang, *Arbitrary manipulation of spatial amplitude and phase using phase-only spatial light modulators.* Scientific reports, 2014. **4**: p. 7441.
125. Zhu, L. and J. Wang, *Arbitrary manipulation of spatial amplitude and phase using phase-only spatial light modulators.* Scientific reports, 2014. **4**.
126. Mujat, M., E. Baleine, and A. Dogariu, *Interferometric imaging polarimeter.* JOSA A, 2004. **21**(11): p. 2244-2249.

127. Woźniak, W.A. and P. Kurzynowski, *Compact spatial polariscope for light polarization state analysis*. Optics Express, 2008. **16**(14): p. 10471-10479.
128. Sabatke, D., et al., *Optimization of retardance for a complete Stokes polarimeter*. Optics Letters, 2000. **25**(11): p. 802-804.
129. LIEN, b.A., *A detailed derivation of extended Jones matrix representation for twisted nematic liquid crystal displays.* Liquid Crystals, 1997. **22**(2): p. 171-175.
130. Hauge, P., R.H. Muller, and C. Smith, *Conventions and formulas for using the Mueller-Stokes calculus in ellipsometry*. Surface science, 1980. **96**(1-3): p. 81-107.
131. Inc, T., *https://www.thorlabs.com/newgrouppage9.cfm?objectgroup_id=9098*.
132. Bernacki, B.E. and M. Mansuripur, *Investigation of substrate birefringence effects on optical-disk performance.* Applied optics, 1993. **32**(32): p. 6547-6555.
133. Takahashi, A., et al., *Influence of birefringence on the signal quality of magnetooptic disks using polycarbonate substrates.* Applied optics, 1988. **27**(14): p. 2863-2866.
134. Menzel, M., et al., *A Jones matrix formalism for simulating three-dimensional polarized light imaging of brain tissue.* Journal of the Royal Society Interface, 2015. **12**(111): p. 20150734.
135. Axer, M., et al., *High-resolution fiber tract reconstruction in the human brain by means of three-dimensional polarized light imaging.* Frontiers in neuroinformatics, 2011. **5**: p. 34.
136. Schermelleh, L., R. Heintzmann, and H. Leonhardt, *A guide to super-resolution fluorescence microscopy*. The Journal of cell biology, 2010. **190**(2): p. 165-175.